

Fall 2014

Applications of halloysite nanocontainers for functional protective coating

Anupam Ramesh Joshi

Follow this and additional works at: <https://digitalcommons.latech.edu/dissertations>

 Part of the [Nanoscience and Nanotechnology Commons](#)

**APPLICATIONS OF HALLOYSITE NANOCONTAINERS
FOR FUNCTIONAL PROTECTIVE COATING**

by,

Anupam Ramesh Joshi, B.Sc., M.Sc., M.S.

A Dissertation Presented in Partial Fulfillment
of the Requirements for the Degree of
Doctor of Philosophy

COLLEGE OF ENGINEERING AND SCIENCE
LOUISIANA TECH UNIVERSITY

November 2014

UMI Number: 3662476

All rights reserved

INFORMATION TO ALL USERS

The quality of this reproduction is dependent upon the quality of the copy submitted.

In the unlikely event that the author did not send a complete manuscript and there are missing pages, these will be noted. Also, if material had to be removed, a note will indicate the deletion.



UMI 3662476

Published by ProQuest LLC 2015. Copyright in the Dissertation held by the Author.

Microform Edition © ProQuest LLC.

All rights reserved. This work is protected against unauthorized copying under Title 17, United States Code.



ProQuest LLC
789 East Eisenhower Parkway
P.O. Box 1346
Ann Arbor, MI 48106-1346

LOUISIANA TECH UNIVERSITY

THE GRADUATE SCHOOL

NOVEMBER 15, 2014

Date

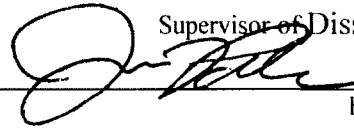
We hereby recommend that the dissertation prepared under our supervision by
ANUPAM RAMESH JOSHI, B.Sc., M.Sc., M.S.

entitled APPLICATIONS OF HALLOYSITE NANOCONTAINERS
FOR FUNCTIONAL PROTECTIVE COATING

be accepted in partial fulfillment of the requirements for the Degree of
DOCTOR OF PHILOSOPHY IN ENGINEERING

Yuri Lvov

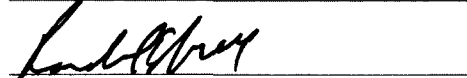
Supervisor of Dissertation Research



Head of Department
ENGINEERING

Department

Recommendation concurred in:



ERAZA Alouchani




Advisory Committee

Approved:



Director of Graduate Studies



Dean of the College

Approved:



Dean of the Graduate School

ABSTRACT

In this study we have explored the applications of halloysite clay nanotubes as a nanocontainer. Halloysite nanotubes are used as a storage unit for anticorrosion agents, flame retardants, and a dopant to extend the curing time for geopolymer composites. Halloysite is a naturally occurring clay mineral with a chemical formula of $\text{Al}_2\text{Si}_2\text{O}_5(\text{OH})_4 \cdot 2 \text{H}_2\text{O}$ and is identical to kaolinite with the exception that it holds an additional water monolayer in its interlayered spaces. Upon heating at higher temperatures, halloysite loses the additional water monolayer, and this variant known colloquially as “meta-halloysite” has a chemical formula of $\text{Al}_2\text{Si}_2\text{O}_5(\text{OH})_4$ [1][3].

This study has been divided into five sections. The first section explores the implementation of acid etching for interlayered alumina to increase the loading efficiency of the halloysite. Halloysite is mixed with the sulfuric acid at 0.5 M, 1 M and 2 M concentrations at varying temperature. It is observed that the alumina that composes the halloysite is degraded faster at temperatures above room temperature and at higher concentrations of sulfuric acid.

The second section addresses the application of halloysite as a nanocontainer for the anticorrosion agents for the protection of ASTM A366 steel plates. Halloysite nanotubes are loaded with different types of anticorrosion agents, and are then admixed with an acrylic paint. Samples are exposed to a saline environment for one month. Compared to the controlled samples, halloysite loaded with corrosion inhibitors are found

to enhance self-healing. This makes halloysite nanotubes a strong candidate for self-healing composites.

In the third section, controlled release of dodecylamine from halloysite nanotubes is used in the implementation of metal-organic and polymeric stoppers. Different types of metal stoppers and polymeric stoppers are analyzed and release studies for dodecylamine are performed in water and paint thinner.

In the fourth section, halloysite is explored as a flame retardant. Halloysite nanotubes are mixed with latex paint in concentrations of 5 wt% and 7 wt%, and the samples are tested for flame retardancy by exposing them to a flame torch following the ASTM E84 standard. Simultaneously, paint is mixed with a commercial flame retardant additive and the results are compared pre and post-flame exposure for both samples, with and without halloysite mixed paint.

In the final section, halloysite nanotubes used to extend the curing time of geopolymer samples can be achieved for the fly ash samples with a higher calcium content. High calcium content fly ash samples set faster than normal fly ashes. Halloysite coating increases the curing time, therefore giving ample time for the cement sample to flow and set in any desired shape. Utilizing the Layer-by-Layer (LbL) technique, fly ash particles are coated with halloysite, and the curing time is analyzed using rheological testing at room temperature and at 100° C. The coating of halloysite on the fly ash particles is characterized with SEM and Zeta-potential resulting in an optimized shell coating on the fly ash. An extension of curing time from 2 to 8 hrs is reached which is patented (pending) as an important technological development in this new constructional material.

DEDICATION

To my dear parents, Dr. Ramesh G. Joshi, and Mrs. Pratima R. Joshi, my brothers, Abhishek, Amit and my beloved wife Anisha.

TABLE OF CONTENTS

| | |
|--|------|
| ABSTRACT..... | iii |
| DEDICATION..... | vi |
| LIST OF TABLES..... | xii |
| LIST OF FIGURES | xiii |
| ACKNOWLEDGMENTS | xx |
| CHAPTER 1 INTRODUCTION | 1 |
| 1.1 Nanocontainers for Active Agent Storage..... | 2 |
| 1.2 Research Goals | 4 |
| 1.3 Dissertation Overview | 5 |
| CHAPTER 2 BACKGROUND AND THEORY | 8 |
| 2.1 Chemistry and Structural Characterization of Halloysite | 8 |
| 2.2 Biocompatibility of Halloysite nanotubes | 13 |
| 2.3 Implementation of Halloysite Nanotubes as a Nanocontainer for active agents..... | 15 |
| 2.4 Halloysite as an Nanocontainer for Drugs..... | 17 |
| 2.5 Halloysite Nanotubes for the Encapsulation of Anticorrosive Agents | 20 |
| 2.6 Application of Halloysite Nanotubes for Flame Retardant Coatings | 22 |
| 2.7 Halloysite Nanotubes for Encapsulation of Metal/Inorganic Substances..... | 23 |
| 2.8 Applications of Halloysite Nanotubes | 25 |
| 2.8.1 Halloysite-polymer nanocomposites..... | 25 |
| 2.8.2 Halloysite as a hydrocarbon conversion catalyst..... | 26 |

| | | |
|--|---|----|
| 2.9 | Conclusion | 27 |
| CHAPTER 3 ENLARGEMENT OF HALLOYSITE CLAY NANOTUBE LUMEN BY SELECTIVE ETCHING OF ALUMINUM OXIDE..... | | |
| 3.1 | Introduction..... | 29 |
| 3.2 | Materials and Methods..... | 31 |
| 3.2.1 | Materials | 31 |
| 3.2.2 | Characterization | 31 |
| 3.2.3 | Halloysite etching by sulfuric acid | 32 |
| 3.2.4 | Determination of aluminum concentration | 32 |
| 3.2.5 | Halloysite loading with benzotriazole | 33 |
| 3.2.6 | Halloysite loading with silver | 33 |
| 3.3 | Results and Discussion | 33 |
| 3.3.1 | The tube lumen etching..... | 34 |
| 3.3.2 | Particle size distribution..... | 38 |
| 3.3.3 | FT-IR, ²⁹ Si MAS-NMR and XRD spectral characterization | 39 |
| 3.3.4 | Kinetics of alumina etching | 44 |
| 3.3.5 | Enhanced encapsulation of chemicals within halloysite tubes | 48 |
| 3.4 | Conclusion | 50 |
| CHAPTER 4 INTERFACIAL MODIFICATION OF CLAY NANOTUBE FOR SUSTAINED RELEASE OF CORROSION INHIBITORS | | |
| 4.1 | Introduction..... | 52 |
| 4.2 | Materials and Methods..... | 54 |
| 4.2.1 | Materials | 54 |
| 4.2.2 | Instrumentation | 54 |
| 4.2.3 | Tube loading procedure | 55 |
| 4.2.4 | Kinetics of corrosion inhibitors release | 55 |

| | | |
|---|--|-----------|
| 4.2.5 | Tube encapsulation with urea-formaldehyde..... | 56 |
| 4.2.6 | Tube end stopper formation copper ions treatment | 56 |
| 4.2.7 | Corrosion resistance testing | 56 |
| 4.2.8 | Monitoring corrosion current..... | 57 |
| 4.3 | Results and Discussion | 57 |
| 4.3.1 | Clay nanotube characterization..... | 57 |
| 4.3.2 | Inhibitors for corrosion protection | 58 |
| 4.3.3 | Loading halloysite with corrosion inhibitors | 60 |
| 4.3.4 | Release of corrosion inhibitors | 61 |
| 4.3.5 | Formation of tube end stoppers..... | 63 |
| 4.3.6 | Evaluation of the encapsulation | 64 |
| 4.3.7 | Controlled release profiles | 66 |
| 4.3.8 | Paint anticorrosion performance | 67 |
| 4.3.9 | Analysis of the undercoat corrosion | 68 |
| 4.3.10 | Enhanced paint adhesion..... | 69 |
| 4.3.11 | Corrosion current density mapping..... | 71 |
| 4.4 | Conclusions..... | 73 |
| CHAPTER 5 USE OF INORGANIC AND POLYMERIC STOPPERS FOR THE CONTROLLED RELEASE OF DODECYLAMINE | | 74 |
| 5.1 | Introduction..... | 74 |
| 5.2 | Materials & Methods | 74 |
| 5.2.1 | Materials | 74 |
| 5.2.2 | Instrumentation | 75 |
| 5.2.3 | Halloysite loading with Dodecylamine..... | 75 |
| 5.2.4 | Acid and Base treatment..... | 76 |
| 5.3 | Results and Discussion | 76 |

| | | |
|--|--|-----------|
| 5.3.1 | Halloysite characterization using SEM..... | 76 |
| 5.3.2 | Determination of the amine concentration in water..... | 77 |
| 5.3.3 | Comparison of acid and base treated halloysite samples..... | 78 |
| 5.3.4 | Formation of stoppers at tube endings..... | 80 |
| 5.3.5 | Determination of amine in xylol..... | 83 |
| 5.3.6 | Observation of dodecylamine leakage in xylol..... | 85 |
| 5.4 | Conclusion..... | 86 |
| CHAPTER 6 FLAME RETARDANT COATING DOPED WITH HALLOYSITE CLAY NANOTUBES FOR FLAKE BOARD PROTECTION | | 88 |
| 6.1 | Introduction..... | 88 |
| 6.2 | Materials and Methods..... | 90 |
| 6.2.1 | Materials..... | 90 |
| 6.2.2 | Instrumentation..... | 91 |
| 6.2.3 | Loading of Triphenyl phosphate (TPP) and FR-1 flame additive into halloysite..... | 91 |
| 6.2.4 | Preparation of samples for flame retardant testing on wooden board | 92 |
| 6.2.5 | Preparation of samples for flame retardant testing on metal | 92 |
| 6.3 | Results & Discussion..... | 93 |
| 6.3.1 | Halloysite characterization using SEM..... | 93 |
| 6.3.2 | Analysis of Triphenyl phosphate loading efficiency into halloysite | 93 |
| 6.3.3 | Halloysite admixed latex paint samples before flame test..... | 95 |
| 6.3.4 | Halloysite admixed latex paint samples after flame test on wooden board.. | 96 |
| 6.3.5 | Halloysite admixed latex paint samples after flame test on metal..... | 99 |
| 6.3.6 | Possible mechanism of halloysite flame retardancy | 101 |
| 6.4 | Conclusion..... | 103 |

| | |
|--|------------|
| CHAPTER 7 GEOPOLYMERS PROPERTIES OPTIMIZATION WITH FLY-ASH MICROPARTICLE COATING WITH NANOCCLAYS..... | 105 |
| 7.1 Introduction..... | 105 |
| 7.2 Materials and Methods..... | 107 |
| 7.2.1 Materials | 107 |
| 7.2.2 Instrumentation | 107 |
| 7.2.3 Mixing of halloysite nanotubes with fly ash..... | 107 |
| 7.2.4 Layer-by-Layer (LbL) coating of fly ash with polyelectrolytes | 108 |
| 7.2.5 Flow test and viscosity measurements..... | 110 |
| 7.3 Results and Discussion | 110 |
| 7.3.1 Halloysite and fly ash characterization by SEM..... | 110 |
| 7.3.2 Halloysite interaction with activating solution in fly ash mixture | 111 |
| 7.3.3 Layer-by-Layer assembly for fly ash coating with halloysite | 113 |
| 7.3.4 Flow test and Rheology tests results..... | 117 |
| 7.4 Conclusion | 122 |
| CHAPTER 8 CONCLUSION AND FUTURE WORK | 124 |
| 8.1 Conclusion | 124 |
| 8.2 Future Work..... | 126 |
| APPENDIX A KINETICS OF SELECTIVE ALUMINA ETCHING AND CHARACTERIZATION OF DEALUMINATION | 128 |
| APPENDIX B ANALYSIS OF ANTICORROSIVE AGENTS LOADING BASED ON THERMOGRAVIMETRIC ANALYSIS | 133 |
| REFERENCES | 138 |

LIST OF TABLES

| | |
|---|-----|
| Table 4-1: Parameters of the Weibull's kinetic equation for the inhibitors' release from halloysite. | 63 |
| Table 4-2: Paint adhesive forces on metal strips of ASTM A366 mild steel, after one month of exposure to the 3% NaCl solution..... | 71 |
| Table 7-1: Change in surface charge with deposition of polyelectrolytes for Dollet Hill fly ash..... | 114 |
| Table 7-2: Change in surface charge with deposition of polyelectrolytes for Dollet Hill fly ash..... | 116 |
| Table 7-3: Setting times for geopolymer + halloysite pastes prepared out of Monticello fly ash. | 120 |

LIST OF FIGURES

| | |
|---|----|
| Figure 2-1: Halloysite mineral in rock form (a), and processed form (b). | 9 |
| Figure 2-2: Representation of halloysite structure: side view and top view of the halloysite layer [22]. | 10 |
| Figure 2-3: X-ray powder diffraction pattern for halloysite sample. | 11 |
| Figure 2-4: SEM and TEM images of halloysite nanotubes. a) TEM clearly shows the layered morphology of halloysite nanotubes, b) SEM of halloysite samples from Xinjiang province, China, and c) inner lumen is clearly visible with a TEM of nanotubes. | 12 |
| Figure 2-5: Comparison of halloysite nanotubes surface charge with silicon dioxide (blue) and aluminum oxide (red) from ζ -potential analysis [23]. | 13 |
| Figure 2-6: Halloysite cytotoxicity testing on A) MCF cells, and B) HeLA cells at different concentrations and exposure times [23]. | 14 |
| Figure 2-7: Scheme of halloysite loading using vacuum suction [46]. | 17 |
| Figure 2-8: Release profile for gentamicin loaded into halloysite (left) and chemical formula for gentamicin (right) [54]. | 18 |
| Figure 2-9: Comparison of Release profiles for pure drugs Dexamethasone, Furosemide and Nifedipine crystals and drugs loaded into halloysite [55]. | 19 |
| Figure 2-10: Release profiles for Benzotriazole loaded halloysite nanotubes with and without stoppers (a), and change in controlled release with increasing Cu^{2+} ions concentration [21]. | 21 |
| Figure 2-11: Comparison of stress-strain relation for acrylic paint with and without doping with halloysite [21]. | 21 |
| Figure 2-12: Inorganic substances loaded into halloysite lumen; silver (a,b), sodium tetrachloropelladate (c), and potassium permanganate (d) [54]. | 24 |
| Figure 2-13: Carbonate deposited into halloysite lumen indicated by TEM image (a), and on the tube end by SEM (b). | 24 |

| | |
|---|----|
| Figure 3-1: Halloysite mineral obtained from Dragon Mine Utah, Applied Mineral, Inc., USA (a); SEM of raw powder sample (b); TEM image of tubes with the cross section (inset) and HR-TEM of halloysite multilayer wall (c-d)..... | 34 |
| Figure 3-2: The acid etching of alumina inner layers from halloysite lumen..... | 35 |
| Figure 3-3: SEM images of halloysite tubes after removal of 20% (a), 40% (b), 50% (c), 75% (d), 88% (e) and 100% (f) of aluminum..... | 36 |
| Figure 3-4: TEM images of pristine halloysite before acid treatment (a, b), after the removal of 20 % (c, d), 65 % (e, f) and 100 % (g, h) of alumina by treatment with H ₂ SO ₄ at 50°C. External diameters of the tubes are ca. 70 nm. Lumen diameters are 9.7 nm, 21.5 nm and 36.3 ± 2 nm for original, 20 % and 65 % alumina etched halloysites. Histogram of lumen diameters (i) and external diameters (j) for original and 20 % alumina etched halloysite is also shown (based on 200 tubes' measurements). | 38 |
| Figure 3-5: Halloysite particle size distribution at different levels of alumina etched measured by dynamic light scattering..... | 39 |
| Figure 3-6: FT-IR spectra of halloysite at different levels of Al ₂ O ₃ conversion..... | 41 |
| Figure 3-7 XRD spectra of halloysite at different conversion levels; * aluminum from substrate, * quartz..... | 42 |
| Figure 3-8: ²⁹ Si MAS-NMR spectra of halloysite at different levels of alumina dissolution. | 43 |
| Figure 3-9: Schematic of the partially etched halloysite layer with assignments of the silicon nuclei. | 44 |
| Figure 3-10: (a) Increase of Al ³⁺ concentration in reaction mixture of halloysites and sulfuric acid vs temperature (aluminum concentration was normalized to maximum). (b) Variation of the logarithm of the linear reaction rate on reciprocal of the temperature. | 46 |
| Figure 3-11: TEM images of the halloysite tubes with 20% alumina removal in two regimes: at 80° C (a) and 50° C (b)..... | 47 |
| Figure 3-12: TEM images of silver nanorods within halloysite tubular templates (a) and the magnified image showing silver crystalline planes (b). | 49 |
| Figure 3-13: Benzotriazole (BTA) loading efficiency of halloysites treated with sulfuric acid..... | 50 |
| Figure 4-1: SEM (a) and TEM (b) images of halloysite. | 57 |

| | |
|--|----|
| Figure 4-2: Schematic demonstration of the self-healing effect. | 58 |
| Figure 4-3: Chemical structures of benzotriazole (BTA) - a, 2-mercaptobenzimidazole (MBI) – b, and 2-mercaptobenzothiazole (MBT) – c. | 59 |
| Figure 4-4: Comparison of inhibition efficiencies (%) of different corrosion inhibitors tested on ASTM A366 steel (BTA-benzotriazole, MBT—mercaptobenzothiazole, and MBI- mercaptobenzimidazole). | 60 |
| Figure 4-5: Halloysite release profiles of inhibitors: BTA-benzotriazole, MBT—mercaptobenzothiazole, and MBI- mercaptobenzimidazole (solid lines). Dissolution profiles of powder inhibitors (dashed lines) are also shown. | 62 |
| Figure 4-6: Formation of UF polymer network and stoppers formation (a-b). Copper-benzotriazole thin film coating formation (c). | 64 |
| Figure 4-7: SEM image (a) and EDX spectrum (b) of UF polymer coated halloysite nanotubes. TEM visualization with elemental mapping of the shells formed on halloysite external surface with interaction of mercaptobenzothiazole-MBI with Cu (II) ions (c, d and e). | 65 |
| Figure 4-8: Release time reduction for benzotriazole, BTA (a), mercaptobenzothiazole, MBT (b), and mercaptobenzimidazole, MBI (c) by the additional encapsulation with urea-formaldehyde, UF and copper ions treatments. | 66 |
| Figure 4-9: Corrosion development images of artificially scratched acrylic painted iron alloy with (a) untreated original paint, and coatings with halloysite containing (b) BTA, (c) MBT, and (d) MBI, (e) halloysite containing BTA with Cu-stoppers and (f) halloysite containing BTA with UF-stoppers. | 68 |
| Figure 4-10: Optical microscope (50 x magnification) images of metal surface underneath the coating after one month corrosion test. (a)-control sample, paint with halloysite loaded with BTA-benzotriazole (b), MBT—mercaptobenzothiazole (c), and MBI- mercaptobenzimidazole (d); BTA loaded halloysite with Cu-stoppers (e) and BTA loaded halloysite with UF-stoppers. | 69 |
| Figure 4-11: Setup for testing paint adhesive force on metal. | 70 |
| Figure 4-12: Corrosion current density maps using scanning vibrating electrode technique (SVET) of pure paint sample (a), paint with MBI loaded halloysite (b) and paint with BTA loaded halloysite encapsulated with UF stoppers. Artificially scratched and kept in highly corrosive solution of 0.5 M NaCl. | 72 |
| Figure 5-1: General Schematic for the halloysite loading procedure [21]. | 75 |

| | |
|--|----|
| Figure 5-2: SEM and TEM images of Sodium hydroxide (a) and (b), and with sulfuric acid (c) and (d), respectively. | 77 |
| Figure 5-3: Standard curve for determination of dodecylamine concentration in water..... | 78 |
| Figure 5-4: Dodecylamine release profiles from pure and modified halloysite samples..... | 79 |
| Figure 5-5: Illustration of stopper formation at halloysite tube endings by interaction of leaking dodecylamine [21], [22], [46], [54]. | 80 |
| Figure 5-6: General Scheme for encapsulation of dodecylamine..... | 81 |
| Figure 5-7: Dodecylamine (DA) release profiles from Acid treated and bare halloysite samples with Copper and Iron based stoppers. | 82 |
| Figure 5-8: Dodecylamine (DA) release profiles from Acid treated halloysite samples with Cu(I), Fe(II), glutaraldehyde and sodiumtripolyphosphate based stoppers..... | 83 |
| Figure 5-9: Reaction of primary amine with aldehyde to determine the concentration of Schiff's base [110]..... | 84 |
| Figure 5-10: Standard curve for determination of dodecylamine concentration in xylol. | 85 |
| Figure 5-11: UV spectrum of the samples collected from xylol suspension of the halloysite. (Big noise below 380 nm is due to the signals from salicylaldehyde and xylol. Salicylaldehyde was added to solutions before analyzing samples with UV). | 86 |
| Figure 6-1: TGA curve for pure triphenyl phosphate (TPP)..... | 94 |
| Figure 6-2: TGA curve for TPP loaded into halloysite nanotubes. | 94 |
| Figure 6-3: Wooden flake board samples applied with a) pure paint, b) paint + 5 wt% halloysite, c) paint + 7 wt% halloysite, d) paint + 5 wt% halloysite with FR-1, e) paint + pure FR-1..... | 95 |
| Figure 6-4: ASTM A366 steel metal surface coated with 1) pure paint, 2) paint + 5 wt% halloysite, 3) paint + 7 wt% halloysite, 4) paint + 5 wt% halloysite with FR-1, 5) paint + pure FR-1..... | 96 |
| Figure 6-5: a)Pure paint sample after flame test, b) Paint +5 wt% halloysite sample after flame test..... | 97 |

| | |
|---|-----|
| Figure 6-6: c) Paint +7 wt% halloysite sample after flame test, d) Paint with 5 wt% FR-1 flame retardant admixed with halloysite..... | 98 |
| Figure 6-7: e) Paint with 5 wt% Halloysite loaded with TPP, f) Paint + 5 wt% FR-1 flame retardant. | 99 |
| Figure 6-8: Paint samples after burn test on metals, a) Pure latex paint, b) Paint + 5 wt% halloysite, c) Paint + 7 wt% halloysite, d) Paint + 5 wt% FR-1 loaded halloysite, e) Paint + 5 wt% FR-1 additive, f) Paint + 7 wt% FR-1 additive..... | 101 |
| Figure 6-9: Optical microscopic images of a) Paint + 5 wt% halloysite before flame test, b) Paint + 5 wt% halloysite after flame test, c) Paint + 7 wt% halloysite before flame test, d) Paint + 7 wt% halloysite after flame test. | 103 |
| Figure 7-1: a) Chemical structure for PAA, b) PEI. | 109 |
| Figure 7-2: SEM images of a) halloysite nanotubes, b) dry fly ash [119]..... | 110 |
| Figure 7-3: a) 3% halloysite pre-mixed with fly ash particles in 10 M NaOH, b) 3% halloysite pre-mixed with fly ash particles in 12 M NaOH, c) 6% halloysite pre-mixed with fly ash particles in 10 M NaOH, d) 6% halloysite pre-mixed with fly ash particles in 12 M NaOH..... | 112 |
| Figure 7-4: a) 3% halloysite mixed with the geopolymer paste in 10 M NaOH, b) 3% halloysite pre-mixed with the geopolymer paste in 12 M NaOH, c) 6% halloysite mixed with the geopolymer paste in 10 M NaOH, d) 6% halloysite mixed with the geopolymer paste in 12 M NaOH. | 113 |
| Figure 7-5: Schematic representation of LbL assembly on MO fly ash surface. | 114 |
| Figure 7-6: a), and b) Dry DH fly ash mixed with 6% halloysite before LbL coating, c), and d) DH fly ash mixed with 6% halloysite after LbL coating..... | 115 |
| Figure 7-7: a) and b) Dry DH fly ash mixed with 6% halloysite before LbL coating, c and d) DH fly ash mixed with 6% halloysite after LbL coating. | 117 |
| Figure 7-8: Flow test for the DH fly ash pre-mixed halloysite sample (dry process). .. | 118 |
| Figure 7-9: Flow test for the halloysite mixed with the DH fly ash geopolymer paste sample (wet process)..... | 118 |
| Figure 7-10: Dynamic viscosity values for geopolymer paste prepared with a sodium hydroxide solution of 10 M (a), 12 M (b) for different halloysite loadings and mixing procedures [Blue -wet process, Red -Dry process]..... | 119 |

- Figure 7-11:** Viscosity at room temperature for controlled MO fly ash, fly ash with controlled 6% halloysite, and fly ash with 6% treated halloysite. 121
- Figure 7-12:** Viscosity at 50° C. for control DH fly ash, fly ash with control 6% halloysite, and fly ash with 6% treated halloysite. 122
- Figure A-1:** FT-IR Peak ratios of halloysites at different levels of dealumination. 129
- Figure A-2:** Solid State ²⁷Al NMR Spectra of halloysite samples at various levels of dealumination by sulfuric acid. 129
- Figure A-3:** Kinetic curves of the halloysite dealumination at 80° C fit to the kinetic models of zeroth (A), 2/3rd (B) and first (C) order reaction kinetics. Correlation coefficients of the halloysite dealumination curves at 80°C fit to the kinetic equations of various orders in aluminum (D). Kinetic profiles were fit to the equation $Kt = 1 - (1-X)^{1-n}$, where K is the reaction rate constant, X is the halloysite dealumination level at time t and n is the reaction order in aluminum. Maximum correlation is observed at value of $n = 2/3$ 130
- Figure A-4:** (a) Alumina etching curves of halloysites at 50° C with sulfuric acid of three different concentrations 0.5 M (diamonds), 1.0 M (squares) and 2.0 M (triangles). (b) $\ln(v)$ vs $\ln(c)$ curves of the alumina etching profiles, v -reaction rate, c -sulfuric acid concentration. As one can see, $\ln(v) = \ln(c) + C$, i.e. $v = k \cdot c$ 131
- Figure A-5:** (a) Alumina etching curves of halloysites at 80° C with sulfuric acid of three different concentrations 0.5 M (diamonds), 1.0 M (squares) and 2.0 M (triangles). (b) $\ln(v)$ vs $\ln(c)$ curves of the alumina etching profiles, v -reaction rate, c -sulfuric acid concentration. As one can see, $\ln(v) = 0.2\ln(c) + C$, i.e. $v = k \cdot c^{0.2}$ 131
- Figure A-6:** Relative values of halloysite bending stiffness and tensile strength (normalized to 100) at various lumen diameters. 132
- Figure A-7:** Relative values of halloysite bending stiffness and tensile strength per unit weight (normalized to 100) at various lumen diameters. 132
- Figure B-8:** TGA curve for BTA loaded halloysite nanotubes. 135
- Figure B-9:** TGA curve for 2-MBT loaded halloysite nanotubes. 135
- Figure B-10:** TGA curve for 2-MBI loaded halloysite nanotubes. 136
- Figure B-11:** X-ray powder diffraction patterns (Cu-K α) of the halloysite loaded with BTA (a), MBT (b), and MBI (c) and empty pristine halloysite (d). 136

Figure B-12: Optical microscope images from the back sides of the coatings removed from corroded steel strips, (a)-original paint and paint admixed with (b)-BTA, (c)-MBT, (d)-MBI, (e) BTA loaded halloysite with Cu-stoppers, and (f) BTA loaded halloysite with UF-stoppers. 137

ACKNOWLEDGMENTS

First of all, I would like to thank God and my parents for providing me the opportunity to study and do research at Louisiana Tech University. I would like to extend my gratitude to my advisor and mentor, Dr. Yuri Lvov, who has supported me throughout my doctoral research. I am also thankful to Dr. Elshad Abdullayev for his guidance during the initial stage of my PhD. My current advisory committee, Dr. Erez Allouche, Dr. Randall Null, Dr. James Palmer, and Dr. Leland Weiss, also deserve commendation. I cannot forget my fellow lab mates, those who have already graduated and those who are still pursuing their degrees, for their advice and assistance in the laboratory. Additionally, the IfM faculty and staff have always been there when I needed their assistance. Special thanks to Dr. Alfred Gunasekaran for his assistance in SEM, TEM and XRD analysis. I would also like to acknowledge Dr. Andre Zeitoun from Applied Minerals, Inc., for providing us with halloysite samples. Ms. Renata Minullina from Kazan State University deserves credit for helping us in research work for self-healing coatings. Mr. Giuseppe Cavallaro from University of Palermo, Italy, and Weng-On Yah from Kyushu University, Japan for their valuable support regarding halloysite characterization. I am thankful to Mr. Scott Graham from StormWall Industries, in Ruston, LA, for his valuable assistance for flame retardant project. This work was supported by research grants from organizations such as the National Science Foundation and the Louisiana Board of Regents.

CHAPTER 1

INTRODUCTION

Utilizing different types of nanoparticles for surface-coating composites is one of the emerging field of nanomaterials. Carbon nanotubes are among the most popular materials used by researchers in their composites because of their mechanical and electrical properties [4]. However, carbon nanotubes have many disadvantages including low availability, high cost, and toxicity to living organisms. There are other synthetic nanotubes which are also available in the market, such as metal nanotubes, which offer a simple method of synthesis, but are not available in the tons of final product needed for industrial applications [5]. Currently, there is no method that exists which can produce tons of these synthetic nanotubes in a short amount of time, and at a low cost.

In our study, we explored natural clay nanotubes – Halloysite. Halloysite belongs to the family of phyllosilicate clay minerals which also includes kaolinite. Halloysite nanotubes are formed in natural deposits from the kaolinite due to the hydrothermal process over a period of millions of years [2]. Halloysite tube layers are separated from each other by water monolayer in the interlayered spaces [3]. Halloysite has chemical formula $\text{Al}_2\text{Si}_2\text{O}_5(\text{OH})_4 \cdot 2\text{H}_2\text{O}$, and upon heating at a higher temperature, it loses hydroxyl ions in the interlayered spaces [6]. Halloysite is a naturally occurring clay mineral available in thousands of tons and it is mined in China, New Zealand, Turkey, and the USA [3]. The diameter of a naturally occurring halloysite nanotube ranges from

40-60 nm. Its length varies between 1-1.5 μm , and the inner diameter ranges from 10-15 nm [2], [3], [7]. Halloysite is proposed for many different applications. It has been historically used as a raw material for the ceramics industry, especially for manufacturing porcelain and bone china [3][8]. When the halloysite is admixed with Nylon 6 fibers, the resulting composite has better flame retardant properties [9]. Halloysite can also be used as a template for the synthesis of metalized ceramic core-shell nanoparticles which improved the mechanical properties of the composites [6]. The porous morphology of halloysite has an added advantage of high catalytic activity, and therefore halloysite is used in the petroleum refining industries as well as for the separation of liquid and gaseous mixtures [3]. Halloysite does not need exfoliation and is easily dispersed in polymers like polyamide, which shows improved mechanical properties such as storage modulus and linear viscoelasticity [10].

1.1 Nanocontainers for Active Agent Storage

Different types of containers have been synthesized and utilized for the encapsulation of active agents. These include encapsulation by sol-gel processing, nanocapsules such as silica nanoparticles, and polyurethane microcapsules. Other types of containers include nanotubes such as halloysite, imogolite, and carbon nanotubes.

Sol-gel processing provides excellent transparency that can be used for the development of optical sensors by encapsulating matrices [11]. Also, sol-gel films have high chemical and biological stability. Silica nanoparticles are also commonly used for the encapsulation of different types of active agents. They have also been employed for the encapsulation of anticorrosion agents [12]. However, these types of nanoparticles exhibit a miniscule loading efficiency of 0.5-1 wt%.

The next class of containers includes nanocapsules which trap the active agents, and upon external pressure rupture, releasing the active agents. Polyurethane microcapsules have been used for the encapsulation of anticorrosion agents [13]. These microcapsules are effective for storage and can be mixed with different types of paint media. These microcapsules, upon rupturing, release the anticorrosion agents, and induce self-healing of the damaged surface. Another class of encapsulating vessels include polymeric microcapsules which are synthesized by depositing polymeric layers onto a sacrificial template, and is often utilized for drug delivery [14]. Microcapsule based nanocontainers have lower loading efficiency compared to halloysite nanotubes [15]. Also, the microcapsules are easily ruptured by external forces, resulting in the premature release of the active agent. Other examples of microcapsules include alginate particles [16] and liposomes [17].

The third class of encapsulating containers is nanotubes. Halloysite belongs to this class of vessels. Other examples of nanotubes include carbon nanotubes [18] and boron nitride nanotubes [19]. Although some microcapsules have higher active agents loading efficiency, nanotubes often have higher active agent retention time and a longer controlled release period [15][20]. In the case of halloysite nanotubes, an average release time of 10-20 hrs can be extended to hundreds of hours by the formation of tube end stoppers [21]. The loading efficiency of pristine halloysite of ca 10 wt% is increased in this study to 30-40 wt% make it comparable with the best polymeric microcapsules (Chapter 4). The tube end stoppers are formed from metal-organic complexes and a polymerization reaction [22].

The first two classes of nanocontainers are difficult to prepare in large amounts. In contrast, halloysite nanotubes are available in natural deposits in thousands of tons and are also biocompatible [23]. Halloysite have been used for the delivery of different types of active chemical agents such as anticorrosive agents [21] and sustained drug delivery [24]. Halloysite has also been used for the reinforcement of polymer composites to improve the mechanical properties and flame retardancy of the polymer [9]. The results presented in this study highlight the application of halloysite nanotube as a reservoir and delivery system of anticorrosion agents for the protection of steel surface from corrosion. Halloysite at 5-10 wt% was admixed with latex and polyurethane paints and the anticorrosion and flame retardance property are analyzed.

1.2 Research Goals

The objective of this study is to use the halloysite nanotubes as a nanocontainer for protective coatings based on polymeric paints. We concentrated on the following objectives during the research:

1. Use of halloysite nanotubes for encapsulating different anticorrosive agents. Optimization of anticorrosive release time with formation of halloysite nanotubes tube end stoppers slowed the release rate from tens to hundreds of hours (using metal-organic complexation and polyurethane organic stoppers).
2. Increasing halloysite nanotubes active agents loading efficiency from 10 to 30 wt% by increasing the inner lumen diameter by acid etching the inner lumen with sulfuric acid. Comparison of the pristine and acid treated halloysite loading efficiency by analyzing release profiles of active chemical agents.

3. Optimization of the addition of the selected anticorrosive agents encapsulated in halloysite into polymeric paint, and analyzing the strength, adhesion and protective properties of this composite as a surface coating.
4. Admixing halloysite with latex paint, and applying it on metal and flake boards, and testing for flame retardant properties. Loading halloysite with a commercial paint flame retardant to achieve synergy between the two components. The coating burn resistance (flame torch tests) is tested, and testing the latex paint-halloysite composites.
5. Extension of clay nanotubes coating method for encapsulation of fly ash microparticles with halloysite nanotubes using the Layer-by-Layer (LbL) technique, and optimizing these microcore-nanoshell concrete samples for extended curing time (parameter which is much needed in industry) at room temperature and at higher temperatures.

1.3 Dissertation Overview

The dissertation is divided into six chapters. The first chapter covers the background on the halloysite nanotubes, including their structure, surface properties, and some applications.

The second chapter describes increasing the halloysite's lumen diameter by reacting with sulfuric acid. Halloysite nanotubes are mixed with sulfuric acid solutions prepared at different concentrations and at different temperatures. Changes in the lumen diameter at different acid concentrations and temperatures are analyzed using SEM, TEM, and solid state NMR. Change in the internal and external diameter upon exposure to the halloysite is also analyzed. Improved loading efficiency for the acid treated

halloysite is proved by analyzing release profile for benzotriazole and comparing it with acid untreated halloysite.

The third chapter is on the application of halloysite nanotubes as a nanocontainer for loading of anticorrosive active agents. These selected active agents include Benzotriazole (BTA), 2-Mercaptobenzothiazole (2-MBT), and 2-Mercaptobenzimidazole (2-MBI). These active agents are loaded into halloysite in a vacuum chamber. Anticorrosive properties of the acrylic paint are tested by admixing these active agents loaded halloysite, and then applying onto ASTM A366 steel plate surface. Active agents release is further controlled by forming tube end stoppers using metal-organic stopper and polyurethane organic stoppers.

In the next chapter, halloysite is loaded with a dodecylamine (commonly used anticorrosion agent for steel), and its release profile is analyzed in water and in a paint thinner, xylol. Controlled release of dodecylamine is further extended by the formation of tube end stoppers. This time inorganic metal ion based tube end stoppers and organic polymer based tube stoppers are implemented and compared by analyzing their dodecylamine release profile. Three types of halloysite nanotubes are used: normal pristine halloysite, lumen enlarged acid treated halloysite, and base treated halloysite.

In the fifth chapter, clay nanotubes application as a flame retardant is explored by 5-10 wt% doping of latex paint with halloysite nanotubes. The halloysite is loaded with a commercial flame retardant additive, FR-1, and mixed with the latex paint. The samples are compared by applying these paint sample on wooden flake blocks, and burning the samples using a BenzomaticTM flame torch (in collaboration with Stormwall Industries, Ruston, LA). Flame retardant property of the paint is also analyzed by applying the paint

on ASTM A366 steel metal surface, and burning them using the same flame torch. Flame retardant property was analyzed based on ASTM E84 test which covers standards based on surface appearance before and after the flame test, sample flame spread and smoke development.

In the final chapter halloysite coating on the fly ash particles is developed to extend the curing time for geopolymer cement (a disclosure was filed to LaTech and the patent application on this technology is in preparation). Anionic halloysite nanotubes were coated on fly ash particles using the Layer-by-Layer (LbL) technique through sequential deposition with polycations. Fly ash surface is coated with halloysite alternated with polycation, polyethylenimine (PEI) and a polyanion, and polyacrylic acid (PAA) to get multilayer protective shell. Halloysite coating on fly ash surface is visualized using SEM. Halloysite is mixed with untreated (positive) or LbL-treated fly ash microparticles in dry state, and change in setting time is analyzed using rheology tests (in collaboration with TTC researcher Dr. C. Montes).

CHAPTER 2

BACKGROUND AND THEORY

In this chapter the chemistry and structural characteristics of the halloysite nanotubes will be discussed. This chapter explains how the chemistry of the halloysite allows it to store different types of active agents into its lumen. This chapter will also explain the different applications of halloysite nanotubes, concentrating mostly on its application as a nanocontainer for drugs, proteins, and anticorrosive agents.

2.1 Chemistry and Structural Characterization of Halloysite

Halloysite is an environmentally friendly, naturally occurring clay mineral available in hydrated form, and it has the chemical formula $\text{Al}_2\text{Si}_2\text{O}_5(\text{OH})_4 \cdot n\text{H}_2\text{O}$. Chemically, halloysite is similar to kaolinite except that halloysite has an additional water monolayer present between the interlayered spaces. Based on the number of water molecules present in the halloysite interlayered spaces, $n = 2$, this type of halloysite mineral is called halloysite-10 Å, or hydrated halloysite, and is larger than kaolinite. Hydrated halloysite can be converted irreversibly into a dehydrated form easily by heating at high temperatures [1-3]. The dehydrated form of halloysite has an interlayered spacing of 7 Å, and has a chemical formula $\text{Al}_2\text{Si}_2\text{O}_5(\text{OH})_4$ [3].

According to some scientists, the halloysites are present in nature in two forms: hydrated and dehydrated halloysites. Upon heating at high temperature, halloysite-10 Å

changes to halloysite-7 Å due to loss of water molecules. However, it has been debated that the halloysite could be present in halloysite-10 Å form and halloysite-7 Å form separately because of irreversibility in the transformation [25][26]. According to X-ray diffraction studies by Churchman *et al.*, he concluded that during the dehydration process, the value of n (number of water molecules) changes from 0 to 2, therefore suggesting that halloysite exists in only 2 phases, hydrated and dehydrated phase, dehydrated state being the later stage [27].

Pure halloysite nanotubes are white in color and can be easily processed into powder as shown in Figure 2-1 a and b. Halloysite clay sometimes contains metal ions such as Fe^{3+} and Cr^{3+} and Ti^{2+} in the form of impurities, and therefore give halloysite a yellowish to brown and sometimes a greenish appearance [3].

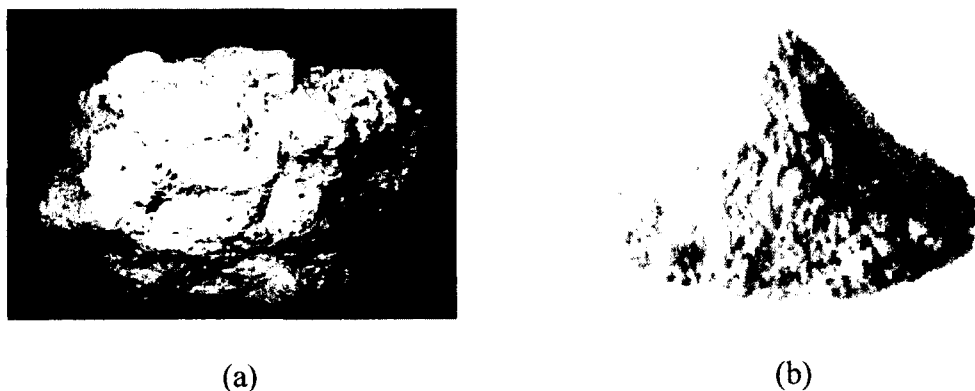


Figure 2-1: Halloysite mineral in rock form (a), and processed form (b).

Elemental analysis suggests that the halloysites have a higher percentage of iron oxide as a common impurity [3]. The presence of iron oxide could be associated with the presence of iron oxide related minerals such as hematite or meghamite may be because of isomorphous substitution of Fe^{3+} for Al^{3+} in the octahedral alumina sheet. However,

elemental analysis has suggested that Fe^{3+} does not substitute for Si^{4+} in the tetrahedral sheet of halloysite as shown in Figure 2-2.

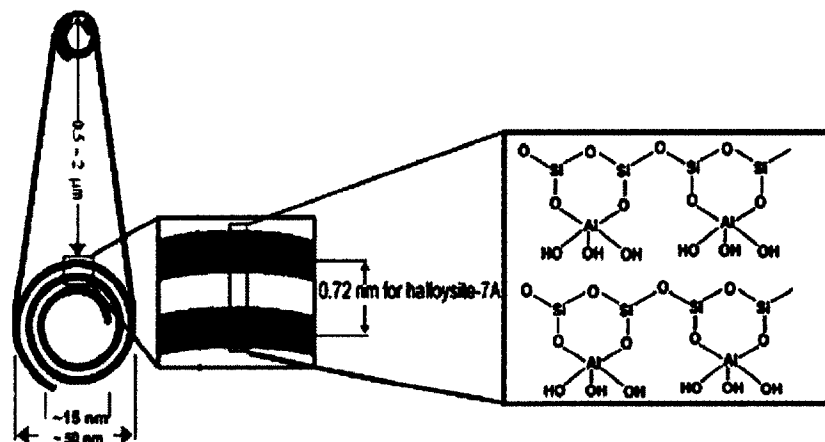


Figure 2-2: Representation of halloysite structure: side view and top view of the halloysite layer [22].

Baral *et al.*, has explained the process for the purification of raw halloysite rock [6]. Halloysite is first grinded with water into a slurry and then passed through a sieve of a size $125\ \mu\text{m}$. It is then suspended in water, followed by centrifugation. The precipitant is mixed with a solution of $0.5\ \text{M}$ EDTA (ethylenediaminetetraacetate) for 24 hrs. This results in a white wet solid, which can be air dried at room temperature.

Halloysite nanotubes are composed of alternate layers of aluminum and silica oxides: aluminum consisting the inner layer, and silica oxide is on the outside layer [1-3]. The halloysite nanotubes are formed because of the process of weathering and hydrothermal processes [2][3][28]. The hydrothermal and weathering process results into two types of minerals, an irreversible form of dehydrated Halloysite-7 Å, and a hydrated form of Halloysite-10 Å [2-3]. The outside diameter of the halloysite nanotubes ranges from 50 to 200 nm, with an average outer diameter value of 70-75 nm [1]. The lengths of

the halloysite nanotubes range from 0.5 to 5 μm [1-3]. The values of the outside diameter and the lengths of the halloysite nanotubes depend on its origin.

Halloysite has a monoclinic crystal structure, and has unit cell dimensions [29]:

$$a = 5.14 \text{ \AA}, b = 8.9 \text{ \AA}, c = 20.7 \text{ \AA}, \beta = 99.7^\circ, \text{ for halloysite-10\AA}$$

$$a = 5.14 \text{ \AA}, b = 8.9 \text{ \AA}, c = 14.6 \text{ \AA}, \beta = 101.9^\circ, \text{ for halloysite-7\AA}$$

where a corresponds to the tube axis and c corresponds to the axis normal to the tube [1] [30]. The difference in the unit cell dimensions indicate that upon dehydration there is only change in the interlayer spacing of the halloysite nanotubes. Constant values of a and b suggest that there is a preservation in the halloysite shape along the lateral dimensions. Upon dehydration the overall diameter of the halloysite nanotubes increased by 10-15% [3] [29].

Figure 2-3 shows the X-ray powder diffraction spectra for the halloysite nanotube samples. A Cu-K α radiation source is used for obtaining the spectrum.

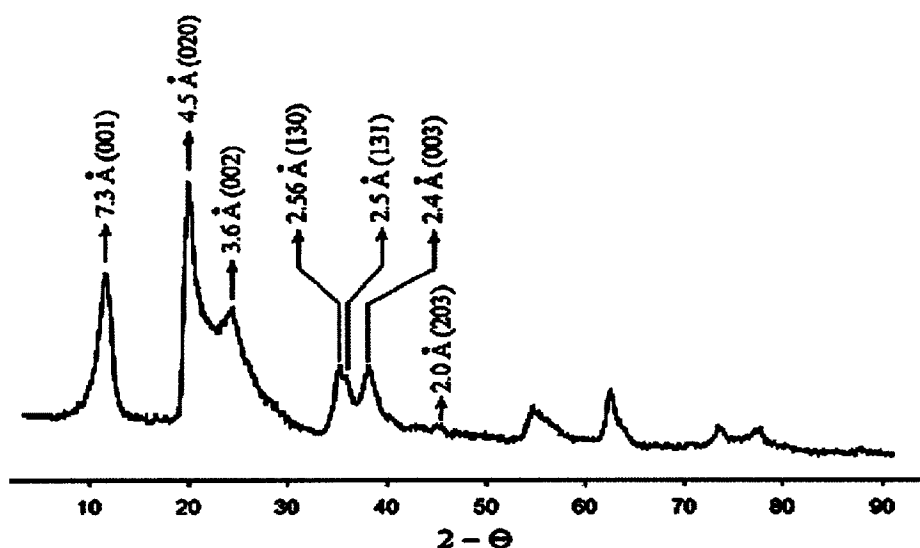


Figure 2-3: X-ray powder diffraction pattern for halloysite sample.

For the first order basal reflection, the interlayer distance is clearly visible with a broad peak at 7.3 Å. The second order basal reflection is indicated by a peak at 3.6 Å [31]. When compared with the stacked kaolinite sheets, this peak is broader for the halloysite nanotubes. This is because the rolled multilayered structure of halloysite have less crystallinity than the stacked sheets of kaolinite. In the case of kaolinite, the peak for the crystallinity corresponds to 7.2 Å spacing [32]. The tubular structure of halloysite clay nanotube is indicated by a distinctive high intensity peak at 4.5 Å [33].

Figure 2-4 is the scanning electron microscope (SEM) images of the halloysite nanotubes. These images show the tubular morphology of the halloysite nanotubes. The inner lumen of the halloysite nanotubes is clearly visible in the transmission electron microscope (TEM) image of the tubes. This varying chemistry of the halloysite nanotubes makes it an interesting material for their implementation in different applications.

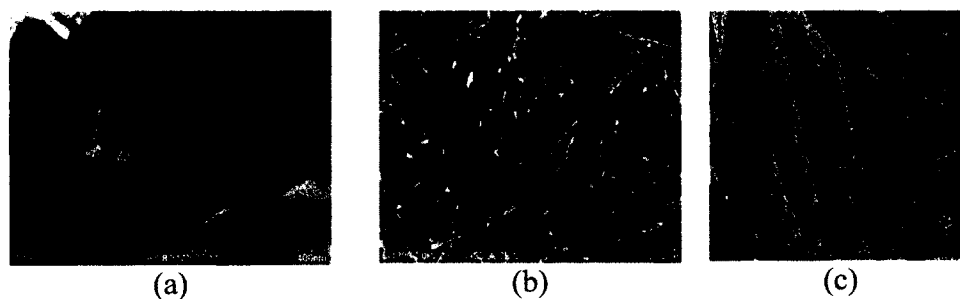


Figure 2-4: SEM and TEM images of halloysite nanotubes. a) TEM clearly shows the layered morphology of halloysite nanotubes, b) SEM of halloysite samples from Xinjiang province, China, and c) inner lumen is clearly visible with a TEM of nanotubes.

In the case of halloysite nanotubes, silica oxide makes up the outer layer, and aluminum makes up the inner lumen surface [3]. This different surface chemistry of the

halloysite surfaces makes it an interesting material for its application as a nanocontainer. The different chemical properties of the inner and outer surfaces of the halloysite are also proved by the measurements of surface charge [23]. As shown in Figure 2-5, halloysite surface charge is comparable with that of pure silica, as it follows a trend of change in zeta potential into the negative range with an increasing pH. In the case of alumina, the surface charge becomes negative at a pH of 8.5. This allows selective loading of different types of negatively charged active agents into the halloysite lumen [21][34].

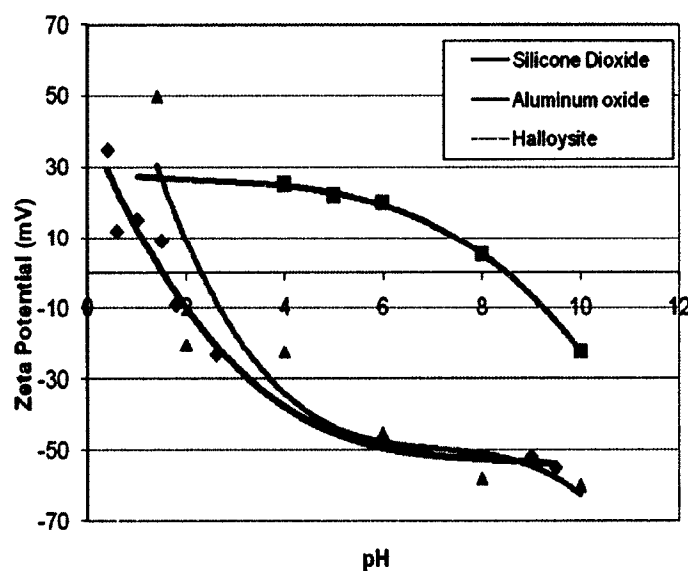


Figure 2-5: Comparison of halloysite nanotubes surface charge with silicon dioxide (blue) and aluminum oxide (red) from ζ -potential analysis [23].

2.2 Biocompatibility of Halloysite nanotubes

In recent scientific studies, concentration is not only on synthesizing or implementing economically viable material, but also on environmentally friendly materials. These materials should do their work with more effectiveness without compromising the environmental safety. In the case of halloysite nanotubes, occurring

naturally is an environmentally safe clay mineral, and therefore can be used as a nanocontainer. A cytocompatibility study conducted by Vergaro *et al.*, showed that halloysite nanotubes are safer than a normal table salt at a concentration of 75 $\mu\text{g/ml}$ where most of the cells die [23]. As shown in Figure 2-6 in the case of halloysite nanotubes for MCF-7 and HeLa cells, the viability percentage is about 50% after exposure to halloysite nanotubes at a concentration of 100 $\mu\text{g/ml}$.

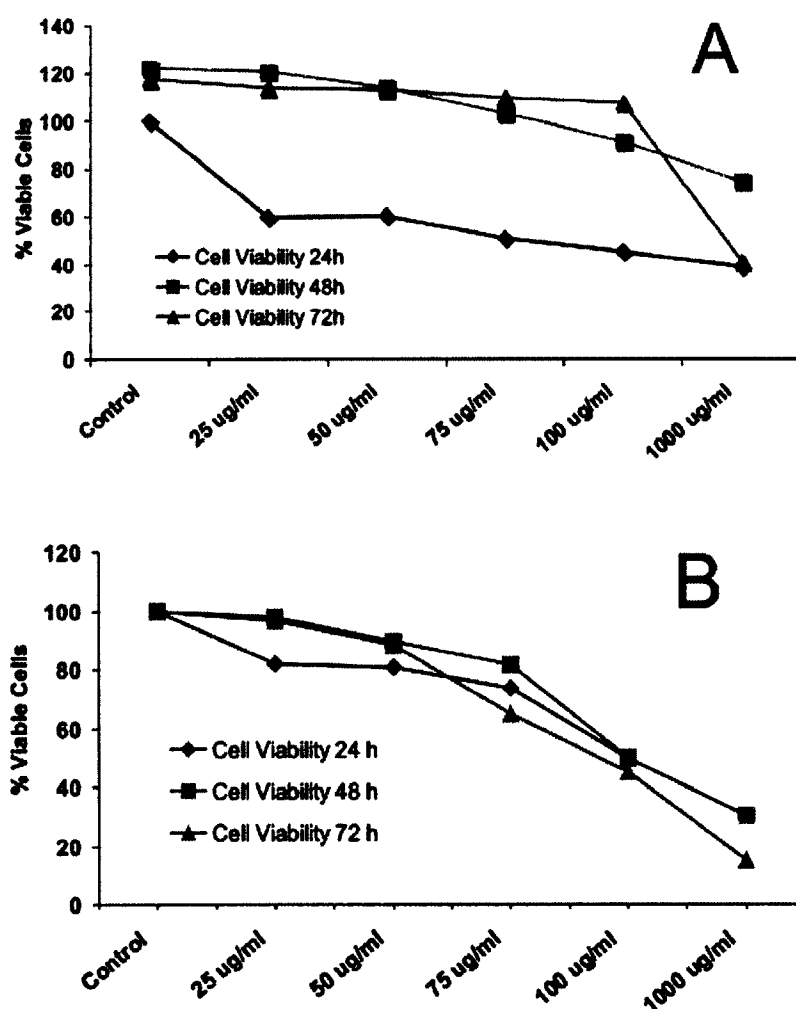


Figure 2-6: Halloysite cytotoxicity testing on A) MCF cells, and B) HeLa cells at different concentrations and exposure times [23].

2.3 Implementation of Halloysite Nanotubes as a Nanocontainer for Active Agents

Halloysite nanotubes with alternate structural chemistry and biocompatibility property make it an interesting nanocontainer for active agents. For the active agents encapsulation halloysite is mixed with a solution of the same material to be loaded. However, these active agents can get adsorbed on the external and internal walls of the tubes [31][35][36], may be intercalation [3][37][38][39], and the substances loaded into the halloysite lumen, which get crystallized into the pores [40]–[42].

Carr *et al.*, conducted intercalation study on halloysite interlayered spacing with different types of salts, and they found that in particular potassium and ammonium salts get intercalated into the interlayered spacing more efficiently than the lithium and sodium salts [43]. Not only salts but also some of the organic substances are shown to have intercalated into the halloysite interlayered spacing [3][39][44]. Intercalation is mainly attributed to the presence of water molecules between the layers, and therefore, this phenomenon is mainly observed in hydrated halloysite, and is partially or completely absent in dehydrated halloysite [39]. According to Frost *et al.*, intercalation can be divided into mainly two types. In the first type of intercalation, strong hydrogen bonds form between the silicon tetrahedral sheet [39]. These hydrogen contributing compounds include urea and other compounds with -NH_2 or -OH functional groups. The second type of intercalation involves interaction of interaction of alkali metals substances which interact with the inner alumina layer, and the acetates which interact with the silica layer because of a strong dipole moment. Halloysite intercalation provides an advantage of water treatment because it can absorb a large amount of material due to a higher surface area.

To act as a nanocontainer, we are more interested in using the halloysite lumen for the encapsulation instead of its surface as an adsorbing material for active agents. Halloysite lumen functions as a storage unit for the active agents. Abdullayev *et al.* showed that the active loading efficiency of the halloysite lumen can be improved by selective etching of the inner layered alumina surface [45]. Figure 2-7 shows the scheme of active agents loading into halloysite [46]. Halloysite nanotubes are mixed with a concentrated solution of compound to be loaded into the halloysite under the effect of vacuum [21], [46], [47]. Halloysite powder is mixed with a concentrated solution of compound desired to be loaded into the halloysite. The compound with a higher solubility in a solvent, which can form a stable colloid solution with halloysite, is advantageous. The solvent should be non-viscous, and should not alter the properties of the compound to be loaded into the halloysite. Some of the commonly used solvents include water, acetone and ethanol [21][48]. Solvents with lower viscosities are preferred because with fast drying solvents it also increases the concentration gradient between the lumen and the external solution. After adding the halloysite into the solution, the sample is sonicated for 20 minutes to break the halloysite agglomerates and to form a stable solution. The beaker containing the solution is then transferred into a vacuum chamber, and is evacuated using a vacuum pump. A vacuum cycle of 30 minutes is repeated 2 to 3 times for improved loading, and then removed to atmospheric pressure. A fuzzing sound indicates that the air bubbles are being removed from the halloysite, and the air inside the lumen gets replaced by the concentrated solution of solvent, and partial crystallization of the compound occurs inside the pores. Finally, the sample is washed with the solvent

used for loading to remove excess of the compound which may get adsorbed on the halloysite externally.

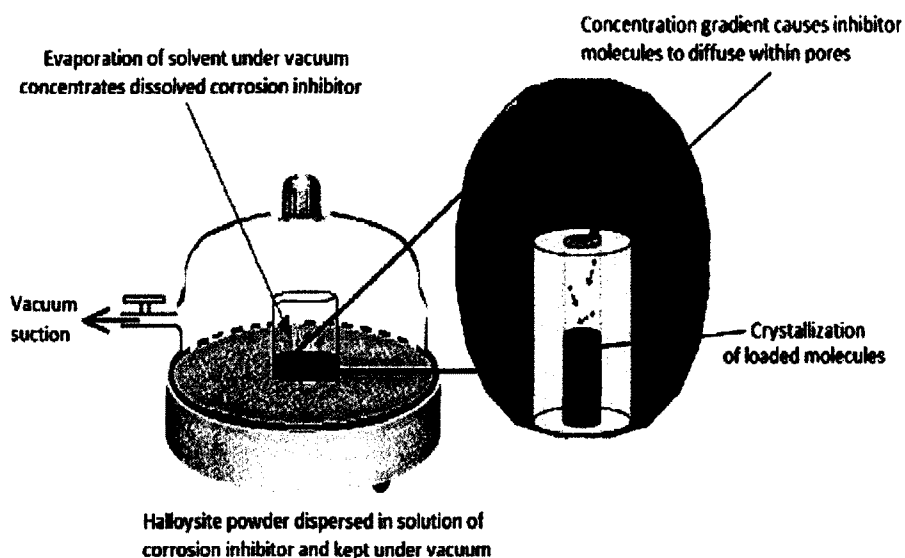


Figure 2-7: Scheme of halloysite loading using vacuum suction [46].

2.4 Halloysite as a Nanocontainer for Drugs

This biocompatible property of halloysite nanotubes makes it advantageous as a nanocontainer for drugs, proteins, and other biological agents. Halloysite nanotubes can be used for the biological application without any need of special processing. A study conducted by Vergaro *et al.*, showed that halloysite can be used as an nanocontainer for a polyphenol, resveratrol [49]. With increasing concentration of the drug loaded into the halloysite and with increasing exposure time, the cancer cell cytotoxicity increases leading to apoptosis. The halloysite nanotubes' surface area provides good anchoring for selective capturing of the leukemic cells, thereby enhancing the cell capture by isolation from normal cells [50]. Halloysite can be easily electrospun with other polymers such as poly(lactic-*co*-glycolid acid) to synthesize the fibers, where halloysites are loaded with a

drug [51]. The advantage of this system is that the halloysite can store the drug for a longer time, and sudden release of the drug can be avoided. Halloysite application as a drug delivery agent has been further extended for gene therapy applications [52]. Halloysite modification with γ -aminopropyltriethoxysilane (APTES) can be used as a delivery agent for an antisense agent, oligodeoxynucleotides (ASODNs), as a therapeutic gene for targeting survivin, a cancer inducing protein. Halloysite upon loading with an opioid Fentanyl shows promising application as a high potent drug for oral intake [24]. Halloysite nanotubes have also been used in the preparation of polymeric composites for artificial bone cement [53]. It is observed that with the addition of 5 wt% of halloysite into poly(methyl methacrylate) polymer (PMMA), the tensile strength of the composite increases significantly when compared to the control samples. It was observed that along with increasing the tensile strength of the bone cement, halloysite can also be used as an encapsulating agent for an antiseptic, gentamicin, which prevents infection (Figure 2-8).

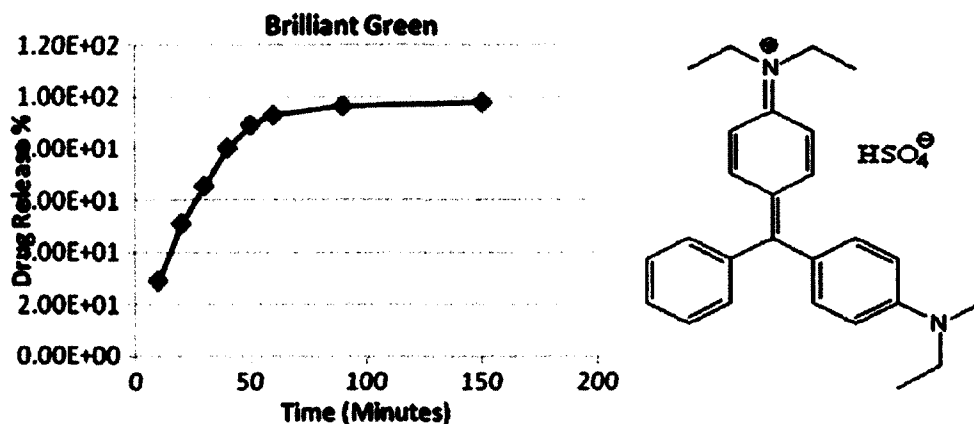


Figure 2-8: Release profile for gentamicin loaded into halloysite (left) and chemical formula for gentamicin (right) [54].

Halloysite offers extended controlled release time for the drugs loaded into the lumen. Lvov *et al.* showed that for some of the drugs such as Dexamethasone,

Furosemide, and Nifedipine, the release time is up to 10 hrs with about 60% of the drug released in 5 hrs [55]. For the pure drug crystals, 100% release is observed within 30 minutes (Figure 2-9). Price *et al.* also reported a similar phenomenon when he loaded tetracyclin HCl drug into halloysite, and compared it with the dissolution of a pure drug [48]. Biocompatibility of halloysite therefore offer halloysite nanotubes as an alternate nanocontainer for drug storage and controlled release.

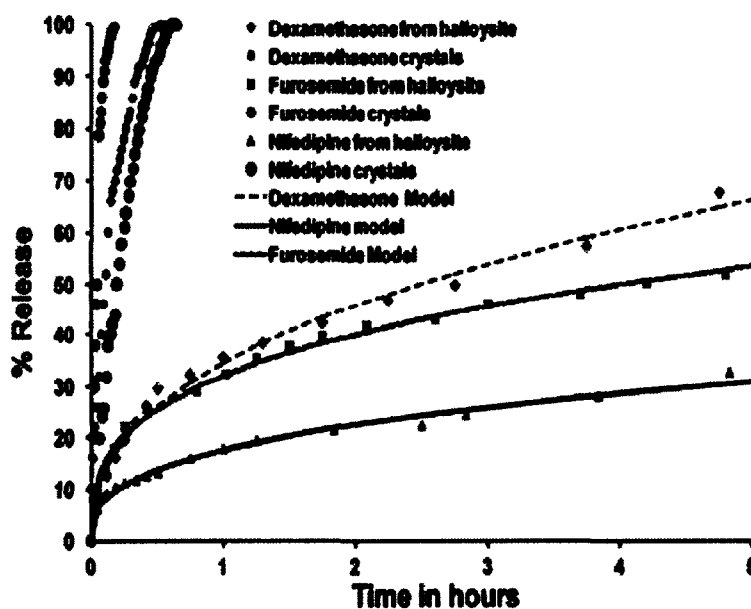


Figure 2-9: Comparison of Release profiles for pure drugs Dexamethasone, Furosemide and Nifedipine crystals and drugs loaded into halloysite [55].

2.5 Halloysite Nanotubes for the Encapsulation of Anticorrosive Agents

One of the important application of halloysite nanotubes is its use as a nanocontainer for anticorrosive agents. Abdullayev *et al.* showed that when the halloysite nanotubes are loaded with benzotriazole and admixed with an industrial paint, it significantly improves the anticorrosive properties of the paint matrix [21]. Halloysite nanotubes have a loading efficiency 4.5% of the weight of halloysite, when loading is performed in acetone. Halloysite nanotubes loaded with benzotriazole are compared with the sol-gel based coatings to check surface protective activity. The samples are exposed to the corrosive environment for 24 hrs to measure the anodic corrosion activity. It is observed that anodic corrosion on the sol-gel based coatings increases rapidly in a few hours, leading to a pitting type of corrosion [21]. When the halloysite nanotubes admixed acrylic paint coated on copper metal wire is exposed to a corrosive environment, the concentration of Cu^{2+} ions corroded is significantly decreased than the controlled sample [22]. As shown in Figure 2-10, release of the anticorrosive agents from the halloysite can be further controlled by the formation of tube end stoppers. In the case of halloysite loaded with benzotriazole without stoppers, about 90% of the release is achieved in 8 hrs. When Cu-BTA stoppers are used to control the release 70% of the release is achieved in 8 hrs. The release can be further controlled by increasing the concentration of Cu^{2+} ions.

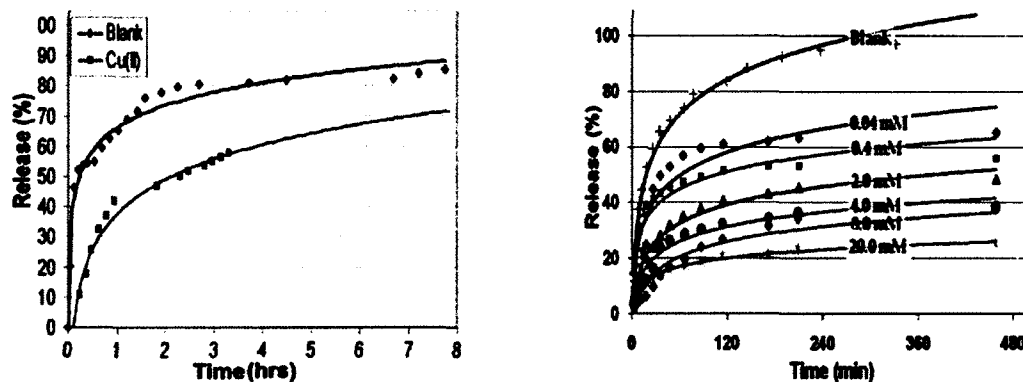


Figure 2-10: Release profiles for Benzotriazole loaded halloysite nanotubes with and without stoppers (a), and change in controlled release with increasing Cu^{2+} ions concentration [21].

Halloysite nanotubes not only provide anticorrosive property to the paint, but it also increases the mechanical strength of the coating. As shown in Figure 2-11 for the stress-strain relationship for controlled samples and paint with halloysite nanotubes. The comparison shows that for the pure paint sample the shear stress for the samples improved significantly with the addition of halloysite nanotubes [21].

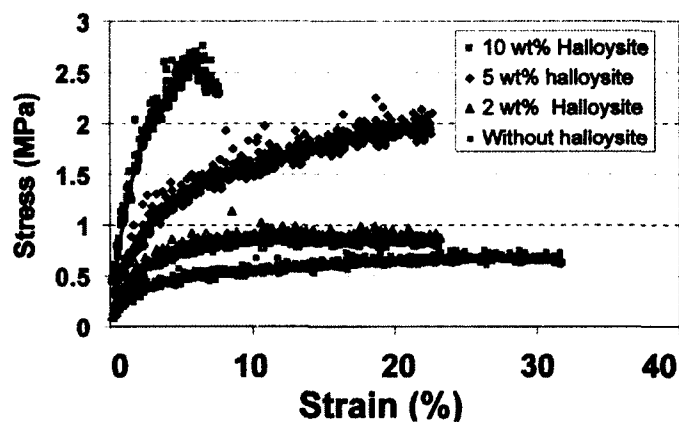


Figure 2-11: Comparison of stress-strain relation for acrylic paint with and without doping with halloysite [21].

Along with benzotriazole, other anticorrosive agents such as 2-mercaptobenzothiazole (2-MBT) and 2-mercaptobenzimidazole (2-MBI) are also

successfully loaded into halloysite [46] [54]. Shchukin *et al.* also showed that halloysite nanotubes can be used as a nanoreservoir that provides effective storage and extended release of anticorrosive agents [12].

2.6 Application of Halloysite Nanotubes for Flame Retardant Coatings

Halloysite nanostructure offers an advantage by increasing the mechanical properties, as well as increased thermal stability and increased flame retardancy [10]. In the past few years, a great deal of interest has been toward synthesizing polymer-clay based composites which seem to have good flame retardant properties. Halloysite nanotube structure provides a flame retardant effect similar to that of halogen based flame retardants, except that the halloysite nanotubes are biocompatible in nature. Du *et al.* reported that the flame retardancy of the polypropylene (PP) is increased significantly after doping with halloysite nanotubes [56][57]. Halloysite nanotubes encapsulate the degradation products in their lumen, which results in the improved resistance towards thermal decomposition [47]. Similar results were reported by Prashantha *et al.* where they showed that by increasing the concentration of halloysite nanotubes in polypropylene polymer matrix Nylon 6 fiber has inherently good flame retardant properties; however, when the fibers are burned in the presence of air, it results in dripping because of intense flammability causing ignition, thereby increasing the risk of a fire hazard [9]. When the Nylon 6 is incorporated with halloysite nanotubes, it forms a thermal insulating barrier on the surface which decreases the rate of burning. Jing *et al.* reported that upon hydrophobization of halloysite lumen by loading with diphenyl phosphate, it has a release time up to 60 hrs, and it can be used as a flame retardant composite [58].

2.7 Halloysite Nanotubes for Encapsulation of Metal/Inorganic Substances

Halloysite nanotubes can be utilized as a template for the chemical reduction of metal ions, and therefore it provides an electroless solution for the synthesis of metal-halloysite nanocomposites [6]. Halloysite have been used for the deposition of different types of metals such as nickel and gold [6][59]. Baral *et al.* showed that Ni^{2+} ions can be deposited on the surface of halloysite nanotubes by using Niposit468 nickel plating bath in the presence of palladium as a catalyst for the reduction of nickel [6].

Halloysite nanotubes can be loaded not only with organic substances but also with organic substances. Silver nanorods can be synthesized inside a halloysite lumen by thermal decomposition of silver acetate [60]. The formation of silver nanorod inside the halloysite lumen is proven from STEM-EDX analysis. This halloysite-silver composite is mixed with the paint, and it has antimicrobial properties. When mixed with the paint it also increases the mechanical properties of the paint (Figure 2-12 a and b).

Halloysite nanotubes can also be loaded with other inorganic substances such as sodium tetrachloropelladate, a catalyst that can be used for the metallization of halloysite nanotubes (Figure 2.12c) [54]. Halloysite can also be loaded with potassium permanganate, which gets deposited on both surfaces, inside into the lumen and also on the external surface (Figure 2.12d). Halloysite- TiO_2 thin films can be prepared on a glass surface by utilizing the sol-gel method, which have photocatalytic properties when studied on basic Blue 41 Azo dye in water [61].

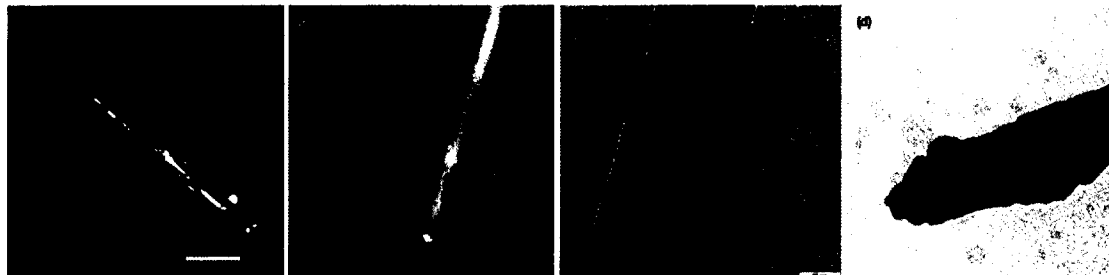


Figure 2-12: Inorganic substances loaded into halloysite lumen; silver (a,b), sodium tetrachloropelladate (c), and potassium permanganate (d) [54].

Shchukin *et al.* showed that halloysite nanotubes can be loaded with calcium carbonate, where carbonate ions are produced by a reaction between urease enzyme and calcium ions [7]. The urease enzyme is loaded into the halloysite nanotubes following the scheme showed in Figure 2-7 from the external bulk solution. The urease therefore releases the carbonate ions into the pores of the halloysite nanotubes. These tubes are then mixed with a solution containing calcium ions which causes the deposition of carbonate inside the pores. The precipitation of carbonate inside lumen is proven by the TEM and SEM images (Figure 2-13).

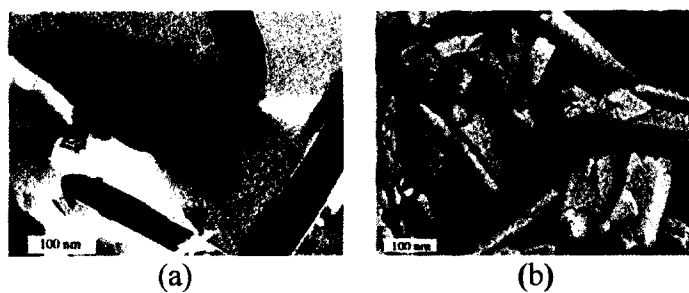


Figure 2-13: Carbonate deposited into halloysite lumen indicated by TEM image (a), and on the tube end by SEM (b).

2.8 Applications of Halloysite Nanotubes

Other applications of halloysite nanotubes include preparation of polymer nanocomposites and as a catalyst in the petroleum industry.

2.8.1 Halloysite-polymer nanocomposites

Polymer-clay based nanocomposites are one of the emerging areas in the field of polymer based on their usefulness in improved tensile strength, flame retardancy, and lower cost [9][10] [56][57][62][63]. Therefore, these nanocomposites have been used for different applications in drug delivery, sensor applications, and medical devices [57][63][64].

Polymer composites made with platy clays are the most commonly used materials because of their easy and abundant availability in nature [65][66]. It is desirable that for the halloysite nanotubes to be used in the polymer nanotubes they should be exfoliated, i.e. each nanotube should be separate [63]. One of the drawbacks of the clay mineral in polymer nanocomposites is their surface hydrophilicity; therefore, they need to be hydrophobized before admixing with the hydrophobic polymers. Hence, the nanotubes are processed with surfactants or silanating compounds to make the clay surface hydrophobic in nature [63][67].

Halloysite nanotubes do not require longer processing compared to the platy clays such as kaolinite, and therefore, their implementation in polymer composites is promising [63][68]. Addition of halloysite nanotubes into the polypropylene seems to have improved the flexural modulus of the composite by 35%, whereas tensile strength is improved by 6% [69]. Along with polypropylene other polymers such as epoxy,

polyamide polymer nanocomposites have benefitted from the halloysite additives [10][57].

Halloysite-polymer composites are prepared in different ways. In one of the methods, halloysite nanotubes are dispersed in a monomer solution followed by *in situ* polymerization, where monomers react with the external surface of halloysite nanotubes, and result in a uniform suspension. This *in situ* polymerization takes place in the presence of heat or light, and therefore, it does not require a solvent [67]. In the second method, halloysite nanotubes are mixed with a polymer matrix in a solvent and the mixture is sonicated for the exfoliation of the halloysite nanotubes, which results into a uniform suspension. Later the solvent is evaporated, which results into a halloysite-polymer composite [63][67].

The third method for the preparation of halloysite-polymer composite involves mixing the polymer matrix with the halloysite in molten form, which results in halloysite exfoliation in the polymer matrix. This method is simple, but it results in clay agglomerates because of poor distribution of polymer molecules into the clay matrix. Some of the composite examples include halloysite-polyamide and halloysite-terephthalate [57].

2.8.2 Halloysite as a hydrocarbon conversion catalyst

Halloysite nanotubes have been used as a hydrocarbon conversion process in the petroleum industry [70][71]. Halloysite nanotubes have a higher Al/Si ratio compared to the other clay minerals, which results in the cracking of the hydrocarbon as the residual aluminum oxide provides acidic sites. These acidic sites act as a catalyst for the heterolytic breakage of chemical bonds resulting in unstable carbocations, which undergo

a chain rearrangement, and C-C scission by hydrogen transfer. This scission reaction generates highly reactive ions which promotes the cracking process [72]. The advantage of using halloysite as a catalyst is that it produces hydrocarbons with a higher concentration of sulfur [73].

Because of this advantage, halloysite drew the attention of researchers for its application as a hydrocarbon catalyst. D. Santili patented the use of halloysite nanotubes as a binding agent for metal oxides such as Al, Mg, and Si for the hydrotreatment and hydrometalation of asphaltene, which contains hydrocarbons in the form of crude petroleum [73]. Efficiency of the hydrocarbon catalyst can be further improved with the addition of oxides of transition metals such as Cr, V and Fe. Deasphalting, a process where asphalt is separated from crude oil in the petroleum industry, can be improved using halloysite with pore sizes ranging from 20 to 70 nm. Deasphalting takes place faster in the presence of pure halloysite and halloysite doped with 5% of alumina, resulting in a higher surface area for the adsorption of porous catalyst.

Halloysite with nickel and magnesium impurities, termed as synthetic halloysite, are found to have higher efficiency in the cracking process. Higher efficiency of the synthetic halloysites is mainly because of the presence of iron impurity which acts as a poison in the cracking process [74].

2.9 Conclusion

Halloysite structure and some applications of nanotubes are described. Halloysite nanotubes are rolled kaolinite with a high aspect ratio of 25-30 with outer diameters ranging from 40 to 60 nm, diameters of lumen ranging from 10 to 20 nm, and the length of the tube is 1-5 μm depending on its source of the origin. Halloysite nanotubes offer

applications in different areas ranging in preparation of composites with polymers, doping paints for protective coating (anticorrosion, flame retardant agents), encapsulating drugs, antimolding agents, and their controlled release. Halloysite nanotubes can also be used as a catalyst for hydrocarbon cracking. The interesting chemistry of halloysite nanotubes enables them to be used for loading, storing, and sustained controlled delivery of the active chemical agents. Unlike other nanotubes (carbon, metal oxide), which are expensive and often toxic, halloysite nanotubes are available in nature in thousands of tons, and are biocompatible. Halloysite nanotubes do not require complicated processing or synthesis and it does not need exfoliation like other clay materials. Halloysite is easily dispersible in water and other polar solvents. These characteristics put halloysite nanotubes in a promising category for wide scale-up industrial applications ranging from biomedical materials, smart polymers and coatings, to petroleum industry and construction technologies.

CHAPTER 3

ENLARGEMENT OF HALLOYSITE CLAY NANOTUBE LUMEN BY SELECTIVE ETCHING OF ALUMINUM OXIDE

In this chapter an idea of improving halloysite loading efficiency by increasing the halloysite lumen diameter has been discussed. Halloysite nanotubes are treated with sulfuric acid (H_2SO_4) at different concentrations and temperatures to optimize the process kinetics. Mechanisms change in halloysite lumen diameter are analyzed using solid state-NMR, X-ray diffraction, FTIR, UV-Vis Spectroscopy and TEM. The sections in this chapter were written by the co-author in a published article: E. Abdullayev, A. Joshi, W. Wei, Y. Zhao, and Y. Lvov, "Enlargement of halloysite clay nanotube lumen by selective etching of aluminum oxide.," *ACS Nano*, vol. 6, no. 8, pp. 7216–26, Aug. 2012.

3.1 Introduction

Halloysite is a naturally occurring clay mineral with tubular morphology; its external diameter is of ca. 50 nm and an inner diameter of 10-15 nm. It has a chemical formula of $\text{Al}_2\text{Si}_2\text{O}_5(\text{OH})_4 \cdot 2\text{H}_2\text{O}$, which is similar to kaolinite, except for the presence of an additional water monolayer between the adjacent clay layers [1]–[3][54][55]. Unlike other tubular materials (such as boron nitride, metal oxide or carbon nanotubes halloysite is abundantly available natural nanomaterial, which makes it attractive for technological applications [75]. These clay nanotubes are environmentally friendly and are a

perspective biocompatible material for biotechnological research [23][76], [77].

Halloysite belongs to a family of clay minerals and can substitute kaolinite, montmorillonite, and bentonite as additives in material composites [57]. Because of its shape, halloysite material does not require long exfoliation processing due to the absence of the stacked platy sheets (contrary to the platy multilayer clays such as kaolinite).

Doping polymers with clay nanotubes remarkably improves the composites' mechanical properties as demonstrated for styrene-butadiene rubber [78], polyamides [10], epoxy resin [79], polypropylene [80], polymethylmethacrylate [53] and natural biopolymers [76].

Halloysite application as additive in polymer composites allows for synergetic strength increase accomplished with controlled sustained release of chemically and biologically active compounds loaded in their lumens. This promises functional polymeric nanocomposites with smart functions (anticorrosion [12][21][22], antibacterial [60], and self-healing [15]).

Many applications of halloysite are conditioned by its lumen size. Typical halloysite lumen volume is ca. 10 vol% of the tube and the pores' enlargement will allow higher amounts of active chemicals loaded with target capacity of 40-50%. Additionally, more effective anchoring of polymer chains within the tube openings will be possible which also improves mechanical properties of the clay- polymer composites. We report here an essential increase of halloysite lumen diameter by selective etching of alumina sheets within its lumen, exploiting the different chemistry of the tube's inner and outer surfaces. Recently, some important data on halloysite acid treatment was presented in [81][82]. However, these works have not presented an in depth kinetic analysis of halloysite lumen etching at varying temperatures, which is found to be especially

important for developing nanotubes with optimal loading and release properties. Reaction conditions (temperature, concentrations of acid and halloysite) are determined for the halloysite acid treatment, allowing selective etching of the tube inner part and resulting in an increase of the tube lumen diameter from 10-15 to 25-30 nm (preserving the clay tubule shape and outer diameter). This drastically enhance the tube loading efficiency (2-3 times), increasing the inner space available for encapsulation of functional chemical agents which is demonstrated with silver acetate, and anticorrosion benzotriazole loading.

3.2 Materials and Methods

3.2.1 Materials

Halloysite is obtained from Applied Minerals, Inc. as a powder and used without further treatment. Sulfuric acid, silver acetate, chromeazurol S, polyvinyl alcohol, urea, acetic acid and benzotriazole are obtained from Sigma Aldrich.

3.2.2 Characterization

The morphology of halloysite is characterized by Scanning Electron Microscope (Hitachi S 4800 FE-SEM) at 5-15 kV. Halloysite is coated with 0.5 nm gold by Cressington Sputter coater (208HR) at 20 mA for 1 min. Internal structure of the halloysite is analyzed with Transmission Electron Microscope (TEM, Zeiss EM 912) at 120 kV. UV-Vis spectrophotometer (Agilent 8453) was used to monitor aluminum concentration in the media during etching experiments. Solutions are calibrated relative to pure DI water before each experiment. An X-ray powder diffractometer (Bruker-D8 Discover, Cu-K α radiation) is used for the crystal structure analysis. Halloysite is characterized by Nicolet Nexus 470 FT-IR spectrometer using KBr pellets in the range of 600–4000 cm⁻¹. In order to improve signal to noise ratio, 32 scans are performed with the

resolution of 4.0 cm^{-1} . Samples are also characterized with 400 MHz JEOL-Delta NMR spectrometer on ^{29}Si and ^{27}Al nuclei. Poly-(dimethylsiloxane) and AlCl_3 are used as references for the silicon and aluminum. Appropriate signal to noise ratio is achieved after 16 scans. Particle size distribution is obtained by using dynamic light scattering technique (Brookhaven Instr.). Porosity analyses are performed by Nitrogen BET adsorption-desorption isotherms (NOVA-2200, Quantochrome Inst). Eppendorf 5804R centrifuge is used to separate halloysite tubes from colloidal dispersion (7000 rpm for 2 minutes).

3.2.3 Halloysite etching by sulfuric acid

1 g of halloysite is dispersed in 100 mL of sulfuric acid of 0.5 M, 1.0 M or 2.0 M. Suspension is magnetically stirred on a hot plate at the controlled temperatures between 40 and 90° C. 1 mL of aliquots are taken at certain time intervals and centrifuged to separate the halloysites. Supernatant is stored for determination of aluminum sulfate concentration. Processed halloysite is washed 5 times with DI water; pH of the supernatant from the final washing stage was in the range of 6-7, which is similar to that of pure halloysite suspension. Then the sample is dried in the oven at 50° C. The final sample represent white solid that is easily crushed into powder using mortar.

3.2.4 Determination of aluminum concentration

100 mg of Chromeazurol S is dissolved in 0.6 mL of concentrated nitric acid solution (50 %) and then 50 mL of ethanol and 20 mL of DI water are added. After that 5 ml of aqueous solution of urea (15 mg/ml) is added and solution is diluted up to 100 mL. This final solution is mixed with acetate buffer, pH 7.1, and polyvinyl alcohol in DI water (40 mg/mL). Concentration of the aluminum is determined by mixing 0.1 mL of

the prepared solution with 0.1 mL of the test solution containing Al^{+3} ions. The mixture is kept for 30 minutes and concentration was determined by UV reading at 620 nm.

3.2.5 Halloysite loading with benzotriazole

To entrap benzotriazole, 1 mL solution of 20 mg/mL benzotriazole in acetone is mixed with 10 mg of halloysite. A beaker containing this suspension is transferred to a vacuum jar, which was then evacuated using a vacuum pump. Suspension is kept in the vacuum until complete evaporation of the solvent. Then, excess benzotriazole is washed with 20% ethanol-isooctane and further dried under vacuum. Loading efficiency is calculated from the increase of the halloysite mass.

3.2.6 Halloysite loading with silver

For loading the silver 5 mg of halloysite and 10 mg of silver acetate were added into deionized water and the suspension is immersed into a vacuum for 30 minutes; loading of silver acetate is achieved by pulling and breaking vacuum three times. Then, halloysite is washed, precipitated, dried at 80° C, and heated at 300° C for 1.5 hours to decompose silver acetate into metallic silver.

3.3 Results and Discussion

Pure halloysite mineral is a white earthy dull matter as shown in Figure 3-1a, which is processed to a fine powder. Tubular structure of the halloysite with external diameters in the range of 50-70 nm is evident from Figure 3-1 b-c. The length of the tubes covers a range of 0.5 to 1.5 μm and the lumen diameter is 10-15 nm. In Figure 3-1d, one can see a periodic multilayer nature of the halloysite wall as well as views of internal aluminol (Al-OH) and external siloxane (Si-O-Si) surfaces. Periodicity in the individual layer packing is determined with X-ray analysis and is found to be

0.70 ± 0.02 nm, which corresponds to dehydrated halloysite. Elemental composition of the halloysite is as follows (atomic %): Al, 18.5; Si, 19.1; O, 62.2. Brunauer-Emmett-Teller (BET) surface area of the halloysite sample was 40 ± 2 m²·g⁻¹.

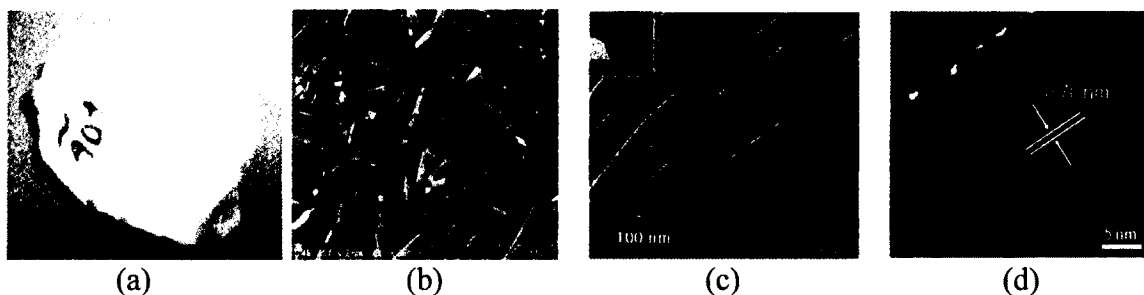


Figure 3-1: Halloysite mineral obtained from Dragon Mine Utah, Applied Mineral, Inc., USA (a); SEM of raw powder sample (b); TEM image of tubes with the cross section (inset) and HR-TEM of halloysite multilayer wall (c-d).

3.3.1 The tube lumen etching

Sulfuric acid is selected to dissolve alumina sheets from halloysite, following similar works done for kaolinite etching [33][83]. Etching starts by the diffusion of hydrogen ions into halloysite pores, followed by interaction between alumina and hydrogen ions, and diffusion of the reaction products outside the pores (Figure 3-2). Opposite phenomena (i.e. selective silica etching) can potentially be achieved using basic solutions (such as aqueous NaOH). At optimal base concentrations and reaction temperature, one may obtain porous alumina sheets or rods in this case. However, in depth analysis of this interaction is outside the scope of this paper.

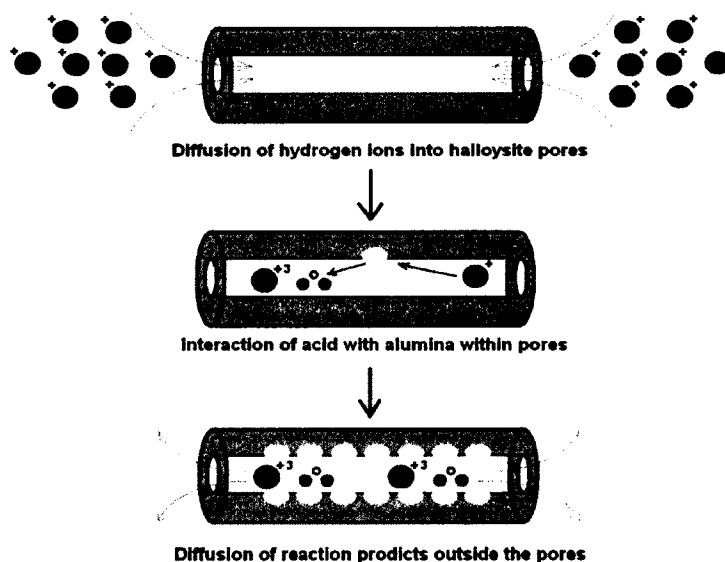


Figure 3-2: The acid etching of alumina inner layers from halloysite lumen.

Halloysite etching is optimised depending on time, temperature and concentration of the acid. In Figure 3-3 we present tube morphology, depending on percentage of removed alumina. Rodlike structures are preserved even after complete removal of the alumina from halloysites. Some small nanoparticles of ca. 20 nm diameter are visible after 50% of the alumina conversion level (Figure 3-3 c-f). These particles are amorphous SiO_2 that are leftovers from dealuminated halloysite. Silica nanoparticles are small in the initial stage of the dealumination process and, possibly, cleaned off with the supernatant upon collection of the samples by centrifugation. They gradually aggregate and become sufficiently large at 50% of the alumina etching contaminating the sample as evident from Figure 3-3d.

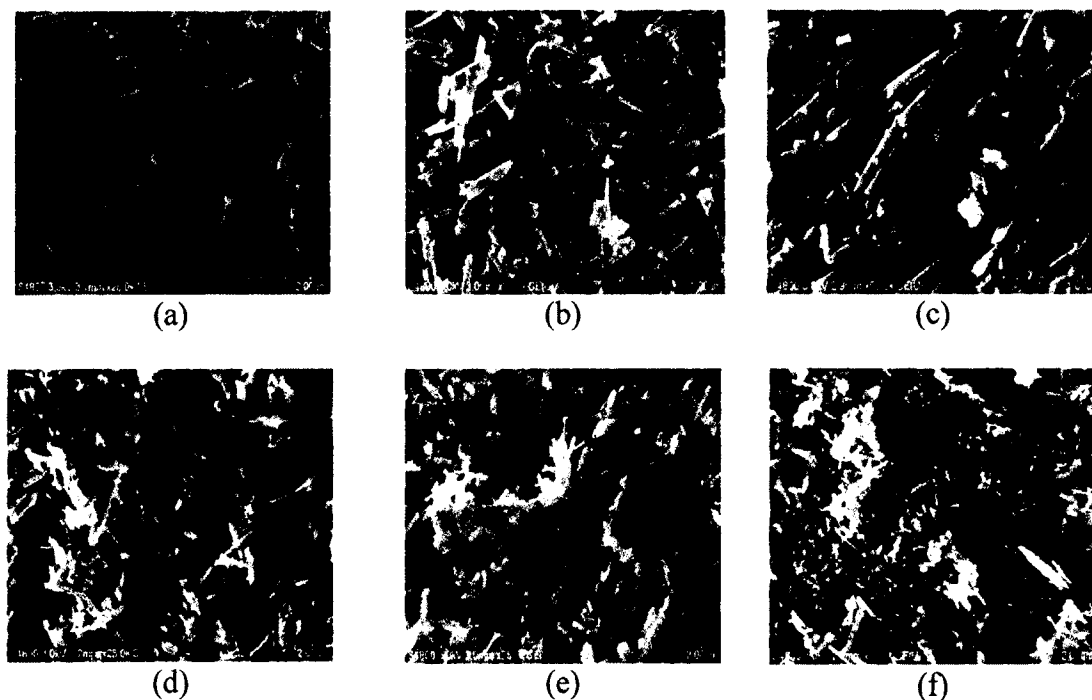


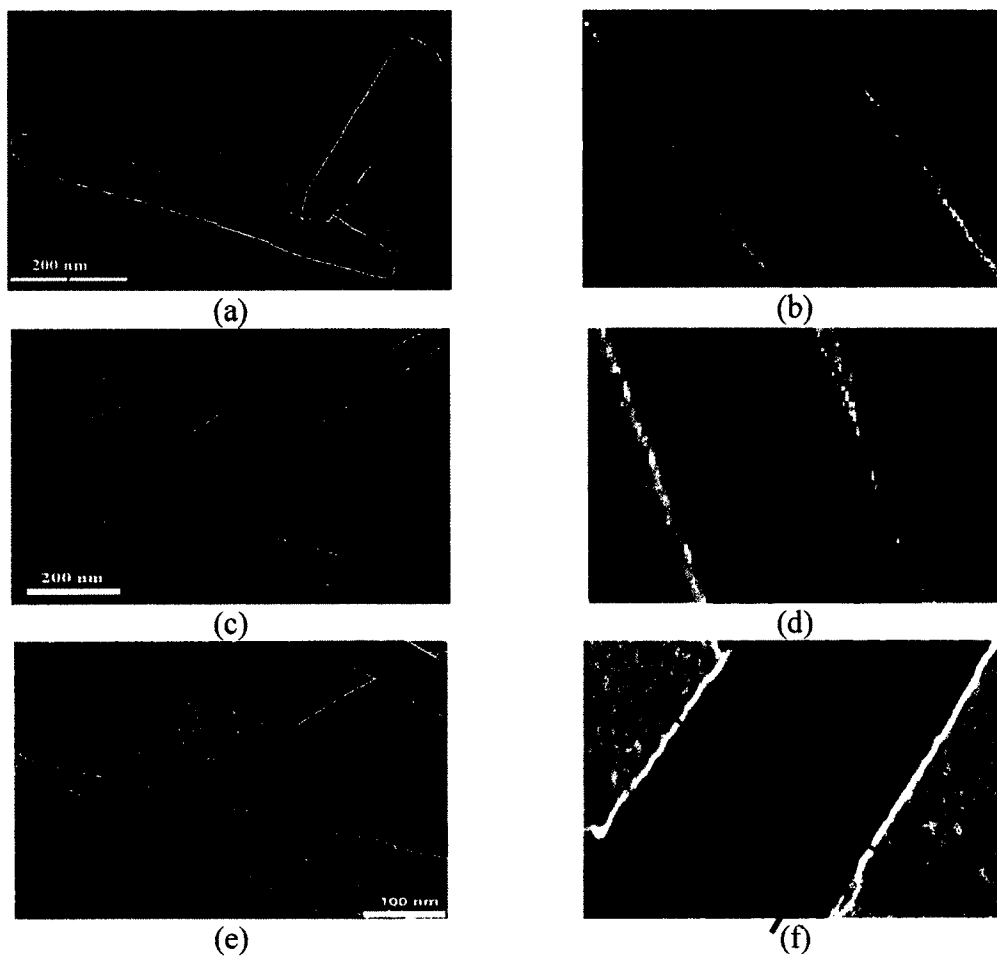
Figure 3-3: SEM images of halloysite tubes after removal of 20% (a), 40% (b), 50% (c), 75% (d), 88% (e) and 100% (f) of aluminum.

In Figure 3-4 TEM images of halloysite tubes etched at 50° C are presented.

Originally, halloysite have a lumen diameter of 10.0 ± 1.0 nm, and it increase to 21.5 ± 2.0 nm after removal of 20% aluminum and further expands to 36.3 nm upon 65% dealumination. Enlargement of the lumen size is further supported by histograms made with 200 tubes' measurements on TEM images (Figure 3-4 i, j). The external diameters of the tubes remain unchanged, indicating that etching takes place solely in the inner lumen. One can also observe left-over silica nanoparticles of 10-20 nm diameter from dealuminated halloysite walls. These nanoparticles were not observed at a lower level of alumina etching.

The tubes preserve their geometry while some holes appear on halloysite walls at the higher level of etching. Halloysite gradually loses its tubular morphology and transforms into porous nanorods upon complete removal of the alumina of the following

stages: First, uniform wall thickness is partially lost; second, the above 30-40% of the dealumination tubes with varying wall thicknesses appear; the above 50-60% of the alumina removal pores in the walls start appearing and grow with further etching. Upon complete removal of the alumina tubular morphology is lost and the lumen disappears. The final product resembles porous nanorods decorated with nanoparticles. Specific surface area of the tubes increased more than six times upon 80% of the dealumination ($\sim 250 \text{ m}^2/\text{g}$).



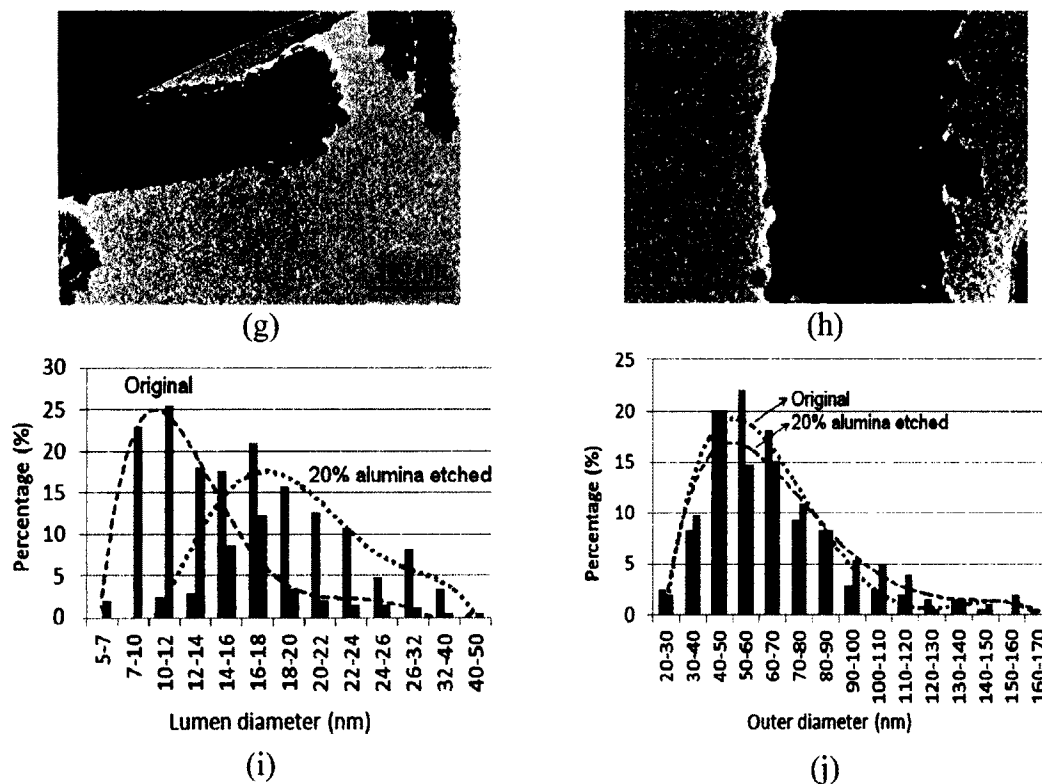


Figure 3-4: TEM images of pristine halloysite before acid treatment (a, b), after the removal of 20 % (c, d), 65 % (e, f) and 100 % (g, h) of alumina by treatment with H_2SO_4 at 50°C . External diameters of the tubes are ca. 70 nm. Lumen diameters are 9.7 nm, 21.5 nm and 36.3 ± 2 nm for original, 20 % and 65 % alumina etched halloysites. Histogram of lumen diameters (i) and external diameters (j) for original and 20 % alumina etched halloysite is also shown (based on 200 tubes' measurements).

3.3.2 Particle size distribution

Dynamic Light Scattering determines particle size distribution (effective diameter corresponding to the radius of gyration) of the halloysite at various stages of the dealumination (Figure 3-5). Particles with diameters in the range of 200 – 300 nm correspond to the individual halloysite tubes [84]. Similar observations are performed in [83] using transient light scattering and dimensions of 315 nm has been ascribed to the individual halloysite tubes. Particles with sizes larger than 400 nm correspond to the agglomerates. Fraction of non-agglomerated tubes increases upon moderate acid

treatment. Left over SiO₂ partially aggregate and form tiny nanoparticles at the initial etching stage (20-30% dealumination). These nanoparticles are separated from the mixture with centrifugation, yielding pure etched halloysite. At 55% of the conversion, silica agglomerates to the sizes of 60-100 nm which is monitored with dynamic light scattering. This is consistent with SEM observations as shown in Figure 3-4.

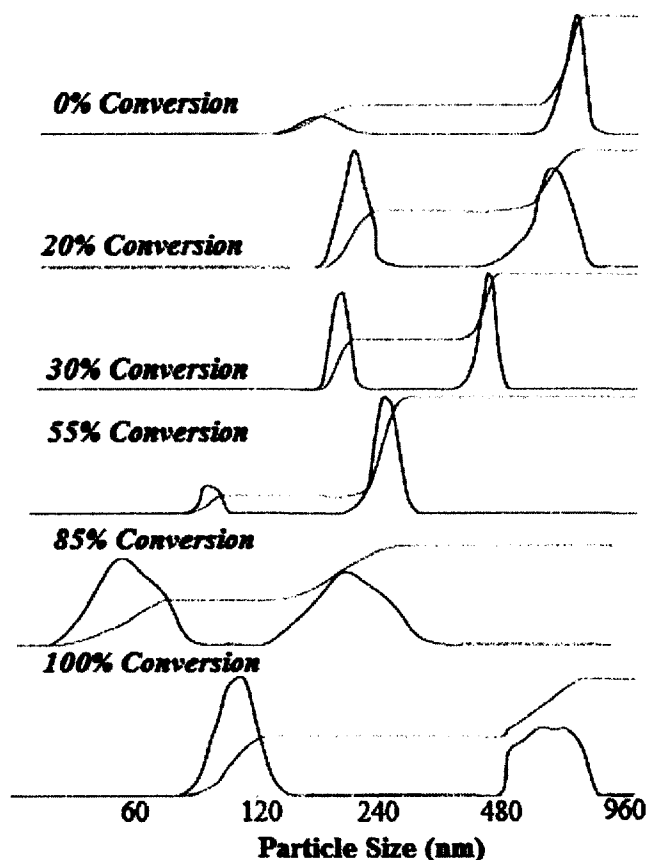


Figure 3-5: Halloysite particle size distribution at different levels of alumina etched measured by dynamic light scattering.

3.3.3 FT-IR, ²⁹Si MAS-NMR and XRD spectral characterization

Halloysite has several clearly established peaks at 600-3700 cm⁻¹ of FT-IR spectral range (Figure 3-6) [85]. Inner OH stretching vibrations of halloysite aluminol groups at 3620 and 3690 cm⁻¹ disappear upon proceeding with the reaction indicating the

removal of the alumina layers. Instead, broad peak between 3200-3700 cm^{-1} range with a maxima at 3450 cm^{-1} appear in the FT-IR spectra that corresponds to SiO-H vibrations [86], indicating the formation of silica nanoparticles. Intensity of the in plane Si-O-Si deformations at 1100 cm^{-1} also increases upon dissolution of the alumina. The signal at 754 cm^{-1} corresponding to Si-O-Al perpendicular stretching disappears and the signal corresponding to the symmetric Si-O-Si stretching slightly shifts from 795 cm^{-1} to 800 cm^{-1} . In Appendix A (Figure A-1), ratios of the the FT-IR peaks at 754 and 795-800 cm^{-1} as well as peaks at 1020 and 1100 cm^{-1} are presented. Data clearly indicates that significant changes start appearing in the spectra above 50% of the dealumination. No changes are observed at peak ratios below 40% of the alumina removal, indicating that halloysite structure is essentially unaffected. This can be explained by the removal of silica nanoparticles left over from etched halloysite sheets by the solvent upon centrifugation of the suspension (separation of solid mass from the reaction mixture). This is in agreement with SEM observations and dynamic light scattering data.

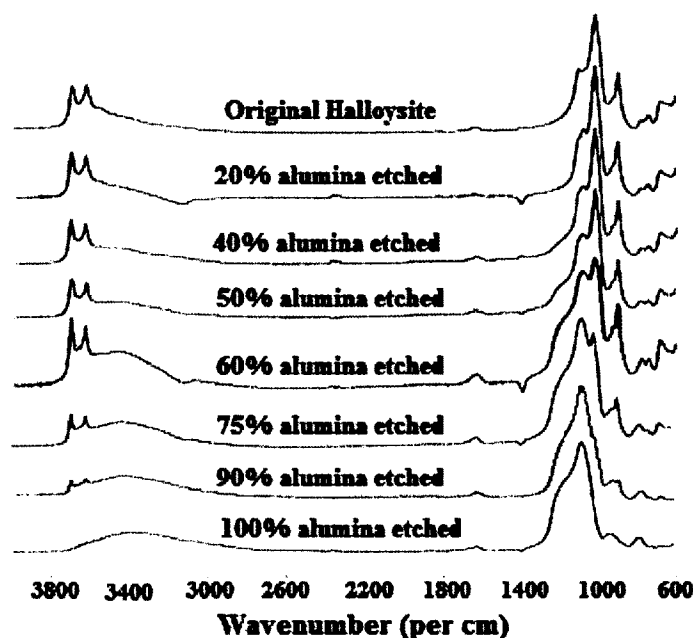


Figure 3-6: FT-IR spectra of halloysite at different levels of Al_2O_3 conversion.

In Figure 3-7, X-ray diffraction patterns of halloysite powders are shown: d_{001} peak at 7.3 \AA corresponds to the multilayer wall packing. Its relative intensity decreases above 40% of the dealumination, indicating the partial loss of the tube wall crystallinity; 4.5 \AA reflection, another characteristic of tubular halloysite [33], also start disappearing. No intercalation of sulfuric acid into the interlayer space is observed, as (001) reflection does not shift to lower angles. This indicates that etching of alumina takes place in a Layer-by-Layer fashion, i.e. etching starts from the innermost layer and proceeds towards the outermost layer (contrary to the etching of all layers at the same time, which requires intercalation of sulfuric acid between layers). The absence of silica crystal reflections indicate that most of the silica re-formed is in an amorphous state and very few as quartz microcrystals. A study on kaolinite dealumination reported similar data [87]-[90].

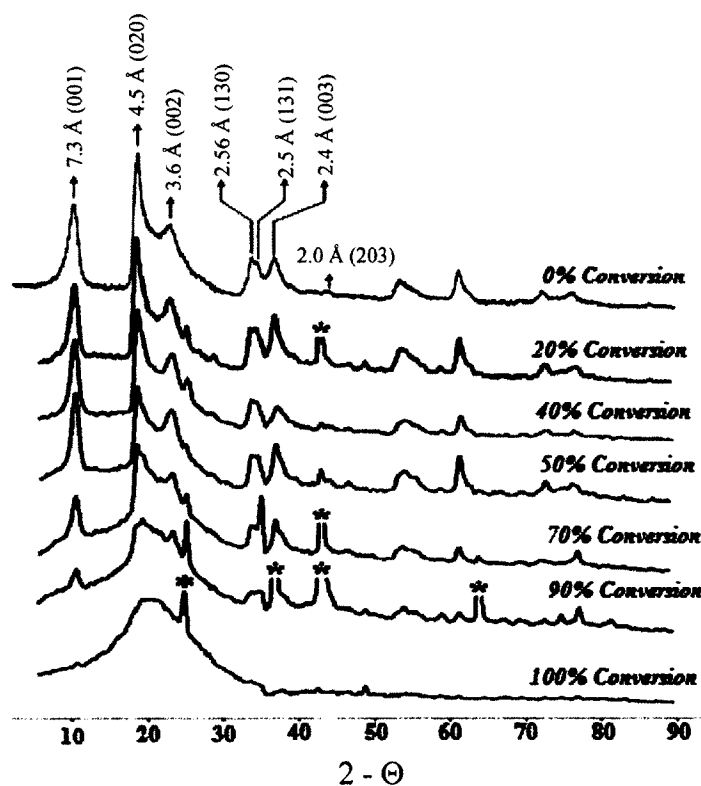


Figure 3-7 XRD spectra of halloysite at different conversion levels; * aluminum from substrate, * quartz.

^{29}Si Solid State MAS-NMR spectra of the halloysite revealed three types of silicon atoms existing in partially dealuminated samples (Figure 3-8). The sharp -91.3 ppm signal is assigned to Q^3 type $\text{Si}(\text{OSi})_3(\text{OAl}_2)$ sites, where each silicon has two second nearest-neighbor octahedral aluminums from the nearby aluminum hydroxide layer of unreacted halloysite. The broader -100 ppm (-96 to -104 ppm) peak is assigned to the newly formed Q^3 type silicon sites with one second nearest-neighbor aluminum ($\text{Si}(\text{OSi})_3(\text{O}^+\text{AlH})$) [33]. The broadest signal at -109 ppm (-100 to -118 ppm) is assigned to newly formed Q^4 -type $\text{Si}(\text{OSi})_4$ sites of amorphous silica-like regions in these dealuminated solids [87]. Al Solid State MAS-NMR spectra shows that all the alumina atoms are identical to those in original Al-OH-Al layers of halloysite (Appendix A,

Figure A2) with significant alterations observed only at a very high level of dealumination (above 90%).

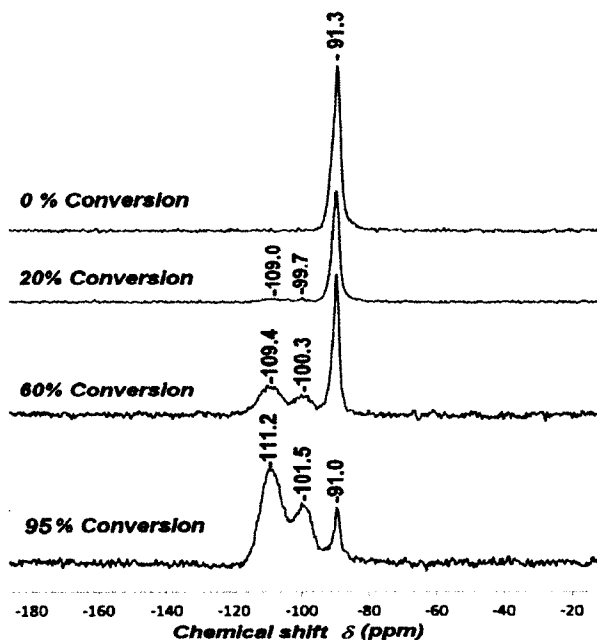


Figure 3-8: ^{29}Si MAS-NMR spectra of halloysite at different levels of alumina dissolution.

Mechanism of the halloysite layer dealumination is proposed based on NMR observations (Figure 3-9), and it suggests hydrolysis of two Si-O-Al and two Al-OH-Al bonds for the release of single Al^{+3} ions. The resulted structure has three different types of silicon atoms (labeled as Q_A^3 , Q_B^3 and Q_C^4) and a single type of aluminum. SiO-H bonds are formed as a result of alumina dissolution, which is consistent with FT-IR observations. Non-dissolved segments of the halloysite layer reserved its crystalline structure and lattice parameters as it is supported by XRD analysis.

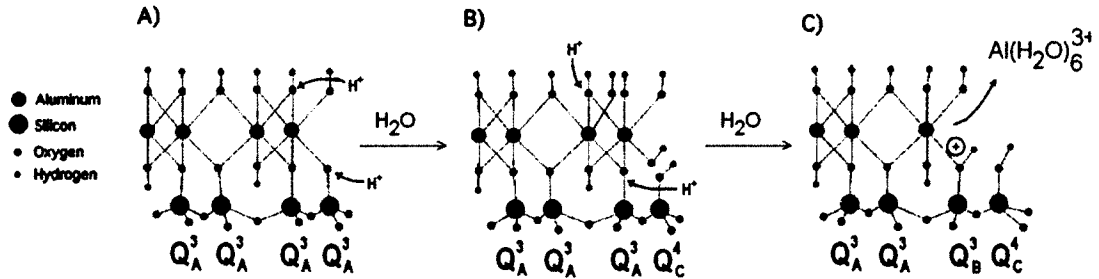


Figure 3-9: Schematic of the partially etched halloysite layer with assignments of the silicon nuclei.

3.3.4 Kinetics of alumina etching

In Figure 3-10a, the kinetics of the halloysite dealumination at various reaction temperatures are shown. Concentration of halloysite and sulfuric acid are 10 mg/mL and 1 M, respectively, which corresponds to the H_2SO_4 : Al ratio of 25:1. Linear profiles indicate that the reaction rate corresponds to the pseudo-zeroth order kinetics. The alumina etching rate becomes reasonably high above 50° C: about 5% of the alumina is dissolved by sulfuric acid at room temperature (18° C) within three days of treatment while this transformation increased to 40% at 50° C within the same time frame.

The reaction rate changes with the temperature following Arrhenius Equation (Equation 3.1), which states that certain activation energy E_A is required for the reaction to proceed:

$$v = A^* \exp\left[-\frac{E_A}{k_B T}\right], \quad (3.1)$$

where k_B is the Boltzmann's constant and A is the experimental constant. By taking logarithm at both sides, one gets Equation 3.2:

$$\ln(v) = \ln(A) - \left[\frac{E_A}{k_B T}\right], \quad (3.2)$$

In Figure 3-10b, variation of the logarithmic zeroth order reaction rate with the reciprocal of the temperature is presented. The reaction rates linearly depend on the temperature up to 70° C ($1/T = 0.0029 \text{ K}^{-1}$). This is the indication that the reaction takes place with two different regimes. An activation energy of the processes below 70° C is calculated from the slope and equal to 68.0 kJ/mole. This value is typical for the chemical reaction controlled alumina etching in clay minerals ($> 42 \text{ kJ/mole}$), while the activation energies for the diffusion-controlled processes through liquid boundary are less than 10 kJ/mole [91].

The reaction order in the alumina follows zeroth order kinetics below 70° C and two-thirds order above this temperature (Appendix A, Figure A-1). Two thirds of the reaction order is also reported on the aluminum dissolution in kaolinite [89]. In order to analyze the reaction order for hydrogen ions, dealumination is conducted by three different concentrations of the sulfuric acid: 0.5, 1.0, and 2.0 M. In Appendix A, the kinetic curves of these processes are shown along with the logarithmic curves of linear reaction rate vs sulfuric acid concentration (Appendix A, Figure A-4 and A-5). The first order reaction rate is observed for the halloysite etching at 50° C and nearly zeroth order is observed for halloysite etching at 80° C.

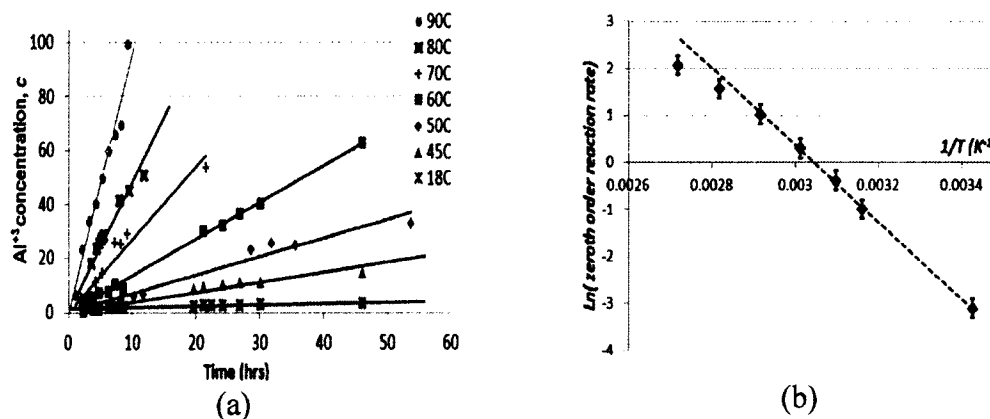
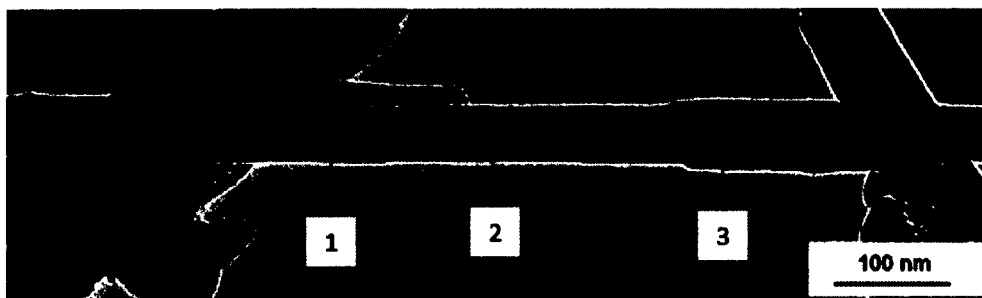


Figure 3-10: (a) Increase of Al^{3+} concentration in reaction mixture of halloysites and sulfuric acid vs temperature (aluminum concentration was normalized to maximum). (b) Variation of the logarithm of the linear reaction rate on reciprocal of the temperature.

Halloysite nanotubes with 20% dealumination at two regimes, 50° C and 80° C (below and above 70° C) are analyzed with TEM (Figure 3-11a). Tubes etched at 80° C have non-uniform lumen enlargements: wider and closer to the tube ends and narrower in the middle. The lumen diameter is ~10 nm in the middle section (arrow 2, Figure 3-11a) while it is over 20 nm close to the tube's endings (arrows 1 and 3, Figure 3-11a). This is the indication of the heterogeneous edge controlled gradient of the hydrogen ions' reactivity, and it is consistent with the data on kaolinite layer etching by hydrogen ions [92].

On the other hand, halloysite etched temperature lower than 50° C gives uniform enlargement of the lumen diameter throughout the tube's length (Figure 3-11b). In this case, a Layer-by-Layer stripping of aluminosilicate sheets takes place, thus allowing uniform etching along the lumen.



(a)



(b)

Figure 3-11: TEM images of the halloysite tubes with 20% alumina removal in two regimes: at 80° C (a) and 50° C (b).

It is reasonable to comment on the influence of acid treatment on halloysite mechanical properties as this is very important, while considering halloysite for applications in polymer composites. In the supplementary information, we give calculations of the relative changes of the halloysite bending stiffness and tensile strength at varying diameters of the inner lumen in the range of 10-40 nm. As one can expect, both the parameters reduce due to the decrease of the wall's thickness (40% decrease for bending stiffness and 62% for tensile strength). Relative change of these parameters per unit weight of the halloysite is a more reasonable data, since obtaining low weight polymer additives is equally as important as the increase in tensile properties. Bending stiffness of halloysite per unit weight has increased by 58%, while tensile strength remained unchanged. Mechanical properties of the halloysite tubes are expected to be significantly affected by formation of holes at tube walls at high levels of dealumination.

3.3.5 Enhanced encapsulation of chemicals within halloysite tubes

Halloysite tubes are proven to be effective nanocontainers for encapsulation of many biologically and chemically active substances such as proteins, drugs, antiseptics, anticorrosive, antifouling and polymer self-healing agent [21], [47], [60], [84]. A general procedure for the halloysite loading is as follows: first, halloysite is mixed with a saturated solution of the compound to be loaded. The solvent has to be not too viscous, provides high solubility of active agent, and allows stable and well dispersed halloysite colloid (e.g., water, acetone and ethanol). Once halloysite is added to the solution, the suspension is stirred and sonicated for 15-20 min. Then a beaker is transferred to a vacuum jar, which is then evacuated with a vacuum pump. Slight fizzling of the solution indicates that air is being removed from the tubule lumen. Once the vacuum is broken, an active agent enters into the pores and partially crystallizes inside the lumen. This process has to be repeated 3-4 times in order to increase the loading efficiency. With 10 nm lumen diameters ca. 10 wt% loading was typically reached, which is close to the theoretical estimations [54][55][76].

Following this procedure, silver is loaded into halloysite using aqueous silver acetate solution heated at 300° C in order to decompose it into metal. As a result, tubule lumen is filled with silver, indicating high efficiency of the tube loading, and silver (110) crystalline rod plane is oriented along the lumen (Figure 3-12). Enlargement of the halloysite lumen allows increasing the silver nanorod diameter to 25 nm. Halloysite walls in the final product can potentially be etched by alkaline solution to yield free standing nanorods with desired diameters.

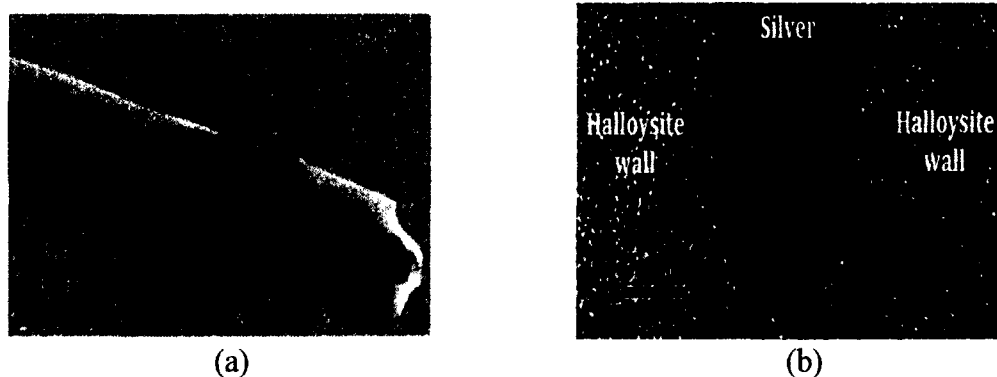


Figure 3-12: TEM images of silver nanorods within halloysite tubular templates (a) and the magnified image showing silver crystalline planes (b).

Geometrical calculations show that the volume of the tube lumen may increase 3-6 times upon removal of 50-60% of alumina, which is confirmed experimentally with loading of corrosion inhibitor benzotriazole (Figure 3-13). Halloysite loading efficiency increased four times after etching removal of ~60 % of alumina. This is associated with the increase of the halloysite's surface area and inner lumen diameter. Benzotriazole loading drops above 60% alumina etching, and this is believed to be due to the formation of multiple holes in the tube's walls at higher levels of alumina removal. Another non-desirable effect of the high (> 40%) level etching is the formation of silica nanoparticles which are significantly poorer carriers for loaded agents. Therefore, an optimal level of alumina etching is 40-60% depending on application purposes.

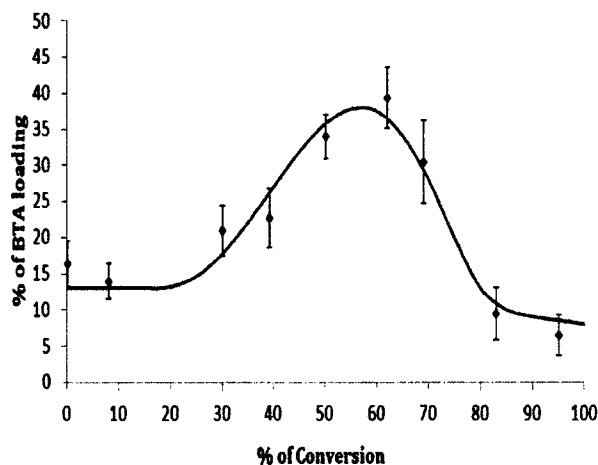


Figure 3-13: Benzotriazole (BTA) loading efficiency of halloysites treated with sulfuric acid.

3.4 Conclusion

Sulfuric acid treatment provides an efficient method for controllable enlargement of halloysite lumen diameter. Dissolution of alumina sheets starts from inner halloysite layers and, below 70° C, produces clay nanotubes with uniformly enlarged lumen diameter. Alumina removal from the nanotubes takes place in three steps: diffusion of hydrogen ions into the inner lumen, chemical reaction with alumina on the tube inner wall, and transport of the reaction products out of the lumen. Kinetics study reveal that chemical interaction is the rate determining step with the activation energy of 68.0 kJ/mole and pseudo-zeroth order below 70° C.

Above 30-40% of dealumination, significant changes in halloysite morphology are observed: manifesting holes in the halloysite walls, formation of free silica nanoparticles, and, finally, transformation of tubular halloysite into porous silica nanorods. Intensive development of holes in the tube walls at >60 % alumina etching decrease their encapsulation efficiency. Loading efficiency of benzotriazole (corrosion

inhibitor), is increased four-times with such etching technique and reach 40 wt%, which is comparable with the conventional polymeric micro-encapsulation technique.

CHAPTER 4

INTERFACIAL MODIFICATION OF CLAY NANOTUBE FOR SUSTAINED RELEASE OF CORROSION INHIBITORS

Halloysite nanotubes application as an encapsulating agent for the anticorrosive agent is well known. In this chapter, halloysite application as an encapsulating agent for anticorrosive agents such as BTA, MBT and MBI have been explored. The sections of this chapter were published: **A. Joshi**, E. Abdullayev, A. Vasiliev, O. Volkova, and Y. Lvov, “Interfacial Modification of Clay Nanotubes for the Sustained Release of Corrosion Inhibitors,” *Langmuir*, vol. 29, pp. 7439–7448, 2012. Results published in this paper are presented only in this dissertation.

4.1 Introduction

Common methods used for anticorrosion protection of metals include use of chromate based pigments; however, their use is limited because of their toxicity [15][93][94]. Polymer coatings have been developed for the corrosion protection; the coating forms a barrier against the strong corrosive species like O_2 , and H^+ . The metals are easily corroded when aggressive anionic species, such as chloride ions, which are detrimental to the metallic surface, are present [95][96]. The metals’ surface can be efficiently protected by the introduction of organic corrosion inhibitors into the coating’s

system together with a primer. Once coating is damaged, the inhibitors interact with released metal ions and form protective barrier on the surface [97].

Organic corrosion inhibitors are efficient and not harmful to the environment. However, direct addition of the inhibitor to the coatings is not efficient because of: a) interaction of inhibitor with other components of the coatings (e.g., amine inhibitors within epoxy resin), b) poor distribution of low soluble inhibitors within paint, and c) inhibitors' leaching from the coating. All of these lead to the necessity of effective micro/nano encapsulation of corrosion inhibitors before mixing with paint. These encapsulated inhibitors leak from coating defects upon formation of microcracks on the surface in a controllable fashion and heal the paint damage by forming thin films on exposed metal surface. Many different capsules have been introduced for encapsulation and controlled release of chemically active agents such as mesoporous carbon [98] or silica nanoparticles [99][100], polymer capsules [101] and polyelectrolyte nanoshells produced by Layer-by-Layer (LbL) self-assembly [102]–[104], carbon nanotubes [105], etc. However, some of these capsules are soft and often get ruptured by shear forces upon mixing with the resin (such as polymeric urea-formaldehyde or polyurethane capsules) or are excessively costly for large scale production (LbL capsules, mesoporous silica or carbon, synthetic nanotubes). Clay nanotubes are naturally available, low cost materials [1][3] with an advantage of being easily processed with many polymeric materials [53][57] (such as epoxy, polyurethane, acrylics, nylon, etc.) and provide sufficiently high loading efficiency of active agents (up to 30% by weight) [45][54] as well as possibility of controlled release through synthesis of caps at the tube's endings [21]–[23][45][55].

Halloysite is a naturally occurring alumina-silicate with biocompatible properties. It has been used as a nanocontainer for different chemical agents including corrosion inhibitors, biocides, antifouling agents and drugs [21][22][23][45], [54], [55], [60], [84],[106], [107]. Halloysite tubule containers are environmentally friendly, natural nanomaterial available in thousands of tons at a low price. We have introduced naturally abundant halloysite clay nanotubes to encapsulate triazole-based corrosion inhibitors (benzotriazole, 2-mercaptobenzimidazole and 2-mercaptobenzothiazole) and dipped these nanotubes into an acrylic coating for enhanced steel corrosion protection. Halloysite nanotubes loaded with inhibitors at 15-20 wt% are kept in dry paint layer for a long time and when a defect is formed the inhibitor is released from the tubes, therefore suppressing the corrosion. Architectural nano-cap formation at the clay tube ends through interfacial modification with copper-inhibitor complexation and urea-formaldehyde copolymer allows for tunable controlled release of the loaded corrosion inhibitors.

4.2 Materials and Methods

4.2.1 Materials

Halloysite clay nanotubes are obtained from Applied Minerals, Inc., NY. Benzotriazole (BTA), 2-mercaptobenzothiazole (MBT) and 2-mercaptobenzimidazole (MBI) were from Sigma-Aldrich, USA. We purchased oil based blue alkyd paint (PDS-33) from Krylon Co.

4.2.2 Instrumentation

Halloysite clay nanotubes are characterized using a Scanning Electron Microscope (Hitachi S4800 FE-SEM) to analyze external surface morphologies. The halloysite samples are coated with 1 nm gold by Cressington Sputter Coater (208HR)

before imaging. A Transmission Electron Microscope (TEM, Zeiss EM 912) was used at 120 kV for the imaging of internal hollow lumens. Concentration of corrosion inhibitors BTA, 2-MBT and 2-MBI are measured with UV-Vis spectrophotometer (Agilent 8453) at absorption peaks at 265 nm, 320 nm and at 300 nm, respectively. A light microscope (Olympus, Japan) with a video camera (Sony SSC DC 80) and SVET current microscanner (Applicable Electronics) are used for analysis of corrosion development on a scratched painted metal.

4.2.3 Tube loading procedure

Saturated solutions of corrosion inhibitors in acetone are mixed with a dry halloysite powder and sonicated for 15 minutes. The samples are transferred into a vacuum jar, which is then evacuated using a vacuum pump. A slight fizzing indicates removal of air from the lumens of the halloysite nanotubes, which is replaced with the saturated solution of the inhibitors. The process is repeated three times for most efficient loading. After loading, the samples are separated from the solution by centrifugation, washed with acetone and water, and then air dried.

4.2.4 Kinetics of corrosion inhibitors release

All release experiments are performed in water, at pH 6-7 and room temperature. The samples are stirred and the supernatants are collected periodically. A typical release time experiment is 15-20 hrs. Concentrations of released inhibitors are determined using UV-Vis spectrophotometer. At the end of the released study, a high power sonication is performed to ensure the complete release of loaded corrosion inhibitors and to calculate the loading efficiency.

4.2.5 Tube encapsulation with urea-formaldehyde

Corrosion inhibitor loaded halloysite samples are exposed to 0.5 ml of urea-formaldehyde pre-polymer solution for 10 minutes [3]. Then sulfuric acid is added dropwise which acts as a crosslinking agent. After 5 minutes, the sample is centrifuged and supernatant is discarded.

4.2.6 Tube end stopper formation copper ions treatment

Corrosion inhibitor loaded halloysite samples were exposed for 1 min to the bulk aqueous solution containing 0.08 M CuSO_4 . This suspension is constantly stirred with a magnetic stirrer. Then the processed nanotubes are separated from the solution by centrifugation. Halloysite loaded with corrosion inhibitors is added to the paint at 10 wt%. Paint composites with halloysite loaded with BTA and encapsulated by Cu-stoppers and UF-stoppers are also prepared.

4.2.7 Corrosion resistance testing

Loaded halloysite nanotubes are mixed at 10 wt% with the paint. The original paint and the paint with bare (unloaded) halloysite are used as a reference. A square block of paint with 5 cm x 5 cm dimensions (from each sample) are applied onto ASTM A366 mild steel (1008 alloy) strips and dried for 3 days at room temperature. Then 3% (0.5 M) NaCl salt solution is prepared. An identical artificial scratch is made at the center of the dried paint of all the samples. Then the strips are exposed to the NaCl solution for one month and corrosion development is analyzed with a light microscope. Undercoat corrosion is analyzed after careful removal of the coating from metal surface. Corrosion is further evaluated by analyzing paint adhesion to the metal surface using the balanced beam adhesion test (ASTM D5178 standard method).

4.2.8 Monitoring corrosion current

The corrosion current scanning of artificially scratched halloysite composite coating on steel in 0.1 M aqueous NaCl was performed with the SVET instrument. The Pt-blackened microelectrode is held at 0.3 mm above the sample during the scan. The vibration frequency is set to 837 Hz. The corrosion current density is detected with a resolution of 0.15 mm and scans are performed every 20 min during a 12 hour period. The current mapping is performed for the pure paint sample, paint with MBI and BTA loaded halloysite and paint with UF stopper-encapsulated halloysite.

4.3 Results and Discussion

4.3.1 Clay nanotube characterization

Halloysite is a naturally occurring tubule clay, made of layered aluminosilicate tubes with 1:1 SiO₂/Al₂O₃ ratio and is chemically similar to the kaolin [1][3]. Halloysite tubes are formed by rolling 15-20 aluminosilicate sheets with interlayer spacing of 0.72 nm. SEM and TEM image of halloysite clay nanotubes are shown in Figure 4-1. The tube internal lumen has a diameter of 10-15 nm and the external diameter is ~50 nm. The length of a halloysite nanotube ranges from 0.5 to 1.5 μm.

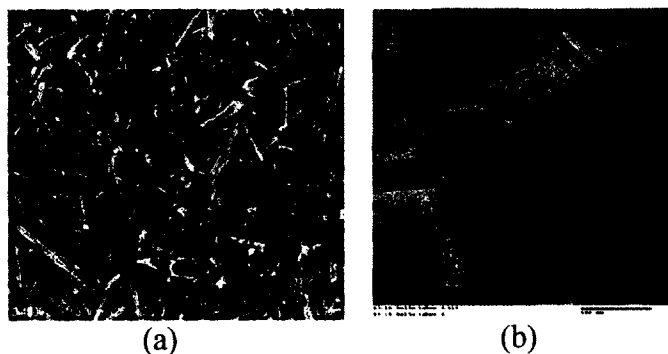


Figure 4-1: SEM (a) and TEM (b) images of halloysite.

The hollow tubular structure of the halloysite clay nanotube allows the encapsulation of corrosion inhibitors and other active chemical agents, making it useful as a nanocontainer to store and release anticorrosion agents in a sustained fashion [12], [15], [21], [22], [45], [47], [53]–[55], [60], [94]. Figure 4-2 shows formation of self-healing coatings using the corrosion inhibitor loaded halloysite clay nanotubes doped in paint. First, the halloysites are loaded with a corrosion inhibitor, dried and mixed with paint at 5-10 wt%. The paint is then applied on a metal surface. The loaded material stays inside the halloysite lumen for months until defects (cracks, scratches) occur in a paint layer, initiating the anticorrosion agents released and healing the metal surface exposed to the environment. When a paint is dissipated, the loaded material gets leaked into the corrosive media and forms a protective layer on the open metal surface through chelation with Fe(II) ions. Current work emphasizes a self-healing approach using nanotube encapsulated corrosion inhibitors.

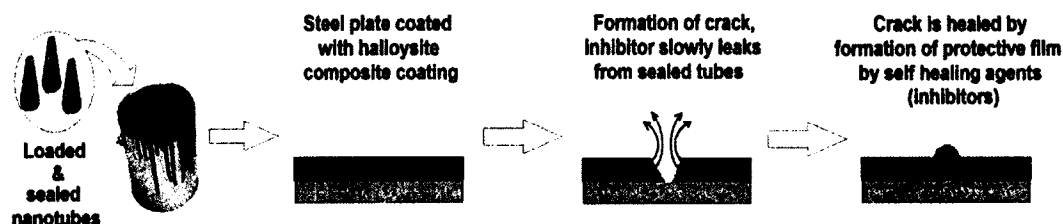


Figure 4-2: Schematic demonstration of the self-healing effect.

4.3.2 Inhibitors for corrosion protection

Benzotriazole (BTA), 2-mercaptobenzothiazole (MBT) and 2-mercaptobenzimidazole (MBI) are used as corrosion inhibitor for the protection of the metals (Figure 4-3).

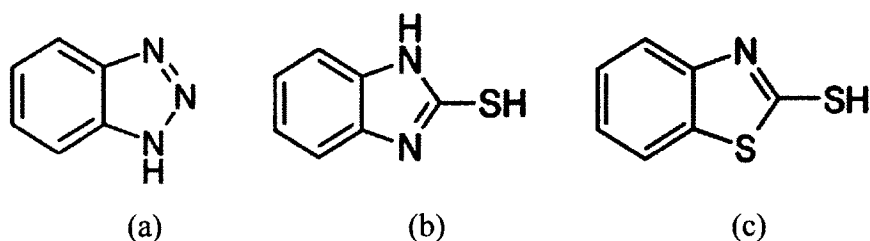


Figure 4-3: Chemical structures of benzotriazole (BTA) - a, 2-mercaptobenzimidazole (MBI) – b, and 2-mercaptobenzothiazole (MBT) – c.

These inhibitors form two dimensional protective thin films on the metal surface, which insulate the metal from the corrosive environment and mitigates corrosion. Figure 4-4 gives the comparison of inhibitive performances of these inhibitors with other common inorganic corrosion inhibitors. The tests are performed on strips made from industrial grade ASTM A366 steel. Corrosion inhibition efficiencies are evaluated by measuring metal weight loss within one week of storage of strips in 3% NaCl solutions and found to be 74%, 64%, and 41% for BTA, MBI and MBT, respectively. Sodium chromate has provided 98% anticorrosion efficiency; however, chromate inhibitors are carcinogenic, and their use has been prohibited in many industrially developed countries [45]. These results motivated us to use triazole-based corrosion inhibitors for entrapment within halloysite lumen for selfhealing coatings.

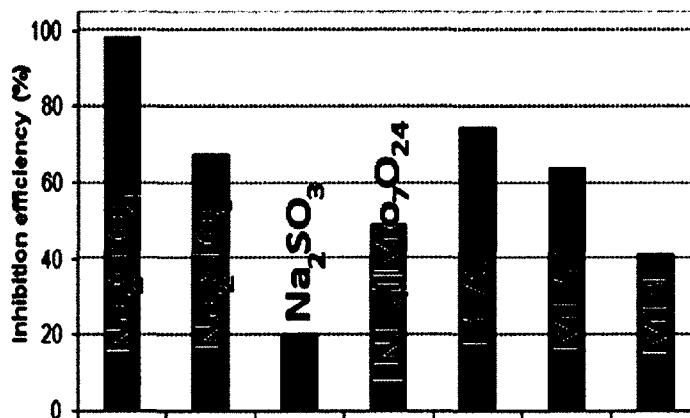


Figure 4-4: Comparison of inhibition efficiencies (%) of different corrosion inhibitors tested on ASTM A366 steel (BTA-benzotriazole, MBT—mercaptobenzothiazole, and MBI- mercaptobenzimidazole).

4.3.3 Loading halloysite with corrosion inhibitors

Halloysite tubes are loaded with corrosion inhibitors by using saturated solutions in acetone and applying vacuum suction (Figure 2-7). Vacuum suction helps to remove air bubbles within the halloysite lumen. Acetone is the optimal solvent for the inhibitors loading due to the following: 1) *Solubility*: All the corrosion inhibitors have higher solubility in acetone and therefore their saturated solutions of about 15-20 wt% can be prepared, while for water 0.5 wt% is the highest solubility. 2) *Viscosity*: Acetone has a lower viscosity than most of the other solvents and allows faster diffusion of the inhibitors into halloysite pores. 3) *Solvent evaporation*: Under vacuum solvent evaporation results in the inhibitor's concentration initiating its precipitation and solidification of the tube lumen.

In supporting information (Appendix B, Figure B-11) X-ray diffraction spectra of the halloysite samples loaded with corrosion inhibitors are presented. After loading, no changes in the 0.72 nm basal reflections of halloysite nanotubes (at $2\theta = 12.2^\circ$) are found.

It shows that the corrosion inhibitors are loaded inside in the pores mainly due to the precipitation within the lumen and no intercalation within the interlayer space took place. The BTA and MBT inhibitors loaded in halloysites are in amorphous forms, as no additional diffraction maxima were observed. In the case of MBI, a reflection at 22.5° is observed which corresponds to a 0.4 nm inter-planar distance.

4.3.4 Release of corrosion inhibitors

Release of loaded corrosion inhibitors are studied in deionized water under magnetic stirring (Figure 4-5). Comparison of the microcrystal (no encapsulation) inhibitor dissolution with the release from halloysite lumen shows that the release becomes considerably slower in the latter case allowing the anticorrosion agent to supply during 20-30 hours. Corrosion inhibitors BTA and MBT release from halloysite in two stages, while the MBI release takes place in one stage. The first stage is associated with a fast release of externally adsorbed inhibitors, while the second slow stage is the release of the inhibitor encapsulated in halloysite lumen. Such dual stage release mechanism is also reported for tetracycline release from halloysite [18, 22]. One stage exponential release of MBI shows that there is no essential amount of inhibitor adsorbed at the tube's external surface.

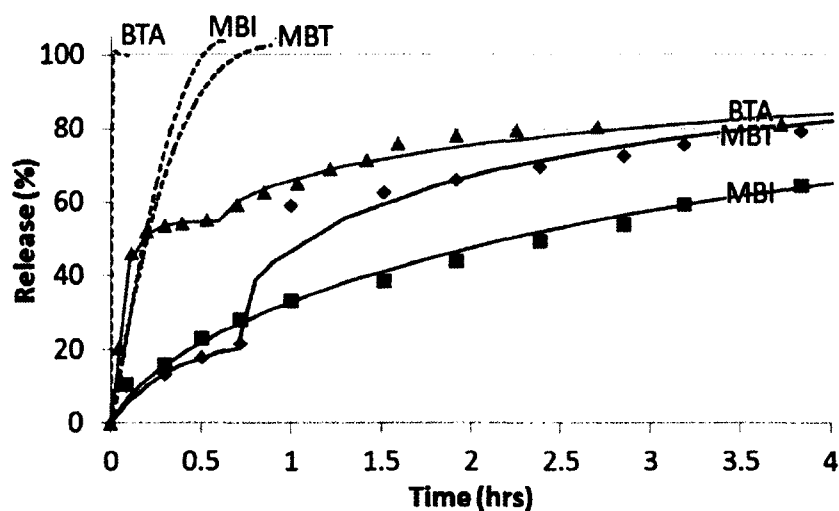


Figure 4-5: Halloysite release profiles of inhibitors: BTA-benzotriazole, MBT—mercaptobenzothiazole, and MBI- mercaptobenzimidazole (solid lines). Dissolution profiles of powder inhibitors (dashed lines) are also shown.

Corrosion inhibitor release curves were fit by Weibull's equation 4.1 [24][108]:

$$M_t = M_\infty(1 - e^{-at^\beta}), \quad (4.1)$$

where M_∞ is the cumulative amount of corrosion inhibitor released at the end of the release (in infinite time) normalized to 100, parameter α and β are experimental constants related to the specific surface area and dosage forms, and to the mass transport characteristics (Table 4-1). Weibull's model is used to calculate the amount of corrosion inhibitor released from the halloysite.

External adsorption of corrosion inhibitors is non-desirable because of the interaction of the inhibitor with other components of the paint. Besides, such release is much faster. M_∞ values of the 2nd stage release describe the amount of inhibitor stored in the halloysite's inner lumen. Closer inspection of these values indicate that encapsulation efficiency decreases in the order of MBI > MBT > BTA. All MBI is stored within halloysite lumen while only 45 wt% of the BTA is stored inside. According to the

proposed release model, 99% release of MBI is achieved within 35 hrs, which is ~ 50 times slower than the dissolution rate of the naked MBI powder. Sustained inhibitor release is desirable for efficient corrosion protection.

Table 4-1: Parameters of the Weibull's kinetic equation for the inhibitors' release from halloysite.

| Inhibitor | 1st stage of release | | | 2nd stage of release | | |
|-----------|----------------------|----------|---------|----------------------|----------|---------|
| | M_{∞} | α | β | M_{∞} | α | β |
| BTA | 55.0 | 10 | 0.8 | 45.0 | 0.5 | 0.6 |
| MBT | 23.0 | 3 | 1.0 | 77.0 | 0.7 | 0.6 |
| MBI | ---- | ---- | ---- | 100 | 0.4 | 0.7 |

4.3.5 Formation of tube end stoppers

Stoppers are effective in extending the release time of the corrosion inhibitors and drugs [21] [22][23][60]. Sustained release of corrosion inhibitors are obtained by the tube coating and partial capping of tube ends. The first approach is based on the formation of urea-formaldehyde (UF) polymer plugs at tube endings and coating on the halloysite surface (Figure 4-6a and 4-6b). Halloysite tubes are exposed to urea-formaldehyde pre-polymer solution (partially polymerized oligomer as described in [103]). Due to its abundant N-H functional groups, pre-polymer adsorbs on the halloysite's external surface via hydrogen bonding and with enhanced adsorption at the lumen ends. Rapid cross linking of the pre-polymer causes the formation of a thin polymer shell that also plugs the tube endings.

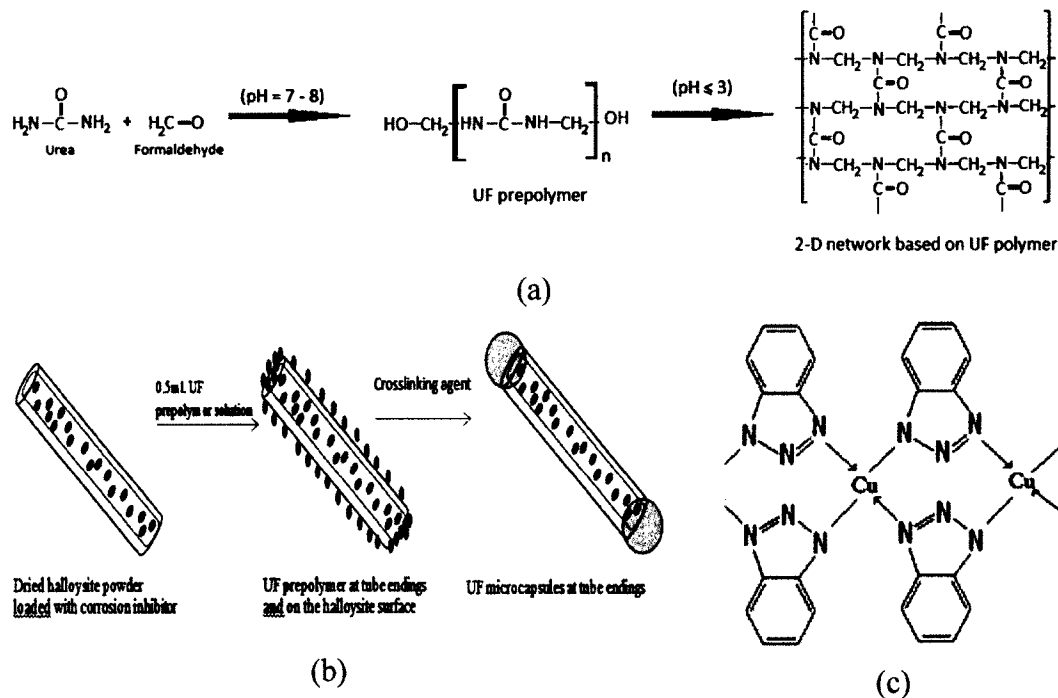


Figure 4-6: Formation of UF polymer network and stoppers formation (a-b). Copper-benzotriazole thin film coating formation (c).

In the second approach, an extending inhibitor release is based on the formation of copper-inhibitor clogs due to chelation of Cu(II) ions by released inhibitors (predominantly at the tube endings) [22]. Corrosion inhibitors form 2-D polymer films (Figure 4-c) that covers the entire halloysite surface and effectively seal tube endings and other leakage defects. Halloysites are rinsed with 0.08 M CuSO_4 solution for about 30 sec for the formation of the stoppers.

4.3.6 Evaluation of the encapsulation

Halloysite nanotubes coated with UF shell are evaluated using SEM analysis. Compared to the untreated halloysite, the surface of the UF treated halloysite is rougher (Figure 4-7a). SEM-EDX elemental analysis revealed the presence of carbon atoms on the halloysite external surface, which is an indication of the polymer coating (Figure 4-

7b). A small quantity of sulfur is also observed which might be due to the partial adsorption of sulfate ions during cross-linking of the pre-polymer. Stopper formation with copper-inhibitor interaction has been evaluated using STEM-EDX elemental mapping. The presence of nitrogen atoms on the halloysite's external surface is an indication of thin film formation from Cu(II)-Inhibitor complexation (Figure 4-7c). Oxygen mapping has been used to visualize the halloysite (Figure 4-7e). Overlapping nitrogen and oxygen maps clearly indicate thin film formation on the halloysite's external walls (Figure 4-7d).

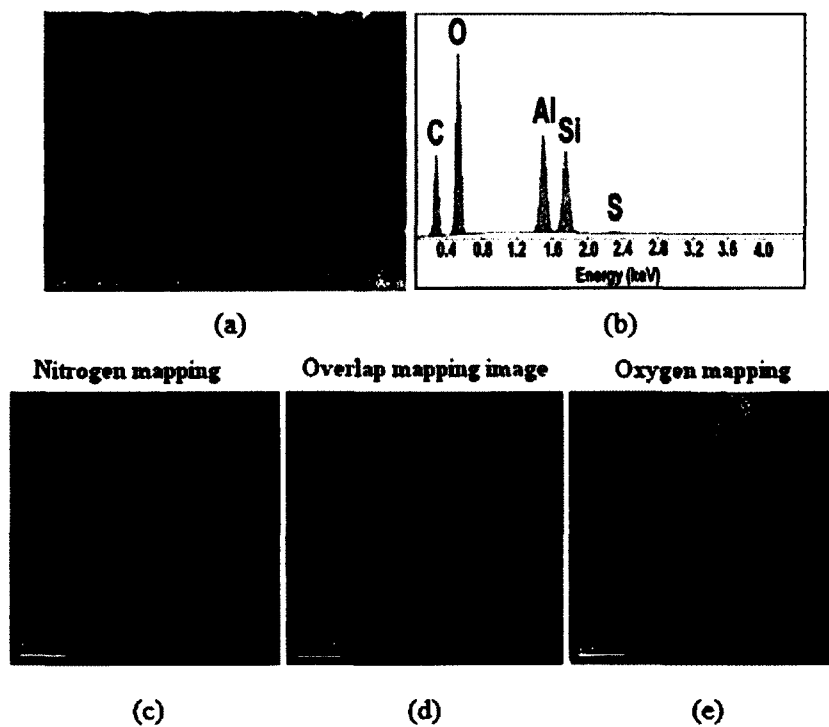


Figure 4-7: SEM image (a) and EDX spectrum (b) of UF polymer coated halloysite nanotubes. TEM visualization with elemental mapping of the shells formed on halloysite external surface with interaction of mercaptobenzothiazole-MBI with Cu (II) ions (c, d and e).

4.3.7 Controlled release profiles

Figure 4-8 shows the release profiles of corrosion inhibitors after the tube coating and end-stoppers have formed. The Cu(II)-inhibitor complexation is more efficient than the urea-formaldehyde treatment to slow down the inhibitors' release kinetics. In one hour, release of BTA is dropped from 60 to 40% for UF encapsulation and much lower for the tube encapsulation with Cu-BTA complex (~10%). Close results were observed also for MBT and MBI.

Interaction of leaking inhibitors with Cu(II) ions allow the increasing overall release time up to 200-300 hrs for BTA and MBT. MBI release rate was only 0.5% in 10 hrs while over 80% of the sample released from unmodified halloysite during that time. This is an indication that both tube encapsulation approaches work (i.e., UF copolymer and copper-inhibitor complexation); however, the second approach provides a longer release time. Tunable controlled release of corrosion inhibitors is achieved by varying the concentrations of Cu(II) ions used for the complex formation.

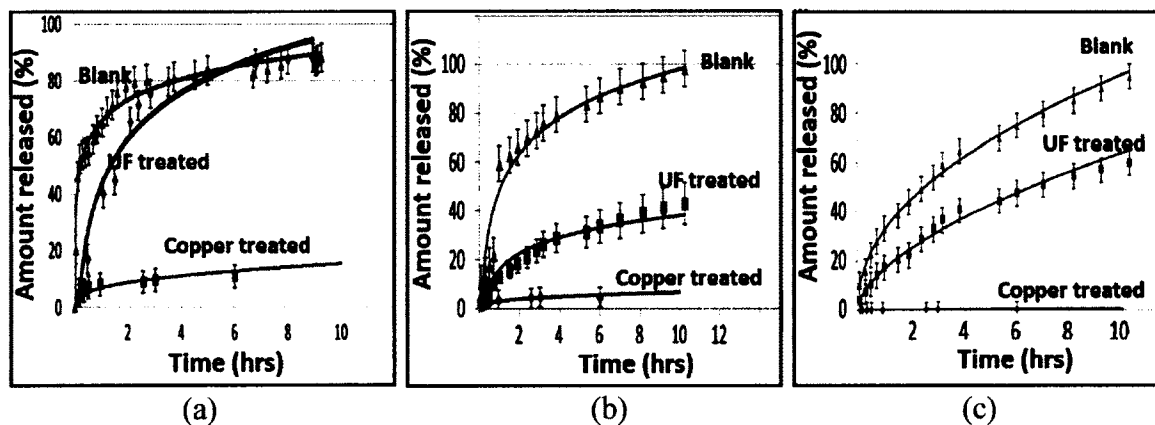
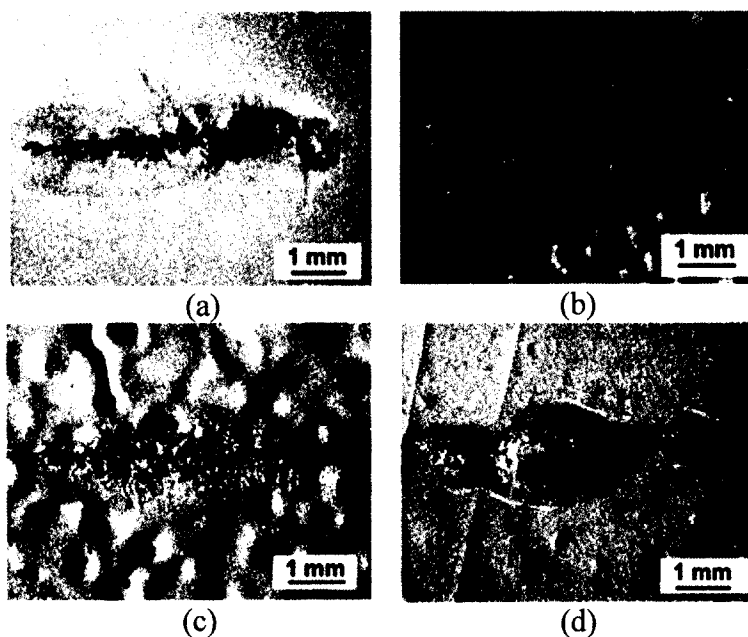


Figure 4-8: Release time reduction for benzotriazole, BTA (a), mercaptobenzothiazole, MBT (b), and mercaptobenzimidazole, MBI (c) by the additional encapsulation with urea-formaldehyde, UF and copper ions treatments.

4.3.8 Paint anticorrosion performance

Corrosion test is performed on the metal strips made of ASTM A366 mild steel. An oil based blue paint (PDS 33 powder based) is applied on metal plates. Wet paint was mixed with 5 wt% halloysite loaded with corrosion inhibitors, prior to application. One of the samples is used as a control, i.e. untreated. After complete drying of the painted metal strips, an artificial scratch is made at the center of the coating and exposed to 3% NaCl solution. After one month of exposure, all the scratched samples were analyzed by optical microscope at 50 x magnification. Sustained release of corrosion inhibitors from halloysite lumen reduces rust formation in the paint crack (Figure 4-9). Paint containing BTA loaded halloysite with UF stoppers have the least amount of corrosion products (rust) accumulated in the crack (Figure 4-9f).



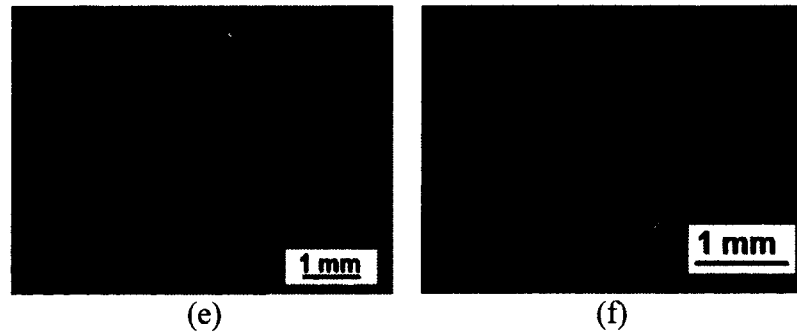


Figure 4-9: Corrosion development images of artificially scratched acrylic painted iron alloy with (a) untreated original paint, and coatings with halloysite containing (b) BTA, (c) MBT, and (d) MBI, (e) halloysite containing BTA with Cu-stoppers and (f) halloysite containing BTA with UF-stoppers.

4.3.9 Analysis of the undercoat corrosion

Paint is carefully removed from the metal surface and the interface is analyzed using an optical microscope to study the formation of steel rust under the coating. In the case of the original paint, the metal surface has many brown spots indicating the pitting undercoat corrosion process (Figure 4-10a). Some of the rust is attached to the paint and removed with it (Appendix B; Figure B-12). Metals coated with halloysite based composite coatings have lesser corrosion spots indicating corrosion inhibition in all the cases. Figure 4-10b-d refers to the painted samples containing halloysite loaded with BTA, MBT and MBI, respectively. MBI allow the least rust formation among the three corrosion inhibitors. In order to check the influence of stoppers on the corrosion rate, BTA loaded halloysite samples are encapsulated with both UF and Cu-BTA stoppers and doped into paint. Results from undercoat corrosion indicate much lesser rust formation in both cases of stopper formation compared to uncapped halloysites loaded with BTA (Figure 4-10b, e, f). UF stoppers have increased anticorrosive performance of the additives to a greater extent than the Cu-BTA stoppers.

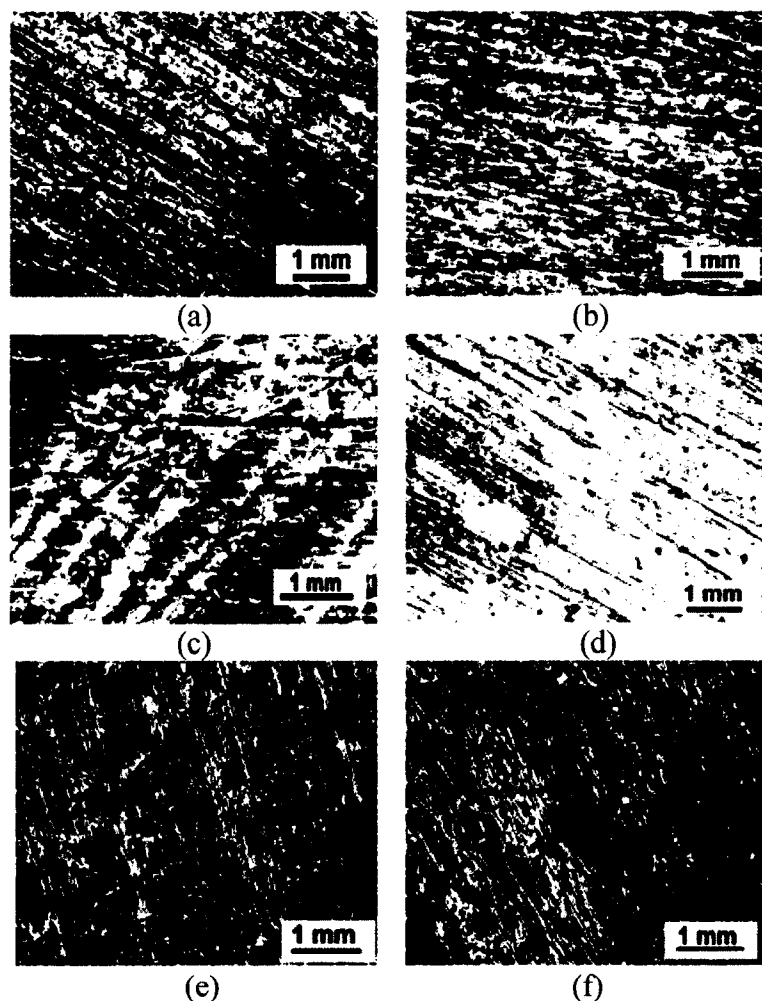


Figure 4-10: Optical microscope (50 x magnification) images of metal surface underneath the coating after one month corrosion test. (a)-control sample, paint with halloysite loaded with BTA-benzotriazole (b), MBT—mercaptobenzothiazole (c), and MBI- mercaptobenzimidazole (d); BTA loaded halloysite with Cu-stoppers (e) and BTA loaded halloysite with UF-stoppers.

4.3.10 Enhanced paint adhesion

Adhesion of paint is often used as an indication of undercoat corrosion assessment. Paint gets partially detached from the metal due to the accumulation of corrosion products at the interface. Modified balanced beam adhesion test (ASTM D5178 method) is used to determine paint adhesion [54]. Setup for measuring paint adhesion contains a beam with a movable cantilever that pushes the coating (Figure 4-11) on the

application of load to the end of the beam. Simple geometric calculations give the following formula (Equation 4.2) for the paint adhesion force:

$$F_{ADH} = \left[\frac{(P+b)L}{a} \right] \text{ctg}(\beta), \quad (4.2)$$

where P is the load applied by the tensile tester, a and L are dimensions of the apparatus, and $\text{ctg}(\beta)$ is the cotangent of the beam inclination angle (β).

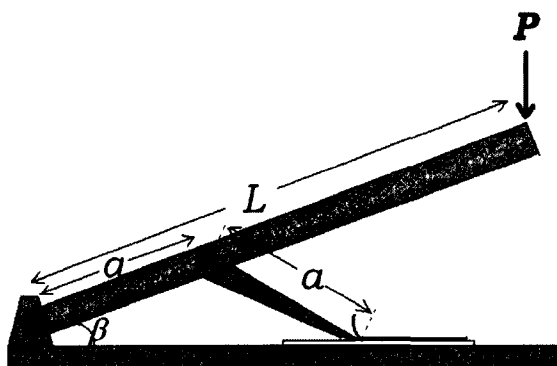


Figure 4-11: Setup for testing paint adhesive force on metal.

Paint adhesion forces are measured on the coatings after one month test in a highly corrosive 3% NaCl solution (Table 4-2). All the coatings containing halloysite have superior adhesion to the metal surface compared to the control sample. Five to ten-fold increased adhesion is observed on paint with halloysites compared with the original paint coating. Maximum adhesion is observed for coating with MBI loaded halloysites, which agrees well with the observations of undercoat corrosion testing. This is related to the retarded release of MBI from halloysite lumen (MBI showed the slowest release among all three inhibitors). Halloysites loaded with BTA and capped with UF capsules give higher adhesive strength compared to uncapped halloysites. Surprisingly, Cu-BTA stoppers are not as effective as UF copolymer stoppers.

Table 4-2: Paint adhesive forces on metal strips of ASTM A366 mild steel, after one month of exposure to the 3% NaCl solution

| Sample | Paint adhesive force (N) |
|---|-----------------------------|
| Original paint | 12 ± 8 |
| Paint with halloysite-BTA | 70 ± 30 |
| Paint with halloysite-MBT | 120 ± 70 |
| Paint with halloysite-MBI | 240 ± 50 |
| Paint with halloysite-BTA and Cu-stoppers | 80 ± 30 |
| Paint with halloysite-BTA and UF-stoppers | 180 ± 30 |

4.3.11 Corrosion current density mapping

Scanning of corrosion current density allows detecting corrosion at the initial stages, when formation of the spots is not visible. Corrosion current densities indicate the severity of the corrosion process since it has an electrochemical nature and the measured using the scanning vibrating electrode technique (SVET) on ASTM A366 mild steel. SVET uses vibrating PtIr electrode with high capacitance microtip to scan across the metal surface. The local corrosion process induces electrostatic potential gradient inside the electrolyte solution and detected by the electrode as an alternating current signal. Signals across the metal's surface are gathered to generate a 2D profile of the corrosion current density [109].

Three metal plates were coated with oil based alkyd paint, artificially scratched and exposed to 0.5 M NaCl solution. The first plate was coated with original paint (blank), while the second and third plates are coated with composite coatings containing inhibitor (MBI and BTA) loaded halloysites with open and capped tube ends, respectively (Figure 4-12). Current density measurements for artificially scratched painted steel show that blank sample has high anodic activity (Figure 4-12a, maximal current is $-15 \mu\text{A}/\text{cm}^2$). This indicates a fast pitting corrosion process taking place at the artificially introduced defect. However, Figures 4-12b and c clearly show that paints, doped with halloysites, have inhibited the development of the corrosion current. A current density map of the metal coated with the paint containing nanotubes, loaded with BTA and capped with UF copolymer plug, is even smoother than the remaining two, indicating that the corrosion is effectively diminished due to the controlled release of the loaded inhibitor.

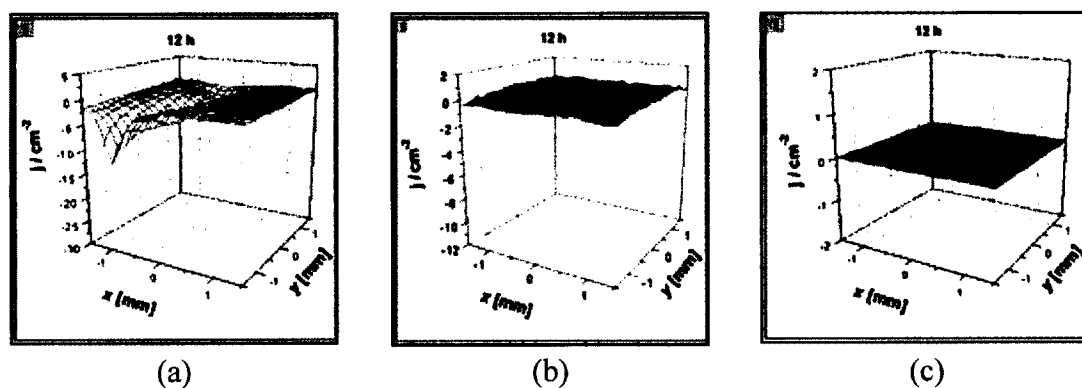


Figure 4-12: Corrosion current density maps using scanning vibrating electrode technique (SVET) of pure paint sample (a), paint with MBI loaded halloysite (b) and paint with BTA loaded halloysite encapsulated with UF stoppers. Artificially scratched and kept in highly corrosive solution of 0.5 M NaCl.

4.4 Conclusions

Natural halloysite nanotubes are employed as inexpensive containers offering essential benefits for the entrapment of corrosion inhibitors into metal coatings. The improvement using the inhibitor loaded halloysite/polymer coating is demonstrated with ASTM A366 mild steel (alloy 1008) by direct exposure of the coated metal strips to a highly corrosive sodium chloride solution. Corrosion is retarded at the initial stage due to the inhibitive action of the benzotriazole, mercaptobenzothiazole and mercaptobenzimidazole slowly released from halloysite pores in response to paint coating defects.

Minimal undercoat corrosion and best paint adhesion was obtained for mercaptobenzimidazole-halloysite embedded coatings. In depth analysis of corrosion inhibitors' release kinetics reveal that slower release of mercaptobenzimidazole (compared to other inhibitors used) is responsible for the best performance. Controlled sustainable release of corrosion inhibitors is developed through urea-formaldehyde and copper-inhibitor complex formation at the tube's ends. Copper-inhibitor complexation is more effective due to additional inhibitors sealed inside the tubes providing sustainable corrosion protection. Microscan mapping of the corrosion current on artificially scratched coating accomplished with visual observations of the developed corrosion spots show that the paint with mercaptobenzimidazole and benzotriazole loaded halloysite encapsulated with urea-formaldehyde-stoppers allow for the most significant improvement in corrosion inhibition. This approach can potentially be applied for the development of other functional coatings such as antifouling, antimicrobial, flame retardant, etc. that benefit from the encapsulation to achieve controlled release.

CHAPTER 5

USE OF INORGANIC AND POLYMERIC STOPPERS FOR THE CONTROLLED RELEASE OF DODECYLAMINE

5.1 Introduction

Chapter 4 describes that halloysite nanotubes can be used as a nanoreservoir for the anticorrosion agents such as benzotriazole, 2-mercaptobenzimidazole, and 2-mercaptobenzothiazole. Ebdullayev *et al.* showed that with the implementation of metal-organic stoppers, the release of active agents can be controlled and reduced by 20% than the controlled sample (without stoppers) [21][22][54]. Developing this approach, in this chapter dodecylamine is loaded into a pristine halloysite, a base treated halloysite and an acid treated halloysite to compare the loading efficiencies. Efficiency of the metal stoppers and organic polymeric stoppers is compared. It is observed that the polymeric stoppers are more effective in controlling the release of dodecylamine than the metal ions based stoppers. Dodecylamine loaded halloysite nanotubes' release is also analyzed in xylol, and compared with another sample having FeCl_3 as a stopper.

5.2 Materials and Methods

5.2.1 Materials

Halloysite clay nanotubes are obtained from Applied Minerals, Inc., NY. Dodecylamine for the halloysite loading, sodium hydroxide, and sulfuric acid for the

halloysite treatment are from Sigma-Aldrich, USA. O-Phtalaldehyde, and β -Mercaptoethanol for the determination of amine content in water are from Sigma-Aldrich, USA.

5.2.2 Instrumentation

Halloysite clay nanotubes are characterized using a Scanning Electron Microscope (Hitachi S4800 FE-SEM) to analyze external surface morphologies. The halloysite samples were coated with 1 nm gold by Cressington Sputter Coater (208HR) before the imaging. A Transmission Electron Microscope (TEM, Zeiss EM 912) is used at 120 kV for the imaging of internal hollow lumens. Concentration of dodecylamine is measured with UV-Vis spectrophotometer (Agilent 8453) at absorption peak 331 nm in water, and at 425 nm in xylol.

5.2.3 Halloysite loading with Dodecylamine

Loading of the halloysite nanotubes is based on the vacuum cycling of a halloysite suspension in the solution containing dodecylamine. The air bubbles located in the cores of the tubes are replaced by the solution during this process (Figure 5-1). This cycle has to be repeated by at least three times in order to get reasonable loading. Leaving the halloysite suspension overnight is observed to increase loading efficiency.

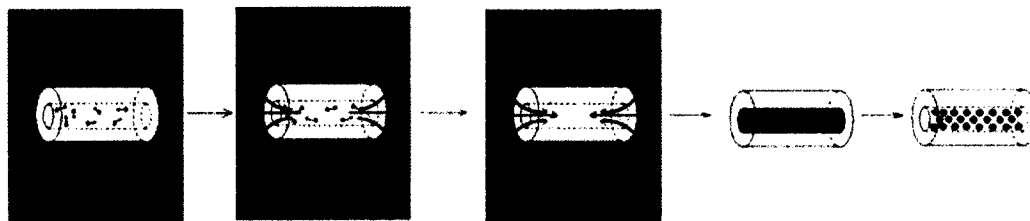


Figure 5-1: General Schematic for the halloysite loading procedure [21].

In order to load halloysite with dodecylamine 30 mg of halloysite is dispersed in 1 ml of 25% solution of dodecylamine in acetone. Suspension is sonicated for 20 minutes in an ultrasonic bath in order to better suspend halloysite nanoparticles in the solution. Suspension is left in a vacuum jar (pressure \approx 100 torr) for 20 minutes followed by breaking the vacuum and vortex halloysite suspension. The sample is left in the vacuum after the vortex and cycle are repeated 4 times for better loading of dodecylamine. After vacuum loading, sample was left overnight. Next day halloysite is separated from the solution by centrifugation and washed once with 1 ml of acetone and twice with 1 ml of water to remove amine adsorbed to the external surface of the halloysite before measuring the release rate of the amine.

5.2.4 Acid and Base treatment

The halloysite powder is treated with sulfuric acid and sodium hydroxide in order to optimize loading efficiency of the corrosion inhibitors. Halloysite was suspended in 1 M of sulfuric acid (H_2SO_4) solution and 1 M of sodium hydroxide (NaOH) solution. Concentration of halloysite is 12.5 g/L. Samples were stirred for 8 hours at 100°C on a hotplate. After treatment the halloysite is separated from the solution by centrifugation and washed with water.

5.3 Results and Discussion

5.3.1 Halloysite characterization using SEM

The halloysite nanotubes are characterized by Scanning Electron Microscope. The diameter of the tubes is about 100 nm. Tiny pieces of broken tubules and incompletely rolled tubes are also observed. The length of the tubes is highly variable. Most of the tubes are shorter than 1.5 microns. Halloysite nanotubes treated with 1 M H_2SO_4 and 1 M

NaOH are also compared with the normal halloysite nanotubes. It is observed that after the treatment with NaOH, halloysite nanotubes are found to have a spherical geometry as NaOH reacts and dissolves the external silica layer as shown in Figure 5-2a. After treatment with H₂SO₄, the tube geometry do not change but small silica nanoparticles are observed on the surface (Figure 5-2b). The TEM image clearly shows that after exposure to 1 M NaOH the halloysite nanotubes change their shapes because of silica dissolution and become spherical (Figure 5-2c). In Figure 5-2d, small silica nanoparticles are visible in the TEM of acid treated halloysite nanotubes.

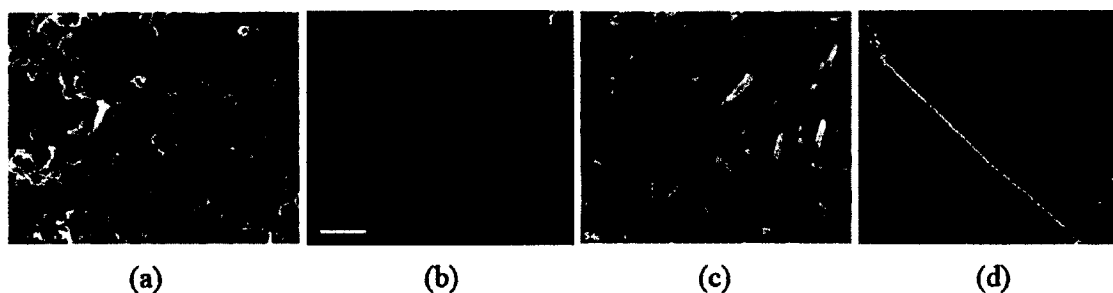


Figure 5-2: SEM and TEM images of Sodium hydroxide (a) and (b), and with sulfuric acid (c) and (d), respectively.

5.3.2 Determination of the amine concentration in water

Dodecylamine (DA) is determined in water by using UV-Vis spectrometry. Amine react with o-phthalaldehyde and β -mercaptoethanol in sodium borate buffer solution in order to detect a signal in the UV range of the spectrum; 2.5 g of o-phthalaldehyde and 3 ml of β -mercaptoethanol are dissolved in 62.5 ml of methanol and added into 560 ml 0.04 M of sodium borate solution. The final solution is allowed to sit for 24 hrs before its use. Then 0.1 ml of prepared solution is mixed with equal volumes of fresh isopropanol and dodecylamine solution in water. Concentration of dodecylamine is

determined by the intensity of the UV signal at 331 nm of the spectrum. Figure 5-3 shows the standard absorption curve for the pure dodecylamine.

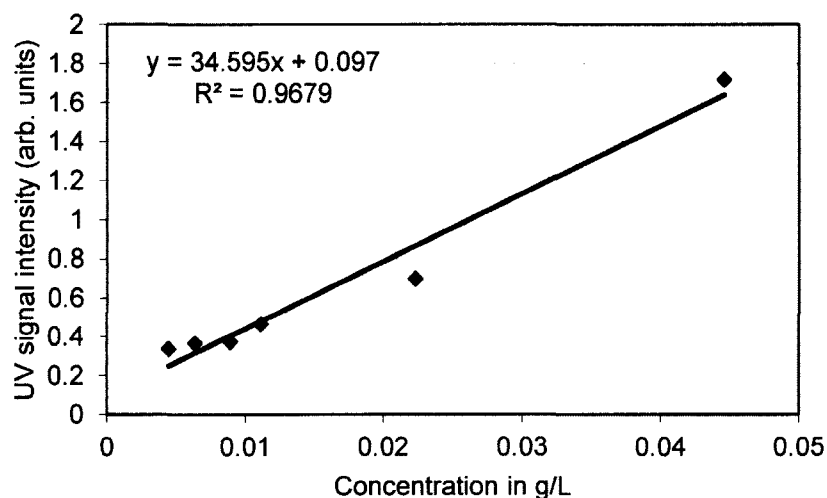


Figure 5-3: Standard curve for determination of dodecylamine concentration in water.

5.3.3 Comparison of acid and base treated halloysite samples

Release is conducted in centrifuge tubes (2 ml size). Halloysite is suspended in 1 ml of water and stirred by a magnetic stirrer. Supernatant is collected periodically by centrifugation and fresh water is added. Concentration of the dodecylamine is measured in collected supernatants and plotted versus the time to obtain release profiles (Figure 5-4). Release is performed for 11 hours. Suspension is sonicated in ultrasonic bath three times for 20 minutes in order to achieve complete release of loaded dodecylamine.

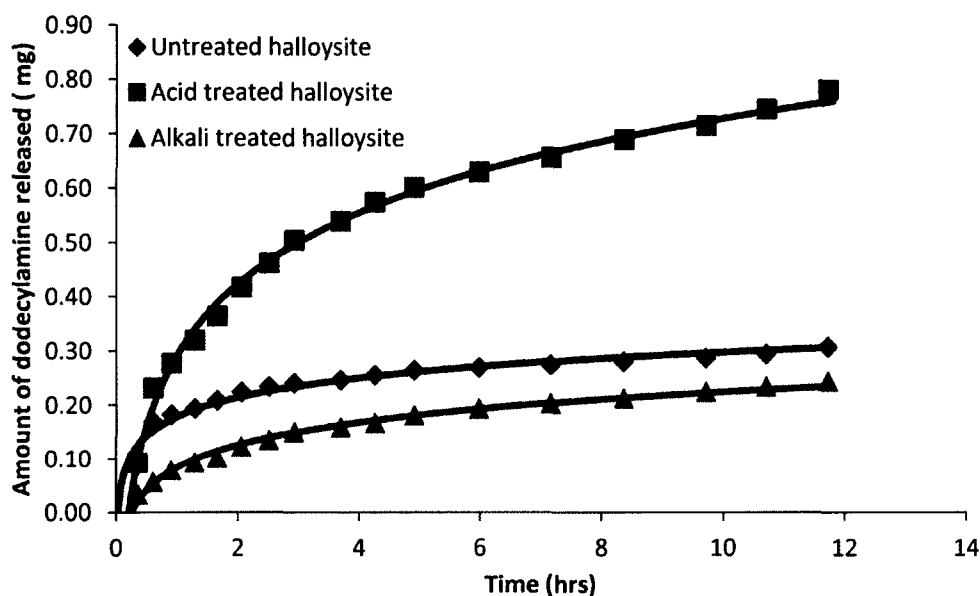


Figure 5-4: Dodecylamine release profiles from pure and modified halloysite samples.

Release profile of dodecylamine from halloysite samples is described in Figure 5-4. Loading efficiency is 3.3% by weight for unmodified halloysite. Acid and base treated halloysite samples show 4.5% and 2.2% of loading efficiencies, respectively. Acid treatment caused a 50% increase in loading efficiency. These results are in agreement with the results in Chapter 3 with the release of benzotriazole [45]. For the acid treated halloysite, the loading efficiency is more than the controlled halloysite sample. In the case of base treated halloysite, the loading efficiency is less than the controlled sample. The observed release profile for the base treated halloysite could be from the dodecylamine deposited on the surface of the halloysite. After treatment with the base, the halloysite nanotubes become spherical as shown in Figure 5-2b. Therefore, for further experiments, controlled halloysite nanotubes and acid treated halloysites are considered.

5.3.4 Formation of stoppers at tube endings

Abdullayev *et al.* showed that with the implementation of metal-organic stoppers the release of active agents from the halloysite nanotubes can be extended with controlled release (Figure 5-5a) [21], [22], [54]. Joshi *et al.* implemented the similar principle in controlling the release of anti-corrosive agents with the formation of metal-organic stoppers and urea-formaldehyde stoppers [46]. Controllable release of dodecylamine from halloysite nanotubes are achieved by the formation of stoppers at halloysite tube endings by interaction of leaking dodecylamine and metal ions from the bulk solution. The idea is very simple and requires only the washing of loaded halloysite nanotubes with solution containing metal ions (Figure 5-6). In this experiment, two different types of stoppers are compared. The first type of stopper is a metal ion stopper and organic polymeric stoppers.

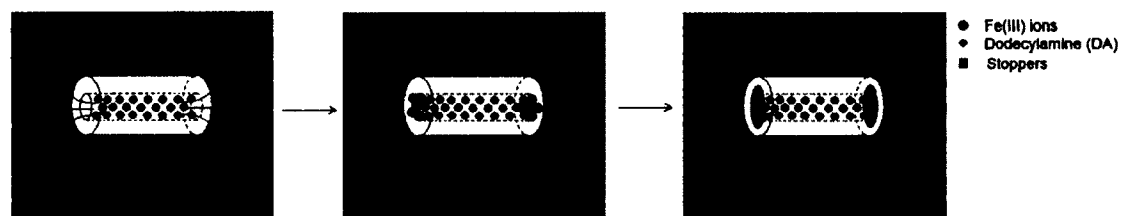


Figure 5-5: Illustration of stopper formation at halloysite tube endings by interaction of leaking dodecylamine [21], [22], [46], [54].

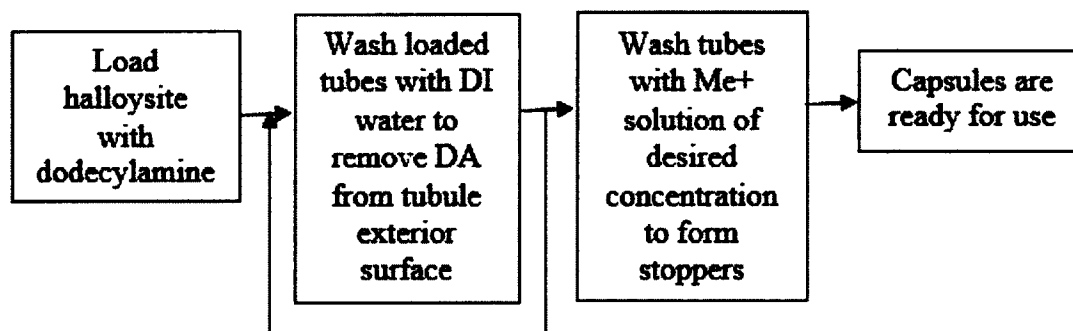


Figure 5-6: General Scheme for encapsulation of dodecylamine.

For the formation of Fe(III) stoppers at the end of the tubes, a 5 mL of $\text{FeCl}_3 \cdot 6\text{H}_2\text{O}$ salt solution is prepared with a concentration of 24 mg/mL. Dodecylamine loaded halloysites are washed two times with acetone. Then the halloysites are suspended in 2 mL of stopper solution for 10 minutes. Samples are centrifuged and the supernatant is removed. Stoppers are also synthesized by using metal ions such as Cu(I), Cu(II), Fe(II) ions, and organic stoppers such as glutaraldehyde and sodiumtripolyphosphate. The following stopper solutions were used in these cases:

For Cu(I) stoppers: 8.0 mg/ml solution of CuCl in water

For Cu(II) stoppers: 20 mg/ml solution of $\text{CuSO}_4 \cdot 5\text{H}_2\text{O}$ in water

For Fe(II) stoppers: 15.9 mg/ml solution of $\text{FeCl}_2 \cdot 4\text{H}_2\text{O}$ in water

For glutaraldehyde stoppers: 8.0 mg/ml solution of glutaraldehyde in water

For tripolyphosphate stoppers: 29.5 mg/ml solution of $\text{Na}_5\text{P}_3\text{O}_{10}$ in water.

After the formation of stoppers, release study is performed in water for ~27 hrs.

The observed release profile is shown in Figure 5-7. It is observed that in the case of both the samples Fe(III) stoppers are effective than the Cu(II) stoppers. For the acid treated samples, dodecylamine loading efficiency is higher than the controlled sample. In the

case of bare halloysite, Fe(III) stoppers work better than for the acid treated halloysite. The reason could be the enlarged lumen size, because the lumen did not get covered with the stoppers entirely. However, the stoppers' effectiveness is evident. As the acid treated halloysites showed a promising release profile even with the stoppers for the next set of experiment, the same halloysites were used to check the efficiency of organic/polymer based and other metal based stoppers.

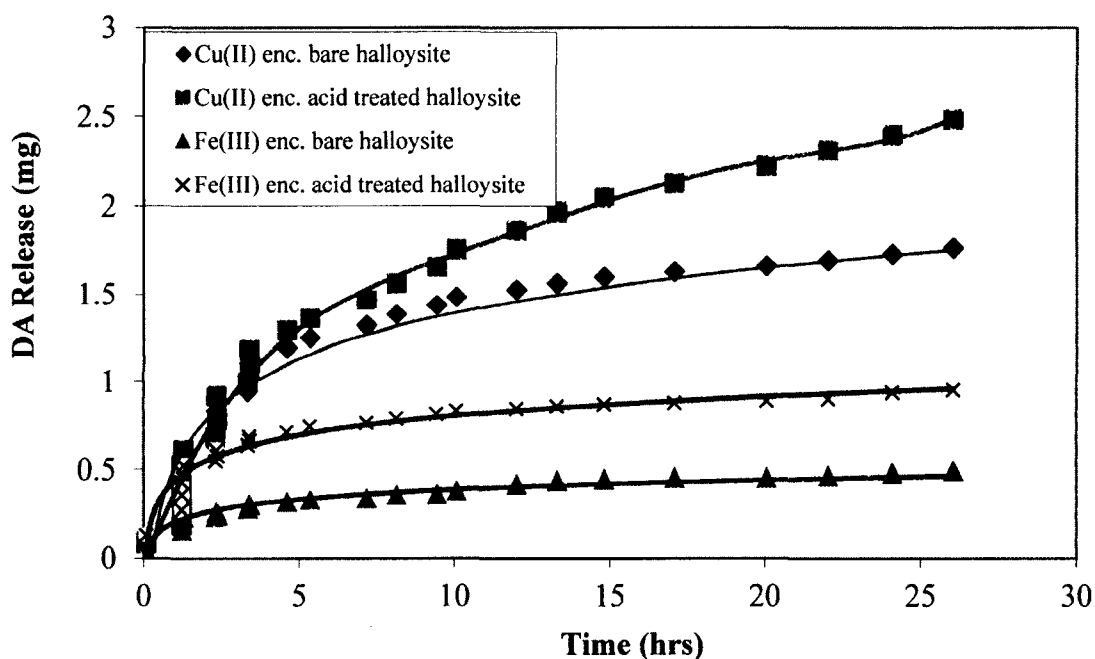


Figure 5-7: Dodecylamine (DA) release profiles from Acid treated and bare halloysite samples with Copper and Iron based stoppers.

In Figure 5-8 dodecylamine release profiles from halloysite samples treated with Cu(I), Fe(II), glutaraldehyde and sodiumtripolyphosphate stopper solutions are shown. The best stoppers are observed in the case of sodiumtripolyphosphate treatment. Most of the halloysite samples have rapid initial release within 2 hrs. However, in the case of sodiumtripolyphosphate based stoppers, we do not observe a rapid release in the first

stage. This could be because of formation of a polymeric network of tripolyphosphate at the tube ends, and on the halloysite nanotubes' surface as well. This can be used for stopping dodecylamine leakage from halloysite in the water. Therefore, for the analysis of dodecylamine release in xylol, the halloysites are covered with glutaraldehyde, sodiumtripolyphosphate, and Fe(III) stoppers.

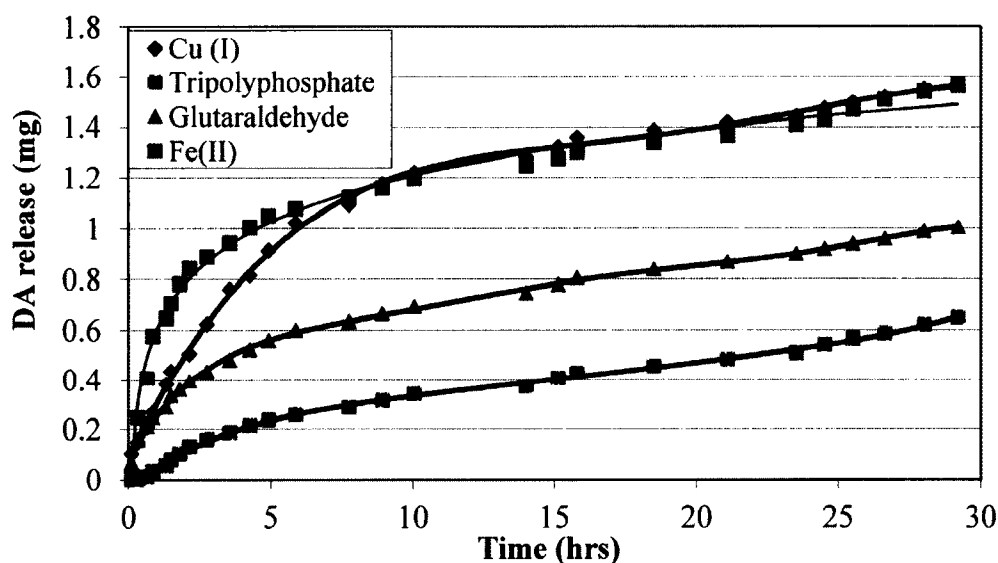


Figure 5-8: Dodecylamine (DA) release profiles from Acid treated halloysite samples with Cu(I), Fe(II), glutaraldehyde and sodiumtripolyphosphate based stoppers..

5.3.5 Determination of amine in xylol

Dodecylamine is determined in xylol using UV-Vis spectrometry. For the detection of the amine in xylol, the reaction of dodecylamine with salicylaldehyde is used. The reaction is based on the determination of primary amine which gives Schiff's base. Primary amine reacts with an aldehyde, and gives imine as a product which is often referred to as Schiff's base, and the concentration of imine is determined using UV-Vis spectrometry (Figure 5-9) [110].

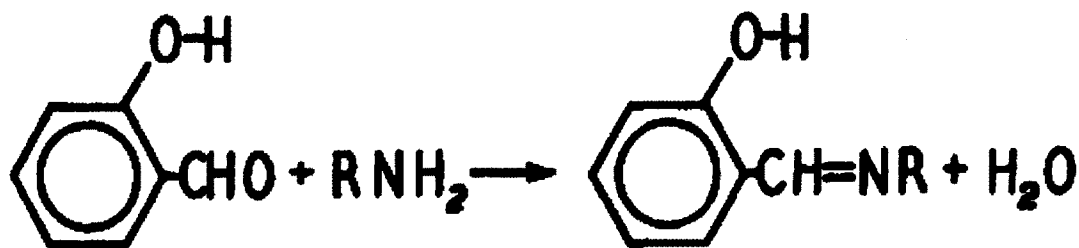


Figure 5-9: Reaction of primary amine with aldehyde to determine the concentration of Schiff's base [110].

This reaction takes place in an acidic environment. A 0.1 ml of dodecylamine solution in xylol is mixed with solutions containing 0.02 mg/ml acetic acid in xylol and 0.05 mg/ml salicylaldehyde in xylol of equal volume. The mixture is sit for the complete reaction for 24 hrs. Concentration of dodecylamine is determined by the intensity of the UV signal at 425 nm of the spectrum. A standard curve is plotted by using 0.1 mg/mL, 0.2 mg/mL, 0.3 mg/mL, 0.5 mg/mL, and 1 mg/mL solution of dodecylamine. UV signal linearly increases with the increase of concentration, suggesting that the method is valid for the determination of DA in xylol (Figure 5-10).

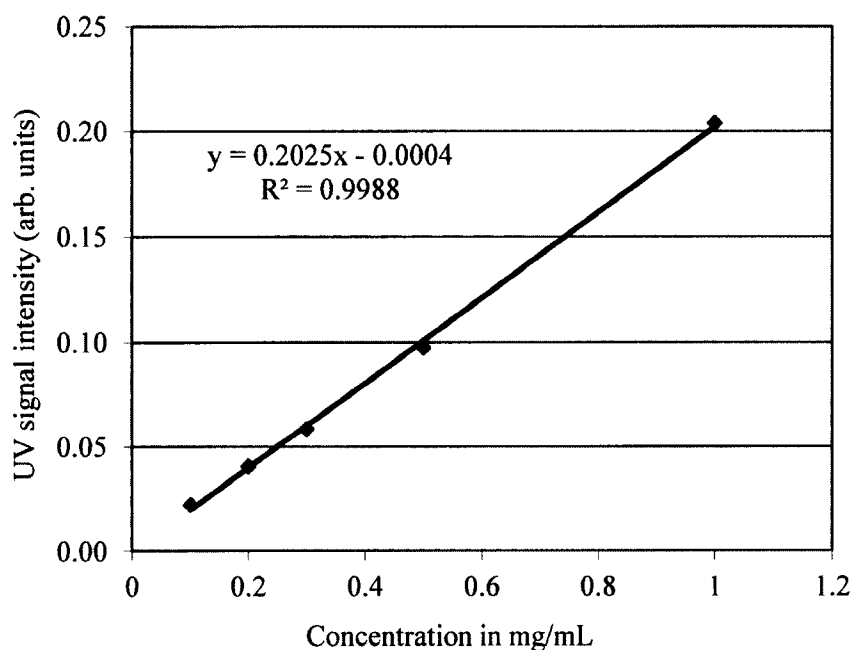


Figure 5-10: Standard curve for determination of dodecylamine concentration in xylol.

5.3.6 Observation of dodecylamine leakage in xylol

In this experiment, we consider real technological conditions in which large quantities of halloysite will be used as an additive in paint. Therefore, we increase the scale of our experiment as much as we can in lab conditions. We use 4 g of dodecylamine loaded halloysite instead of 30 mg as we did in the previous cases. Halloysite is dispersed in 80 ml of xylol. Concentration of the halloysite in the final solution is ~ 5% by weight, which we consider an optimal concentration for metal corrosion protection. Suspension is mixed with laboratory mixer (Cole palmer) of 30 mm diameter blade for 10 minutes and kept for 2 days. After two days the samples from the suspension are taken and analyzed for possible dodecylamine leakage.

As one can see from the UV spectrum of the samples collected from xylol suspension of the halloysite, significant amounts of dodecylamine is observed in the

suspensions with halloysite samples treated with sodiumtripolyphosphate and glutaraldehyde (Figure 5-11). No leakage of dodecylamine is detected from halloysite treated with FeCl_3 . Therefore, we recommend using FeCl_3 for the stopper formation in order to avoid dodecylamine leakage from halloysite in xylol.

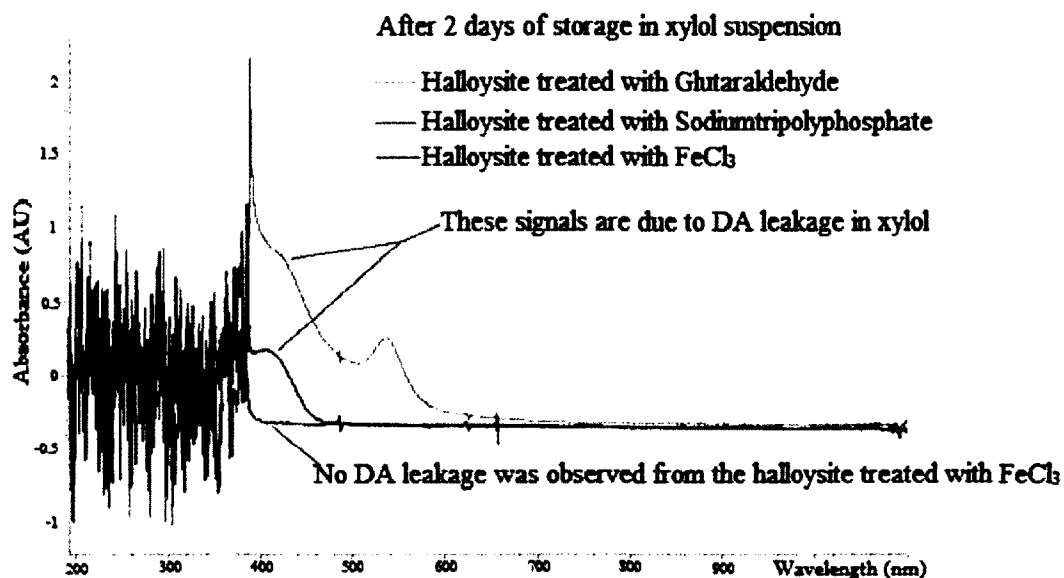


Figure 5-11: UV spectrum of the samples collected from xylol suspension of the halloysite. (Big noise below 380 nm is due to the signals from salicylaldehyde and xylol. Salicylaldehyde was added to solutions before analyzing samples with UV).

5.4 Conclusion

Dodecylamine is loaded into a pristine halloysite, NaOH treated halloysite and H_2SO_4 treated halloysite. Acid treated halloysite are found to have higher dodecylamine loading efficiency than pristine and base treated halloysites, which proves the previous claim. TEM images show that after treatment with base halloysite based spherical shape, and therefore they are opted from further experiments. In the case of stoppers, Fe(III) metal ion based is found to be effective than the Cu(II) metal, for both, bare halloysite

and acid treated halloysite samples loaded with dodecylamine. For the controlled release of dodecylamine, one more set of stoppers is analyzed: Cu(I), Fe(II), glutaraldehyde, and sodiumtripolyphosphate stoppers. Sodiumtripolyphosphate stopper is more effective than the other agents. Dodecylamine release study is analyzed in a paint thinner, xylol.

Concentration of Dodecylamine in xylol is determined based on the formation of Schiff's base product. It is observed that dodecylamine loaded halloysite with Fe(III) stoppers have more controlled release than the glutaraldehyde and sodiumtripolyphosphate stoppers.

CHAPTER 6

FLAME RETARDANT COATING DOPED WITH HALLOYSITE CLAY NANOTUBES FOR FLAKE BOARD PROTECTION

In this chapter, we extend the concept of clay nanotube dopant for flame-retardant nanocomposites. Similarly to anticorrosion agents, we load the clay nanotube with standard anti-burning chemical agents for a protective coating. Halloysite itself has flame-retardant properties, which may be synergistically enhanced with its loading with phosphate esters (e.g., triphenyl phosphate). A paper on this research is in preparation.

6.1 Introduction

Fire is one of the leading causes of casualty in the world, with more than 3000 deaths and property damage of \$11 billion in United States alone [111]. Fire retarding agents are effective in reducing these numbers each year. However, not all the fire retarding agents are useful from an environmental point of view. The main function of a flame retardant is to slow down or completely extinguish the ignition or the flame of that material [112]. The important criteria for a flame retardant functionality is to decrease the rate of combustion by reducing the rate of formation of harmful substances such as carbon monoxide. Flame retardants are commonly divided into the following groups [112]:

1. Organic based halogenated flame retardants such as chlorine, and bromine, in combination with oxide of antimony.
2. Phosphorous based flame retardants such as phosphate esters.
3. Aluminum and magnesium based flame retardants such as aluminum trihydrate ($\text{Al}_2\text{O}_3 \cdot 3\text{H}_2\text{O}$), and magnesium hydroxide, $\text{Mg}(\text{OH})_2$. Sb_2O_3 is the most efficient but very expensive flame-retardant additive to the paint.

The objective of the flame retardant is to reduce the formation of highly active radicals such as $-\text{OH}$, $-\text{H}$ which are commonly formed when a polymer burns. They react with each other in gaseous state as the reaction is predominantly endothermic, and release the energy back into the flame [112]. Flame retardants contain heavy atoms, such as halogen, which absorb the released energy from the flame and prevent further combustion of the flame.

According to the Environmental Protection Agency (EPA), some of the brominated based flame retardants are harmful to the marine life as well as to people if the concentration is more than the optimum level. It is observed that higher concentration ($>5 \text{ g/Kg}$) of a flame retardant Tetrabromobisphenol A (TBBPA) could lead to thyroid related problems [111]. Therefore, certain criteria should be taken into consideration before choosing a flame retardant. Flame retardant should be selected carefully and it should not react with other components of the paint/polymer [112]. It should be inexpensive, colorless, and stable at normal temperature, and upon exposure to light it should not change its nature, and most importantly, a flame retardant should not alter the

properties of the final product. Phosphate based flame retardant is as effective as halogen-free alternatives for different polymers and other applications [113].

Halloysite is a naturally occurring clay mineral, and is found to have flame retardant properties when admixed with polymers [56], [58], [69]. In this case study, halloysite nanotubes are tested as a flame retardant after mixing with latex paint. Latex paint is mixed with 5 wt%, and 7 wt% halloysite and paint with 5 wt% of FR-1 commercial flame retardant using a mechanical mixer, and applied on a wooden flake board. The samples are tested for flame retardancy using a handheld Benzomatic™ propane flame torch. The extended part of this study include loading of triphenyl phosphate (TPP) flame retardant agent into the halloysite, and checking its loading efficiency using thermogravimetric analysis (TGA). All the samples are tested according to the ASTM E84 standard which takes different criteria into consideration to check the flame retardant properties of the paint such as flame spread, point of self-extinguish, and smoke development.

6.2 Materials and Methods

6.2.1 Materials

Halloysite nanotubes are acquired from Applied Minerals, Inc., New York, USA. Latex paint and 10 cm x 10 cm wooden flake board and FR-1 commercial flame retardant are supplied by StormWall Industries in Ruston, LA. Phosphorous based flame retardant triphenyl phosphate is supplied by Sigma-Aldrich, USA.

6.2.2 Instrumentation

Halloysite clay nanotubes are characterized using a Scanning Electron Microscope (Hitachi S4800 FE-SEM) to analyze the external surface morphologies. The halloysite samples are coated with 1 nm gold by Cressington Sputter Coater (208HR) before the imaging. A Transmission Electron Microscope (TEM, Zeiss EM 912) is used at 120 kV for the imaging of internal hollow lumens. For the flame testing, the samples are burned with a handheld Benzomatic™ torch. Images of the samples before and after the testing are taken with a Panasonic Lumix DMC-FZ35 camera. Loading efficiency of triphenyl phosphate into halloysite was determined by using Thermogravimetric analysis (TGA) (Mfg. by, TA Instruments, Model: Q50), at a ramp rate of 10° C/min.

6.2.3 Loading of Triphenyl phosphate (TPP) and FR-1 flame additive into halloysite

In order to load halloysite with triphenyl phosphate, 100 mg of halloysite is dispersed in 1 ml solution of triphenyl phosphate in acetone (150 mg/ml). Suspension is sonicated for 20 minutes in an ultrasonic bath in order to better suspend halloysite nanoparticles in the solution. Suspension is left in the vacuum jar (pressure \approx 100 torr) for 20 minutes followed by breaking the vacuum and vortex halloysite suspension. The sample was left in the vacuum after vortex and cycle are repeated 4 times for better loading of triphenyl phosphate. For the final cycle, the sample is left in the vacuum chamber overnight. Next day the halloysite is separated from the solution by centrifugation and washed twice with 1 ml of acetone to remove excess of phosphate from the external surface of halloysite nanotubes. The samples are dried in a vacuum chamber. FR-1 flame retardant is not soluble in acetone, but it forms a stable solution in

acetone, and therefore, halloysites are admixed with FR-1 suspended in acetone in a vacuum chamber with constant stirring. Next day, the samples are washed with acetone once to remove excess FR-1 from the halloysite surface.

6.2.4 Preparation of samples for flame retardant testing on wooden board

For the flame retardant testing, latex paint is mixed with halloysite nanotubes at different concentrations. For the testing wooden board is coated with the latex paint using Blue Hawk 7.25" synthetic paint brush. Wooden board coated with pure latex paint is counted as a control sample. For the next set of samples, 5 wt% and 7 wt% halloysite are mixed with the latex paint using a mechanical stirrer to break any halloysite clump for 30 minutes. This results in a uniformly mixed sample. Halloysite loaded with triphenyl phosphate is mixed with the paint sample following the same procedure. Afterwards, paint coating samples are air dried for 5 days.

6.2.5 Preparation of samples for flame retardant testing on metal

Flame retardant testing is also conducted on ASTM A366 steel metal surface. Before the application of paint metal surface is polished with sandpaper to remove residual oxide. Samples prepared for the wooden board tests are used for the metal surface testing as well. Paint is applied on a 3 cm x 3 cm block on the metal surface. Samples are air dried for 5 days.

6.3 Results & Discussion

6.3.1 Halloysite characterization using SEM

Halloysite nanotubes have lengths of 1-5 μ m, with lumen diameters of 10-15nm. Tiny pieces of broken tubules and incompletely rolled tubes are also observed. The length of the tubes is highly variable.

6.3.2 Analysis of Triphenyl phosphate loading efficiency into halloysite

Triphenyl phosphate loading efficiency into halloysite is analyzed by using thermogravimetric analysis (TGA). About 15 mg of triphenyl phosphate loaded halloysite sample is placed into a sample pan holder, and the sample is heated at a rate of 10^o C/min. Figure 6-1a shows the TGA curve for the pure triphenyl phosphate, where 100% of the sample is burned under 300^o C. Temperature at which the degradation starts is found to be about 215^o C. In the case of triphenyl phosphate loaded halloysite sample, the degradation point is visible at a temperature of 222^o C, which shows that triphenyl phosphate is loaded into the halloysite lumen (Figure 6-2). TGA curve shows a weight loss of 3.10% which due to the loss of water from the halloysite layers. A weight loss of 2.90% is found to be in the range of the temperature when triphenyl phosphate degrades, and the value is of the loading efficiency for the halloysite as well. Halloysite starts to degrade above 400^o C when the silica layer starts to degrade.

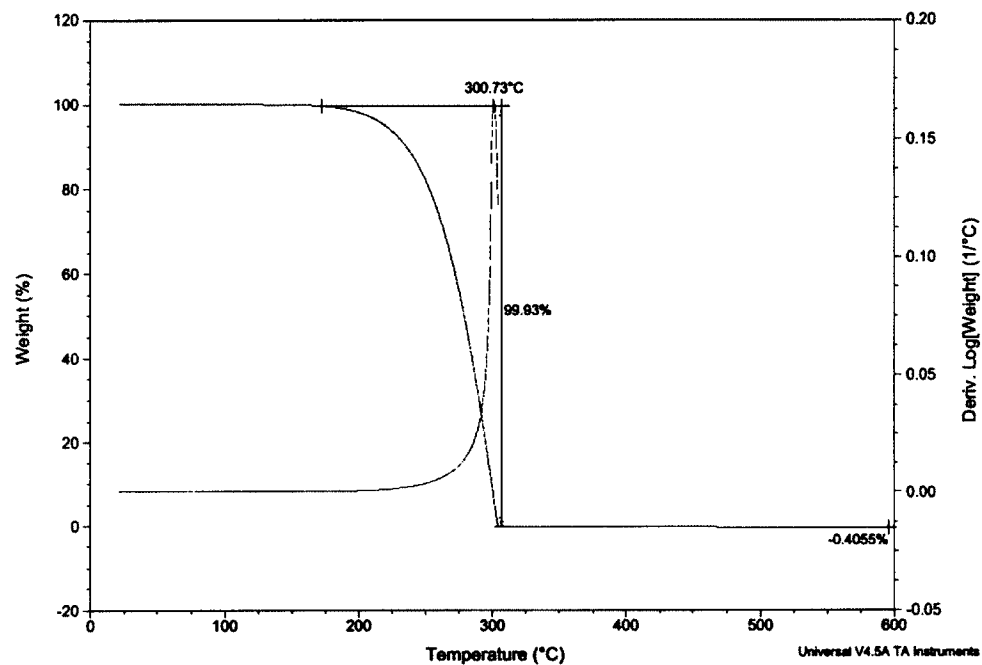


Figure 6-1: TGA curve for pure triphenyl phosphate (TPP).

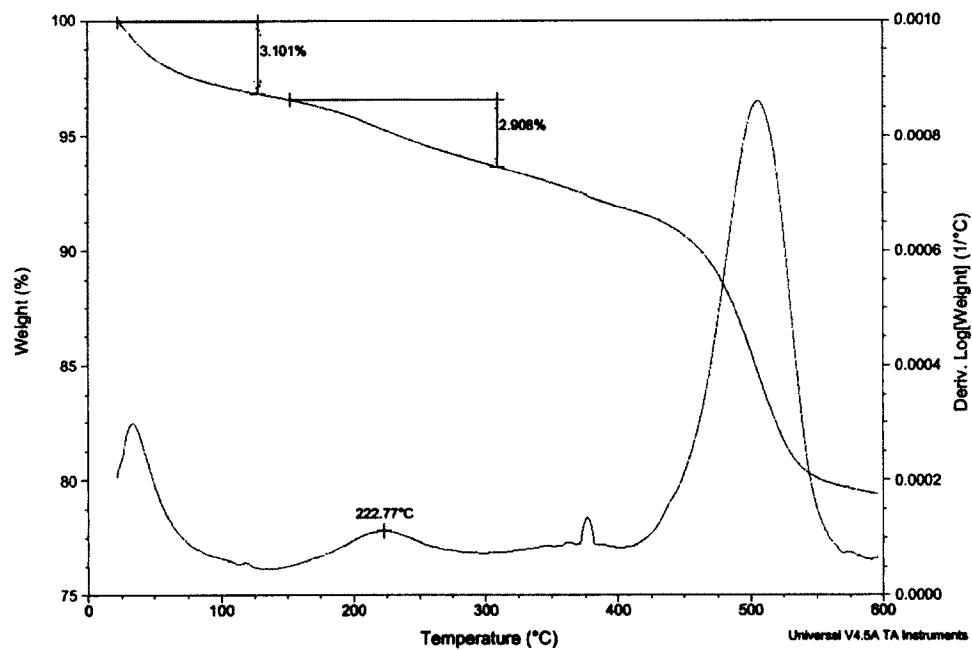


Figure 6-2: TGA curve for TPP loaded into halloysite nanotubes.

6.3.3 Halloysite admixed latex paint samples before flame test

After mixing and applying the paint on the wooden flake board and metal surface, it is observed that the paint characteristics such as its color and physical properties do not change. Therefore, it satisfies the criteria which is applied to a standard flame retardant. Figure 6-3 shows that the paint samples with 5 wt% and 7 wt% halloysite are comparable with the control paint sample in terms of its appearance. The thickness of the paint is about 1 mm.

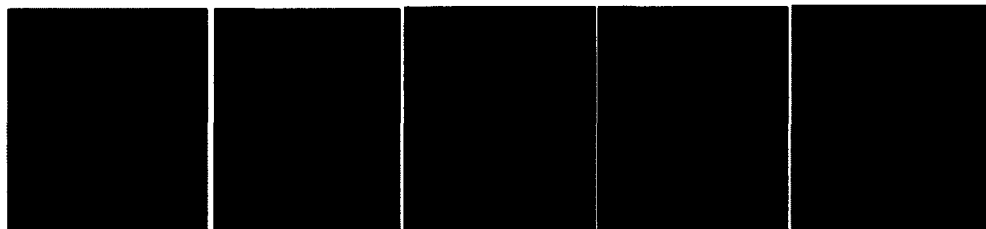


Figure 6-3: Wooden flake board samples applied with 1) pure paint, 2) paint + 5 wt% halloysite, 3) paint + 7 wt% halloysite, 4) paint + 5 wt% halloysite with FR-1, 5) paint + pure FR-1.

In the case of paint coated metal samples, the observations are similar. As shown in Figure 6-4, the latex color and surface morphology do not change after addition of halloysite nanotubes. Therefore, this shows that halloysite nanotubes can be used as an additive in the paint for different surfaces. For 7 wt% halloysite, the surface appears to be rough and grainy. This could be because of the higher wt% of halloysite nanotubes.

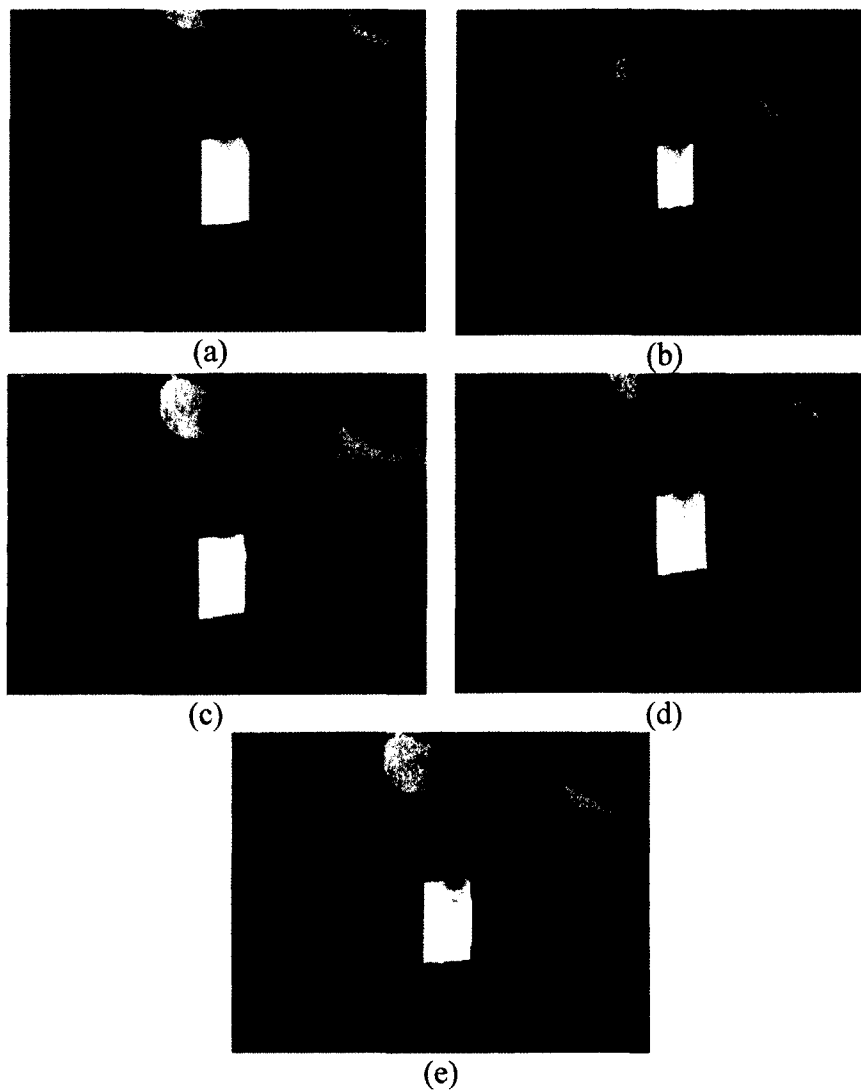


Figure 6-4: ASTM A366 steel metal surface coated with a) pure paint, b) paint + 5 wt% halloysite, c) paint + 7 wt% halloysite, d) paint + 5 wt% halloysite with FR-1, e) paint + pure FR-1.

6.3.4 Halloysite admixed latex paint samples after flame test on wooden board

The flame retardant property of the paint coated wooden board and metal samples are burned with a handheld Benzomatic™ flame torch. For the flame retardant tests, the distance between the samples and the flame nozzle is approximately 10 cm in all the

cases. All the samples are fixed on a metal plate, and the flame is concentrated at the center of each sample. Samples are exposed to the direct flame for 30 seconds. Figure 6.5a shows the pure paint sample after burning. The sample burns profusely compared to the other samples. Surface characteristics show that after complete burning and self-extinguishing, the paint lift-off from the wooden surface is observed, indicating less adhesivity on the wooden board. Smoke developed is noticeable for up to ~10 seconds. Latex paint with 5 wt% halloysite burns slowly compared to the controlled sample (Figure 6.5b). Though the flame spread is almost the same like the controlled sample. Surface characteristics show better adhesion compared to the rest of the samples as no paint lift-off is observed. Also, the flame developed is less compared to the controlled sample. In the case of paint with 5 wt% halloysite, no blister formation is observed, which indicates improved paint surface characteristics, and the flame do not penetrate into the paint's surface.

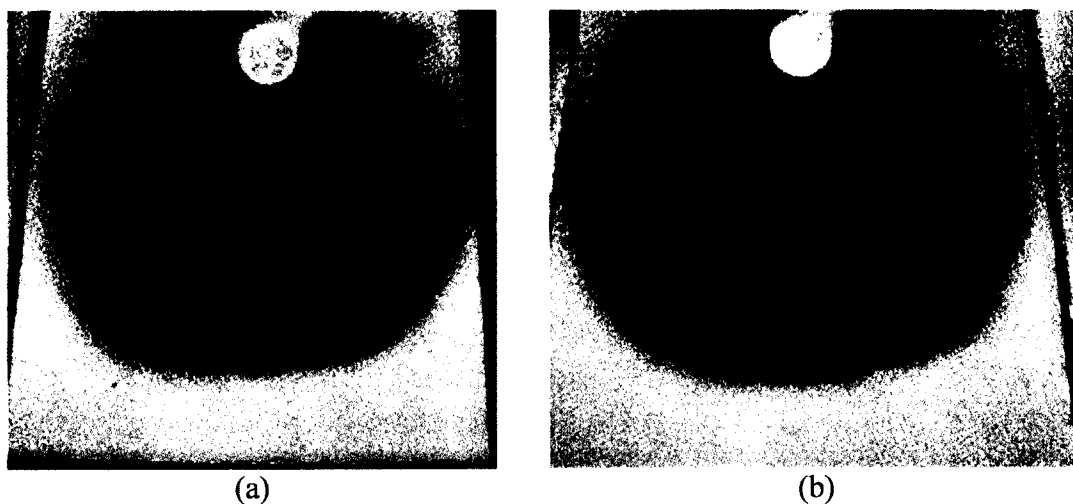


Figure 6-5: a) Pure paint sample after flame test, b) Paint +5 wt% halloysite sample after flame test.

Paint with 7 wt% halloysite burns for a longer time compared to the paint with 5 wt% halloysite (Figure 6-6c). After burning the samples, paint lift-off is observed, which results from the blister formation on the paint's surface. This could be because of the higher percentage of halloysite in the paint which resulted in the aggregated halloysite, and then blister formation. Flame penetrated into the paint, resulting in the lift-off. Figure 6-6d shows the flame testing of latex paint sample mixed with FR-1 loaded halloysite nanotubes. The flame spread area is comparatively larger than the other samples. It is observed that within 10 seconds after exposure the wooden surface is exposed to the direct flame as the top layer starts to fail. This resulted in more smoke development which may lead to the immediate combustion. This is not observed for the samples with 5 wt% and 7 wt% halloysite.

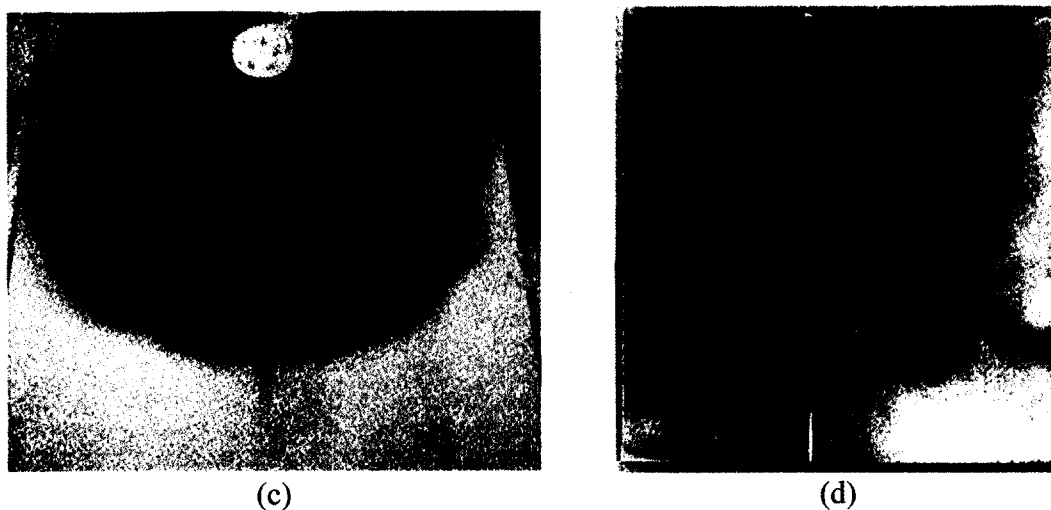


Figure 6-6: c) Paint +7 wt% halloysite sample after flame test, d) Paint with 5 wt% FR-1 flame retardant admixed with halloysite.

In the case of TPP loaded halloysite paint samples, flame spread is controlled compared to the control sample (Figure 6-7e). However, paint lift-off is observed which is not visible in the case of paint with 5 wt% halloysite. Also, the smoke developed is less compared to the previous samples, and the flame extinguished within 10 seconds. In comparison of the paint + 5 wt% FR-1 flame retardant (Figure 6-7f) paint with 5 wt% halloysite loaded with triphenyl phosphate (TPP), the later paint sample is more burned, and results in more smoke development than the paint sample with halloysite. This trend is observed in comparison with the other samples, also. Paint containing halloysite in general resulted in less smoke than the paint sample with FR-1 flame retardant.

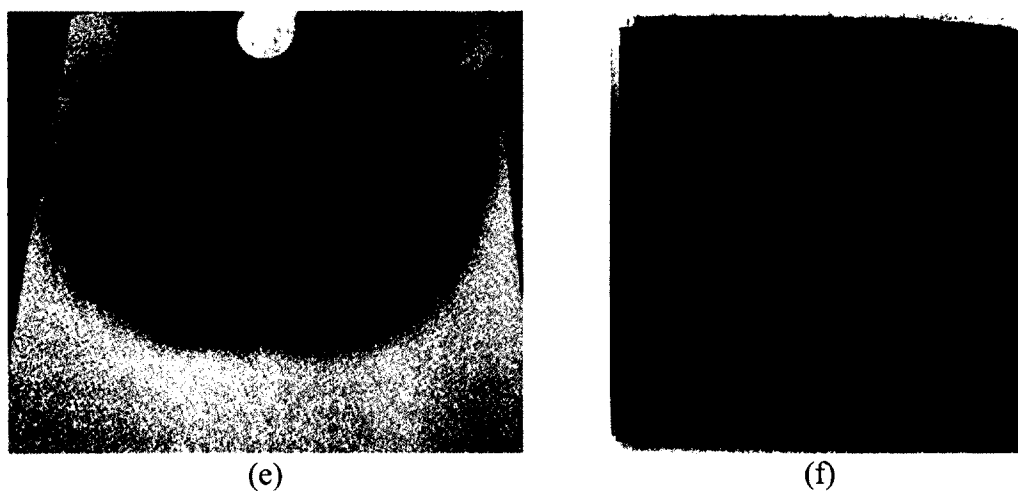


Figure 6-7: e) Paint with 5 wt% Halloysite loaded with TPP, f) Paint + 5 wt% FR-1 flame retardant.

6.3.5 Halloysite admixed latex paint samples after flame test on metal

Flame testing on metal is found to produce the similar results in comparison with the flame test on the wooden board. In the case of metals where the sample is exposed to the flame, it is a two-way heating, from the metal and from the flame. As shown in

Figure 6-8 a-f the sample's appearance is changed based on its composition. In the case of pure latex paint sample (Figure 6-8a) the sample gets charred after 30 seconds of exposure. The results are similar to that of paint with 5 wt% FR-1 flame retardant additive as well (Figure 6-8e). In the case of 5 wt% halloysite, the sample is less burned compared to the rest of the samples (Figure 6-8b). The surface properties are also maintained for the paint samples containing halloysite nanotubes. Paint with 5 wt% halloysite is found to have less surface abnormalities than the other samples. In the case of 7 wt% halloysite, the paint does not get charred but is more burned than the sample with 5 wt% halloysite (Figure 6-8c). This could be because of higher concentration of halloysite, which resulted in the agglomeration of halloysite nanotubes in paint. However, when FR-1 flame additive is admixed with halloysite nanotubes after 30 seconds of exposure, the sample does not get charred unlike paint with pure FR-1 flame additive.

In the case of 5 wt% halloysite sample, the smoke generated is far less than the paint sample with and without FR-1 flame retardant additive. Therefore, it blocks further combustion of the sample, and the self-extinguishing point for the paint with 5 wt% halloysite sample is less than the pure paint sample, and paint with pure FR-1 flame retardant.

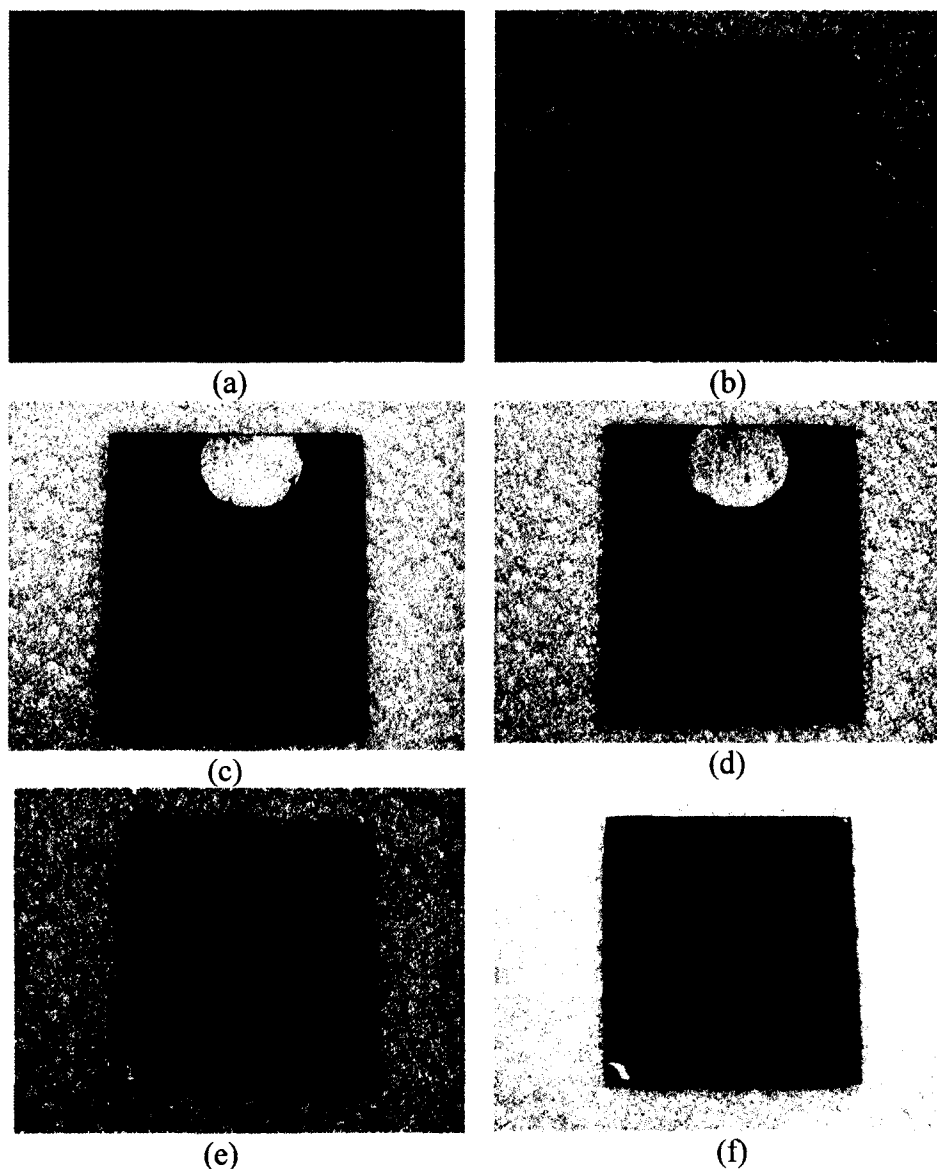


Figure 6-8: Paint samples after burn test on metals, a) Pure latex paint, b) Paint + 5 wt% halloysite, c) Paint + 7 wt% halloysite, d) Paint + 5 wt% FR-1 loaded halloysite, e) Paint + 5 wt% FR-1 additive, f) Paint + 7 wt% FR-1 additive..

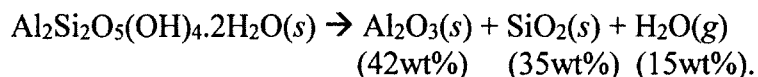
6.3.6 Possible mechanism of halloysite flame retardancy

Halloysite flame retardancy could be because of the degradation of the aluminum oxide from the halloysite interlayer. Aluminum trihydrate, a commonly used flame

retardant, upon degradation releases water molecules which slows down the rate of combustion [112].



Similarly, upon degradation at a higher temperature, the reaction products of halloysite include:



Halloysite upon degradation breaks down into 3 major components: aluminum oxide, silicon dioxide, and water molecules [114]. Therefore, it can be proposed that at a higher temperature of about 600-700° C halloysite degrades and releases water molecules, which slow down the rate of combustion by capturing the free radicals and result in the flame self-extinguishing [112].

Figure 6-9a-d are the optical microscopic image of the burned samples, containing 5 wt% and 7 wt% halloysite. For the 5 wt% halloysite sample paint, the blister formation is distributed on the overall surface, which shows that the halloysite nanotubes are uniformly distributed in the paint, and therefore the blister formation could be a result of interlayered release of the water molecules (Figure 6-9a). In the case of 7 wt% halloysite the blisters are not uniformly distributed and are concentrated in certain areas. This could be because of agglomeration of the halloysite nanotubes in the paint, which results in the release of water molecules in that particular area resulting in bulging in the paint (Figure 6-9d).

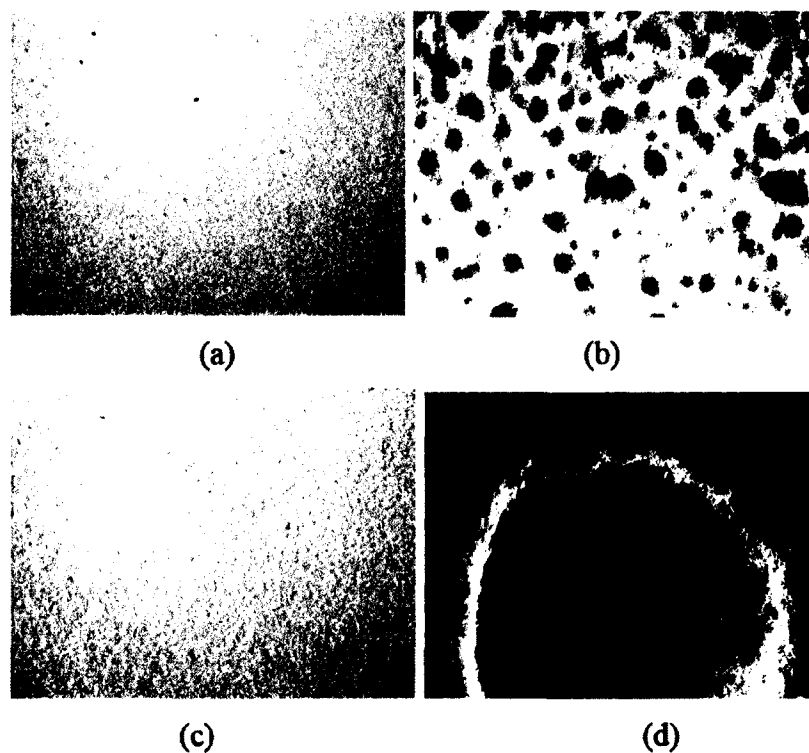


Figure 6-9: Optical microscopic images of a) Paint + 5 wt% halloysite before flame test, b) Paint + 5 wt% halloysite after flame test, c) Paint + 7 wt% halloysite before flame test, d) Paint + 7 wt% halloysite after flame test.

6.4 Conclusion

Halloysite nanotubes are used as a nanocontainer for the flame retardant agents, triphenyl phosphate and FR-1 paint additive. It is observed that halloysite itself acts as a flame retardant when mixed with a latex paint at 5 wt% and 7 wt%. Halloysite satisfies all the conditions required for a flame retardant before it is mixed with a polymer or paint. It does not change the color or the overall appearance of the latex paint. The samples tested are according to the ASTM E84 standards, where the inferences are made based on the flame spread, and smoke developed. Among the samples tested, latex paint with 5 wt% halloysite is found to have better flame retardant properties. The adhesion

properties of the paint are also found to be better for the 5 wt% halloysite containing paint, because for the other samples, surface lift-off is observed which suggests poor surface properties. In the case of testing on metal surface 5wt% halloysite containing paint sample has better flame resistivity than the other samples. The flame spread and smoke developed is also less for the same case. Halloysite degradation resulting in degradation and release of water molecule could be a reason for the decreasing rate of combustion.

CHAPTER 7

GEOPOLYMERS PROPERTIES OPTIMIZATION WITH FLY-ASH MICROPARTICLE COATING WITH NANOCCLAYS

In this last chapter, we extend the clay nanotube coating method for encapsulation of fly ash microparticles with halloysite using the Layer-by-Layer (LbL) technique and optimize these microcore-nanoshell concrete samples for an extended curing time (parameters which is much needed in industry). A paper on these results is invited by the editor for a special nanoarchitectonic issue of *J. Inorganic & Organometallic Polymers Materials*. It is in preparation and will be submitted by August 15: **A. Joshi**, C. Montes, E. Allouche, Y. Lvov, *J. Inorganic & Organometallic Polymers Materials*, v.25, May 2015, "Geopolymers properties optimization with fly-ash microparticle coating with nanoclays."

7.1 Introduction

Ordinary Portland Cement (OPC) is one of the major sources for CO₂ emission in the environment, as the OPC preparation requires burning of large amounts of fuel, and the decomposition of limestone [115]. Geopolymer based cement (GPC) offers an alternative to the use of conventional use of OPC. Geopolymer concrete offers advantages over OPC such as high compressive strength, low shrinkage, and good acid resistance properties. The fly ash particles mainly consist of silicon dioxide, and

aluminum oxide, with other trace metals also present such as iron, and calcium in oxide form [116]. Geopolymer concrete curing time depends on different factors such as molarity of NaOH, moisture content, and curing temperature. These factors also affect the compressive strength of the geopolymer concrete. For the geopolymer concrete the initial setting time plays an important role as the geopolymerization reaction is an exothermic reaction, and it catalyzes the reaction of fast curing [117]. In the case of high calcium content fly ash, this problem is worse as it reacts faster. Therefore, there is a need for an additive to extend the setting time of the geopolymer concrete.

In this study, we are going to explore the use of halloysite nanotubes to extend the initial setting time for the geopolymer cement. This will be achieved by the coating of halloysite nanotubes on the fly ash particles by using the Layer-by-Layer (LbL) approach. The LbL approach involves the deposition of alternative layers of polycation and polyanion onto a substrate [118]. We have used this approach for the coating of fly ash particles with halloysite. The LbL approach helps to deposit a dense layer of halloysite on fly ash particles.

Two different types of fly ashes are used for this experiment, one being a positively charged fly ash, and the other a negatively charged fly ash. Change in the surface charge with the deposition of polyelectrolytes is investigated using zeta potential analyzer. Two different halloysite mixing with fly ashes are explored. First approach is mixing of dry halloysite with dry fly ash, and second approach is mixing halloysite with geopolymer paste. Halloysite nanotubes are added into the fly ash with a concentration of 3 wt% and 6 wt%. The molarities of NaOH solution are 10 M, and 12 M. The best method is chosen based on the initial investigation. Halloysite coating on the fly ash is

analyzed using SEM. Viscosity of the sample is characterized by conducting rheology tests. Last, setting time tests are conducted by mixing halloysite with fly ash at different concentrations.

7.2 Materials and Methods

7.2.1 Materials

Halloysite nanotubes were acquired from Applied Mineral Inc., New York, USA. Polyelectrolytes, polyethylenimine (PEI) (MW: 2000), and polyacrylic acid (PAA) (MW: 5100) are purchased from Sigma Chemicals. Dollet hill fly ash and montecello fly ash are acquired from Trenchless Technology Center, Louisiana Tech University, Ruston, LA. We purchased Sodium hydroxide and sodium silicate from Sigma-Aldrich.

7.2.2 Instrumentation

The morphology of halloysite and fly ash was characterized by Scanning Electron Microscope (Hitachi S 4800 FE-SEM) at 5-15 kV. Halloysite is coated with 0.5 nm gold by Cressington Sputter coater (208HR) at 20 mA for 1 min. Halloysite coating on fly ash is also visualized with the same parameters. Surface charge of the fly ash particles, and change in their surface charge with deposition of polyelectrolytes was conducted using ZetaPlus Zeta potential analyzer (Brookhaven Instruments, New York, USA). Viscosity of the halloysite-fly ash mixture is measured using Brookfield DV-III Ultra Rheometer. Setting time analysis is conducted with a Vicat needle test.

7.2.3 Mixing of halloysite nanotubes with fly ash

Halloysite nanotubes are mixed with fly ash by first preparing the paste of fly ash. For the preparation of fly ash paste the following components are added:

Paste samples

1. 20 grams of Dollet Hills fly ash per sample.
2. Silicate N from PQ.
3. Sodium hydroxide solution of different molarities.
4. Halloysite nanotubes (3 and 6 wt% of fly ash).
5. Activator solution/Fly ash ratio: 0.5
6. Silicate/hydroxide ratio: 1.5

Procedure 1: Adding halloysite to fly ash

1. Halloysite is premixed dry with the fly ash for 30 seconds.
2. The dry mix of fly ash and halloysite is mixed with sodium silicate for 30 seconds.
3. Sodium hydroxide is added for 30 seconds.
4. Paste samples are mixed until a homogeneous mix is achieved.
5. Rheology test begins five minutes after the start of the mixing.

Procedure 2: Adding halloysite into geopolymer paste

1. Fly ash is mixed with sodium silicate for 30 seconds.
2. Sodium hydroxide is added for 30 seconds.
3. Halloysite is added to the mix.
4. Paste samples are mixed until a homogeneous mix is achieved.
5. Rheology test begins five minutes after the start of the mixing.

7.2.4 Layer-by-Layer (LbL) coating of fly ash with polyelectrolytes

The LbL assembly on the surface of fly ash particle is surface charge dependent.

In the case of dollet hill (DH) fly ash, the initial surface charge measured using zeta

potential analyzer is +21 mV; therefore, first polyanion, PAA (Figure 7-1a), is deposited. A 10 mg/ml solution of PAA is prepared with 0.5 M NaCl solution for better deposition on the surface. A 200 mg of fly ash is mixed with 10 ml of PAA solution. The sample is mixed on a magnetic stirrer for 1 hour. Then the sample was centrifuged at 7000 rpm for 5 minutes. The supernatant is discarded, and the sample was washed with 0.5 M NaCl solution two times to remove excess PAA from the surface. The fly ash sample is then mixed with 10 mg/ml solution of polycation, PEI (Figure 7-1b) for 1 hour. Centrifugation and washing procedure is repeated. The sample is dried in a vacuum chamber overnight. The next day the dried fly ash particles are mixed with 6 wt% of halloysite for SEM imaging. In the case of negatively charged montecello fly ash (MO) the polyelectrolyte deposition process is reversed. MO has an initial surface charge of -22 mV. Therefore, the first layer deposited is of polycation PEI, followed by PAA. The washing process after each stage is similar to that of DH fly ash. In both cases after deposition of each layer, a small sample quantity is stored in centrifuge tubes for the measurement of change in surface charge after deposition of polyelectrolytes.

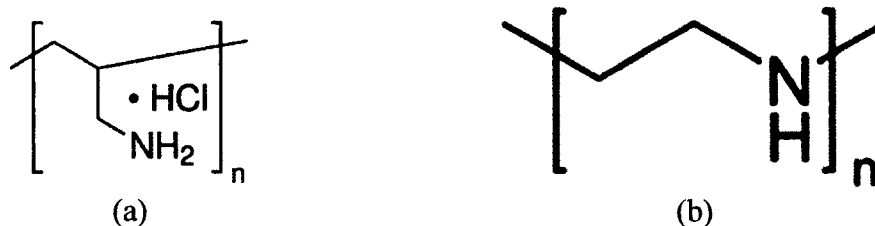


Figure 7-1: a) Chemical structure for PAA, b) PEI.

7.2.5 Flow test and viscosity measurements

Flow table test is conducted and the measurements are made based on the sample spread. The values are obtained for the pure fly ash, fly ash with 3 wt% and 6 wt% halloysite. Also, the dynamic viscosity is conducted using Brookfield DV-III Ultra Rheometer. A small adapter and a SV4-27 spindle are selected for all the experiments. The mixing speed is set at 5 rpm for all the experiments.

7.3 Results and Discussion

7.3.1 Halloysite and fly ash characterization by SEM

Halloysite nanotubes have lengths of 1 to 5 μm . Few fragments of broken nanotubes are also visible on the surface. This could be the result of processing (Figure 7-2a). Fly ash particles are spherical in shape with the size of the particles ranging from 10 μm to 150 μm (Figure 7-2b).

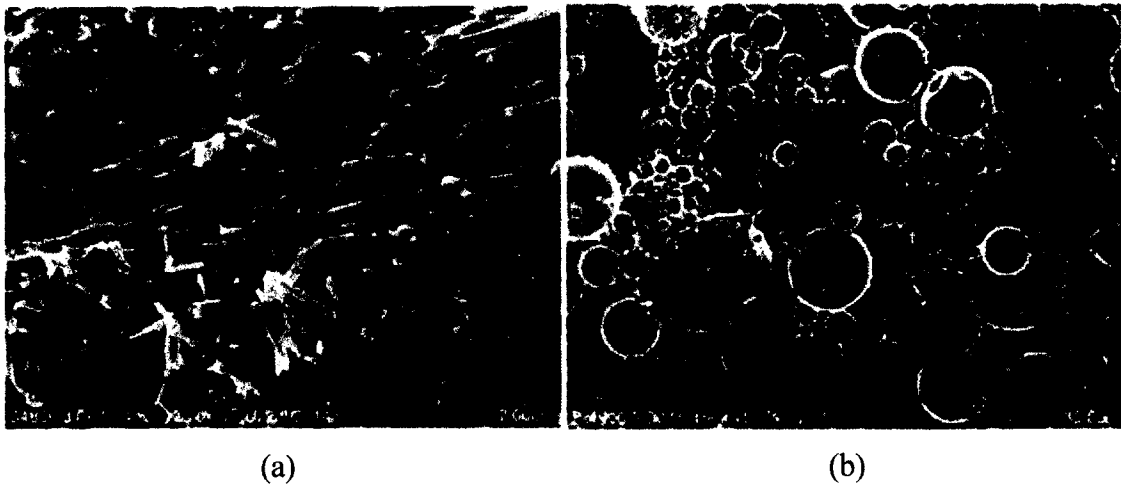


Figure 7-2: SEM images of a) halloysite nanotubes, b) dry fly ash [119]

7.3.2 Halloysite interaction with activating solution in fly ash mixture

Halloysite was mixed with fly ash in two different ways. In the first procedure halloysite was first mixed with the fly ash and then exposed to the activation solution. In the second approach, halloysite is added into the geopolymer paste prepared by mixing fly ash with the activation solution. In Figure 7-3a, the sample for 10 M hydroxide geopolymer halloysite can be found in the cracks of the material. In samples for 12 M halloysite nanotubes are found most preferentially surrounding fly ash particles (Figure 7-3b). In Figure 7-3c, it can be seen that when adding 6% of halloysite to the fly ash, halloysite nanotubes tend to form agglomerates and interact with each other. However, they are still found surrounding the fly ash particles and covering a much larger area of the particles than in the case of 3%. It is very likely that the addition procedure has a large impact on the location and degree of attack of the halloysite nanotubes in the geopolymer.

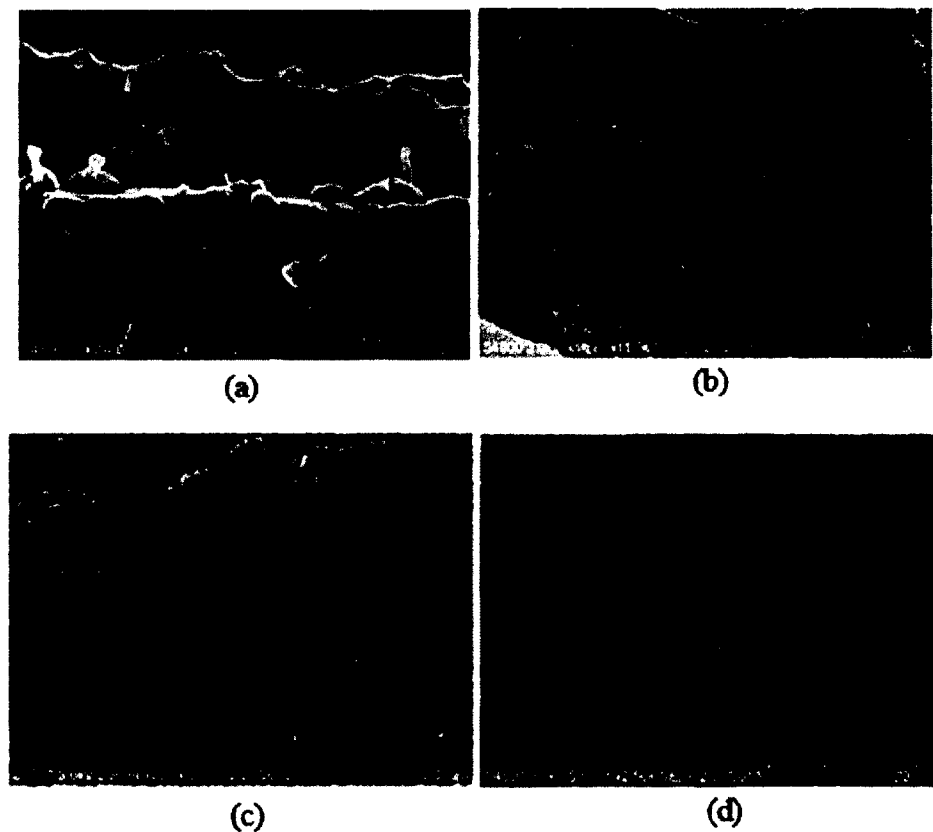


Figure 7-3: a) 3% halloysite pre-mixed with fly ash particles in 10 M NaOH, b) 3% halloysite pre-mixed with fly ash particles in 12 M NaOH, c) 6% halloysite pre-mixed with fly ash particles in 10 M NaOH, d) 6% halloysite pre-mixed with fly ash particles in 12 M NaOH.

In the second approach when halloysite nanotubes were added into the geopolymer paste, the halloysite are predominantly found in the matrix. In Figure 7-4a and b, when 3% of halloysite is mixed with the geopolymer paste, the nanotubes do not appear surrounding fly ash particles that often, but look embedded in the mix. In the case of 6% halloysite added to geopolymer paste, the halloysite nanotubes can be found both in the paste and the surrounding fly ash particles (Figure 7-4c and d).

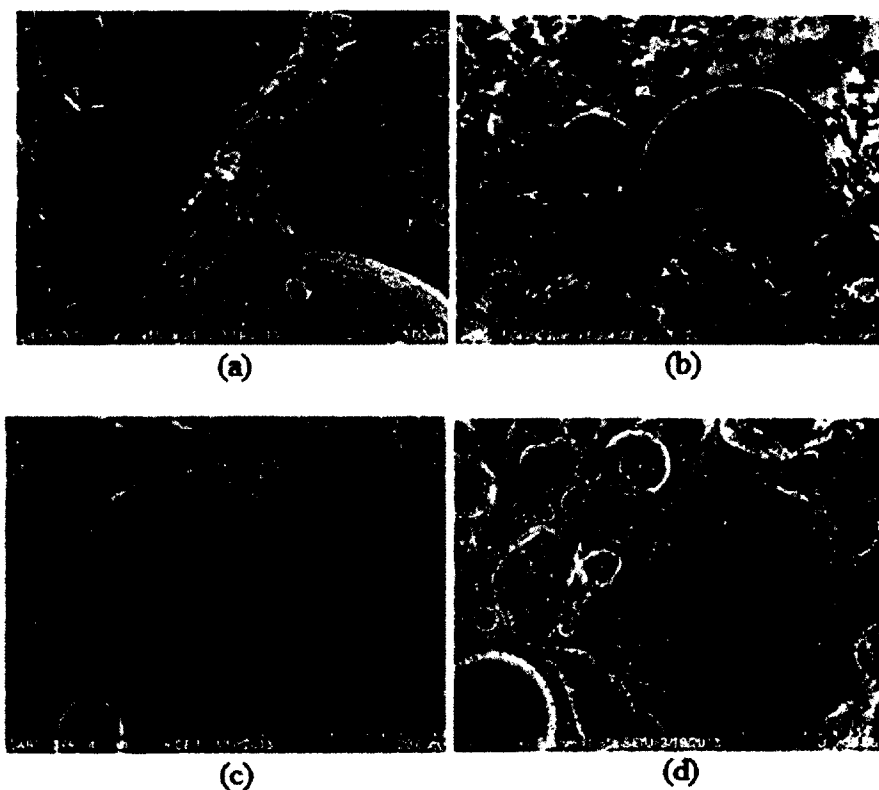


Figure 7-4: a) 3% halloysite mixed with the geopolymer paste in 10 M NaOH, b) 3% halloysite pre- mixed with the geopolymer paste in 12 M NaOH, c) 6% halloysite mixed with the geopolymer paste in 10 M NaOH, d) 6% halloysite mixed with the geopolymer paste in 12 M NaOH.

7.3.3 Layer-by-Layer assembly for fly ash coating with halloysite

In order to improve the coating of the halloysite on the fly ash surface the LbL approach is implemented. As mentioned before, in the case of positively charged DH fly ash, it is first coated with the polyanion, followed by a layer of polycation. After each deposition surface charge was measured to ensure successful coating. Figure 7-5 shows the scheme of LbL coating of polyelectrolytes onto fly ash surface.

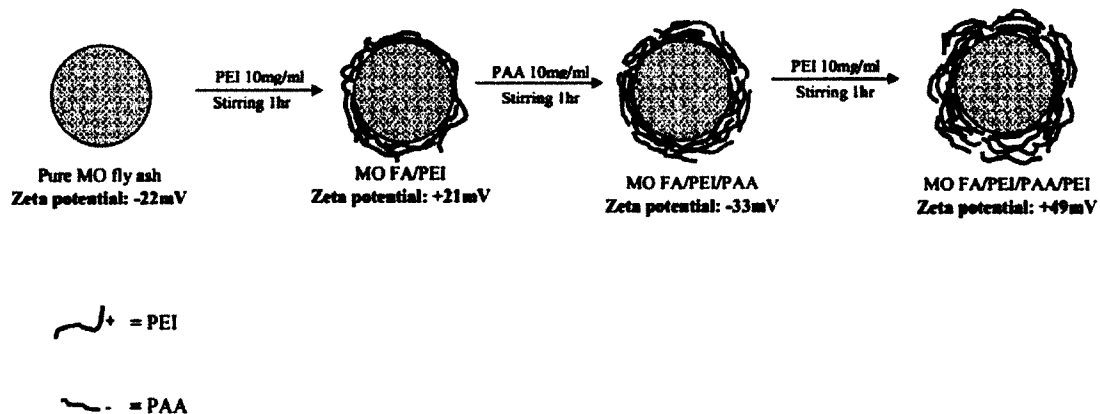


Figure 7-5: Schematic representation of LbL assembly on MO fly ash surface.

In the case of DH fly ash, the initial surface charge measured is found to be +21 mV. After deposition of PAA, the surface charge shifted into negative scale to -43 mV, indicating a successful deposition of polyanion onto surface. The surface charge again shifted into positive range after deposition of PEI and is found to be +55 mV. These results suggest that the fly ash surface can be modified with the deposition of polyelectrolytes. The shift in the surface after deposition of each layer for DH fly ash is shown in Table 7-1. In the case of pure DH fly ash, a control sample is also prepared, which consists of pure fly ash and halloysite. As DH fly ash has a positive surface charge, halloysite nanotubes can be easily deposited on its surface as they have a naturally negatively charged surface.

Table 7-1: Change in surface charge with deposition of polyelectrolytes for Dollet Hill fly ash.

| Layer | Zeta potential (mV) |
|--------------------|---------------------|
| Control DH fly ash | +21 |
| DH FA/PAA | -43 |
| DH FA/PAA/PEI | +55 |

The coating of halloysite on the DH fly ash is visualized using SEM (Figure 7-6). It is observed that the coating after LbL coating is much denser than the control sample, which indicates that the LbL coating of polyelectrolytes help with the fly ash coating as it improves the uniform halloysite coating capability.

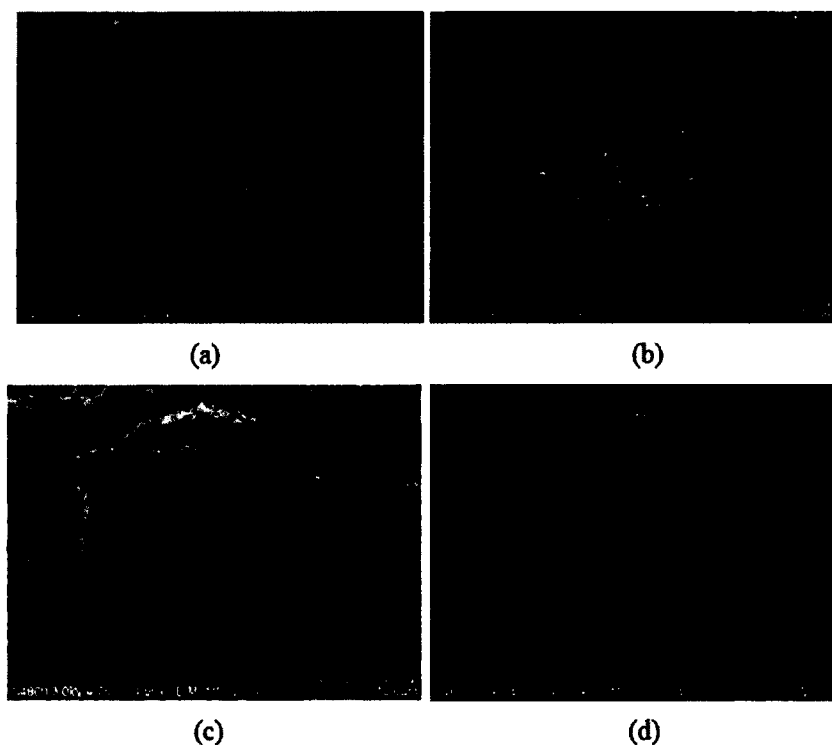


Figure 7-6: a), and b) Dry DH fly ash mixed with 6% halloysite before LbL coating, c), and d) DH fly ash mixed with 6% halloysite after LbL coating.

In the case of montecello fly ash which bears negative surface charge, the surface modification is initiated with a polycation, PEI. The zeta potential measurements are made after the deposition of each polyelectrolyte layer onto the fly ash. As mentioned before, MO fly ash has a surface potential of -22 mV; therefore, it has a strong attraction towards polycation. After the deposition of polycation, it is followed by the mixing of the sample with polyanion, which again shifts the surface charge to negative, and it again shifts to positive after mixing with polycation being the last layer of the LbL treatment.

Table 7-2 shows the values of the zeta potential measured after the deposition of each polyelectrolyte layer.

Table 7-2: Change in surface charge with deposition of polyelectrolytes for Dollet Hill fly ash

| Layer | Zeta potential (mV) |
|--------------------|----------------------------|
| Control MO fly ash | -22 |
| MO FA/PEI | +21 |
| MO FA/PEI/PAA | -33 |
| MO FA/PEI/PAA/PEI | +49 |

SEM images show that when untreated MO fly ash was mixed with the halloysite, there was no coating of the halloysite on the surface. This is because of the negative charge repulsion from both surfaces (Figure 7-7 a and b). After the modification of fly ash surface with PEI, the surface become positively charged and the halloysite coating on the surface is clearly visible (Figure 7-7c and d).

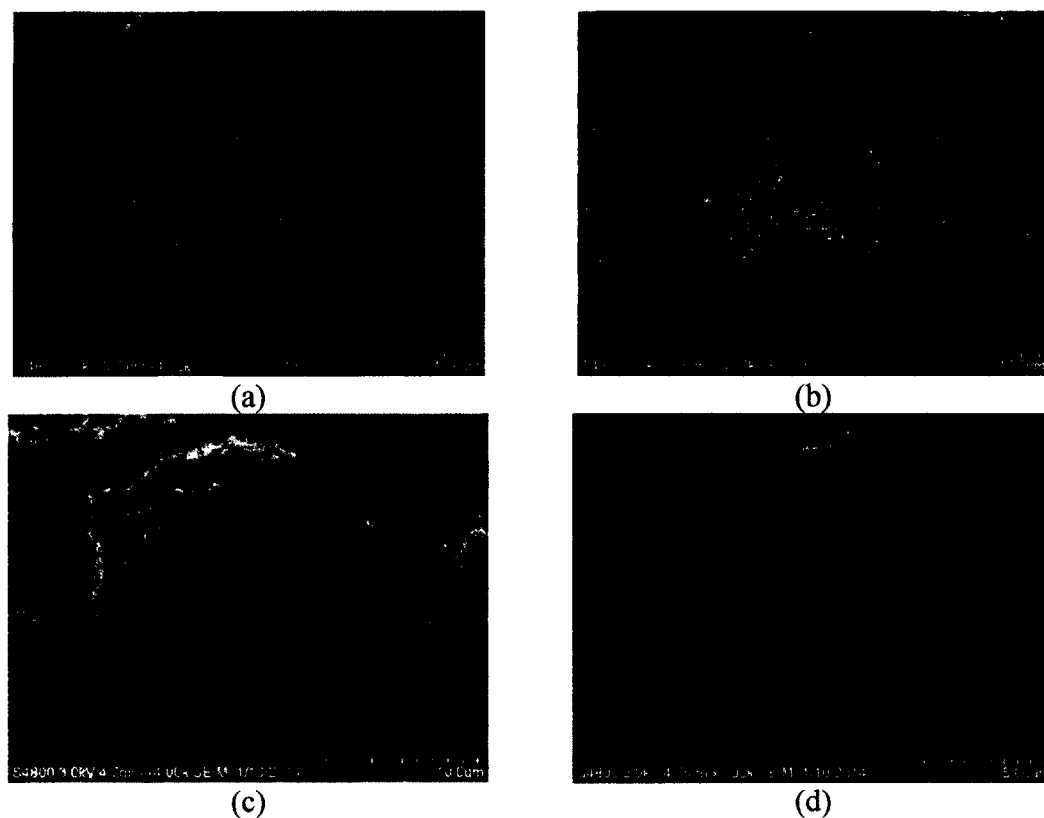


Figure 7-7: a) and b) Dry DH fly ash mixed with 6% halloysite before LbL coating, c and d) DH fly ash mixed with 6% halloysite after LbL coating.

7.3.4 Flow test and Rheology tests results

For the flow test, it is observed that with an increase in the molarity of the NaOH solution and concentration of halloysite nanotubes, the flow value of the paste decrease. However, the flow decrease is slightly less when adding the halloysite to the fly ash than when adding it to the paste. Figure 7-8a shows the flow values observed for two different methods. It is clearly visible that at 10 M NaOH, the concentration flow value is low when halloysite is added into the paste compared to the flow value of the samples when the halloysite nanotubes are pre-mixed with the fly ash (Figure 7-9). At 12 M NaOH concentration when halloysite is pre-mixed with the fly ash, there is no difference in the flow for the control sample and the fly ash pre-mixed with 3% of halloysite. Flow values

are also checked at higher molarity of NaOH solution (14 M) to check the behavior of the mixture. It is observed that when the fly ash is pre-mixed with the halloysite, the flow overall decrease at both concentration of the halloysite.

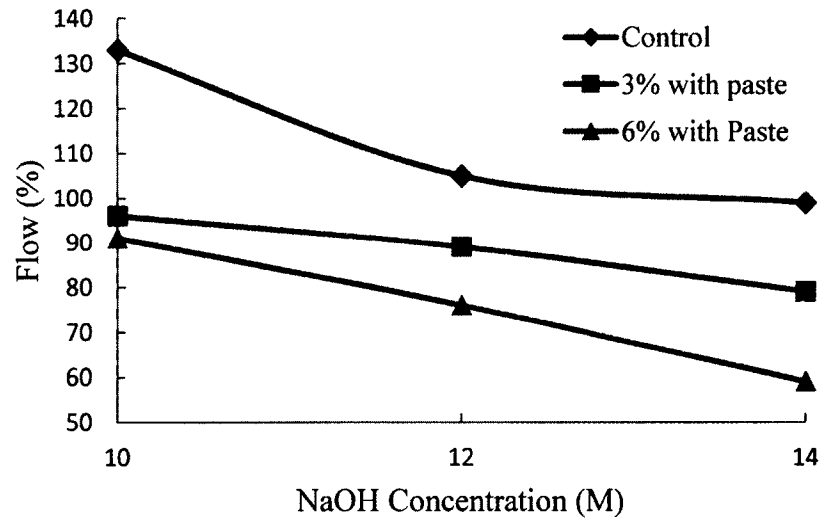


Figure 7-8: Flow test for the DH fly ash pre-mixed halloysite sample (dry process).

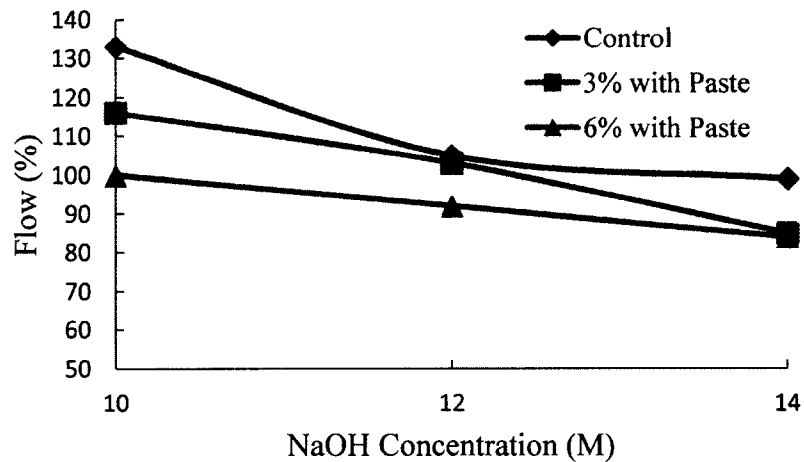
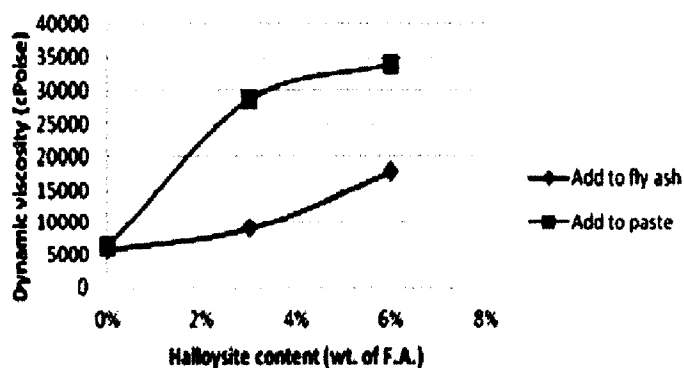


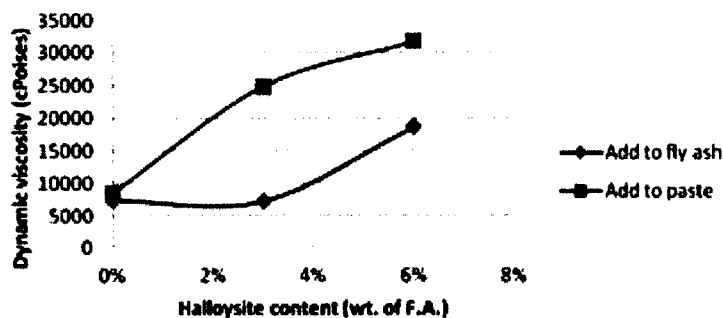
Figure 7-9: Flow test for the halloysite mixed with the DH fly ash geopolymer paste sample (wet process).

Rheology tests show that with an increase in the molarity of NaOH and the concentration of the halloysite nanotubes, the viscosity of the sample increases. These

results are in agreement with the flow table tests. Figures 7-10 a and b show that an increase in halloysite content increases the viscosity of the geopolymer samples in every case. The mixing method has a significant effect. When the halloysite is added to the paste, the viscosity is much higher than when it is added to the fly ash and pre-mixed dry, possibly because of a poorer degree of dispersion in the first case. The results are consistent with flow tests which show the same tendency. Table 7-3 shows the improvement in setting time after the addition of halloysite into MO fly ash.



(a)



(b)

Figure 7-10: Dynamic viscosity values for geopolymer paste prepared with a sodium hydroxide solution of 10 M (a), 12 M (b) for different halloysite loadings and mixing procedures [Blue-wet process, Red-Dry process].

Using Vicat needle the setting time of the sample with and without the addition of halloysite is measured (Table 7-3). In the case of the controlled specimen, the initial setting is 18 minutes, and the sample set in after 25 minutes. After the addition of halloysite into the MO fly ash, the initial setting time drastically increase to 47 minutes, and the final setting time is 49 minutes. After the addition of 6% of halloysite, the initial setting time increase to 117 minutes, and the final setting time is 147 minutes. It clearly shows that the method of halloysite addition affects the dispersion of the sample. When 6% of the halloysite is pre-mixed with the fly ash, the initial setting time is 175 minutes, and the sample cures after 205 minutes.

Table 7-3: Setting times for geopolymer + halloysite pastes prepared out of Monticello fly ash.

| Mixing type | Setting Time(average value of 2 tests) | |
|------------------|---|-------------------|
| | Initial | Final |
| Control Specimen | 18 minutes 24 sec | 25 minutes 43 sec |
| 3 % with Paste | 47 minutes 55 sec | 49 minutes 49 sec |
| 3 % with Fly Ash | 70 minutes 35 sec | 85 minutes 45 sec |
| 6 % with Paste | 117 minutes | 147 minutes |
| 6 % with Fly Ash | 175 minutes | 205 minutes |
| Control Specimen | 18 minutes 24 sec | 25 minutes 43 sec |

Rheology conducted on the LbL coated sample show that in the case of MO fly ash at room temperature after mixing with a controlled 6% halloysite, the viscosity is less than the control MO fly ash (Figure 7-11). It could be a result of the halloysite not coating the surface of the halloysite and instead it increase the viscosity of the solution, and cure in 10 minutes. When the MO fly ash surface was coated with the polyelectrolytes, the halloysite covers the surface of the fly ash, and therefore the viscosity of the sample is achieved similar to the controlled sample, but the setting time is

extended to 1 hr. It clearly shows that the halloysite successfully coated the fly ash surface, and therefore it delay the geopolymerization reaction, thereby increasing the setting time of the cement. The study will also be conducted at 50° C.

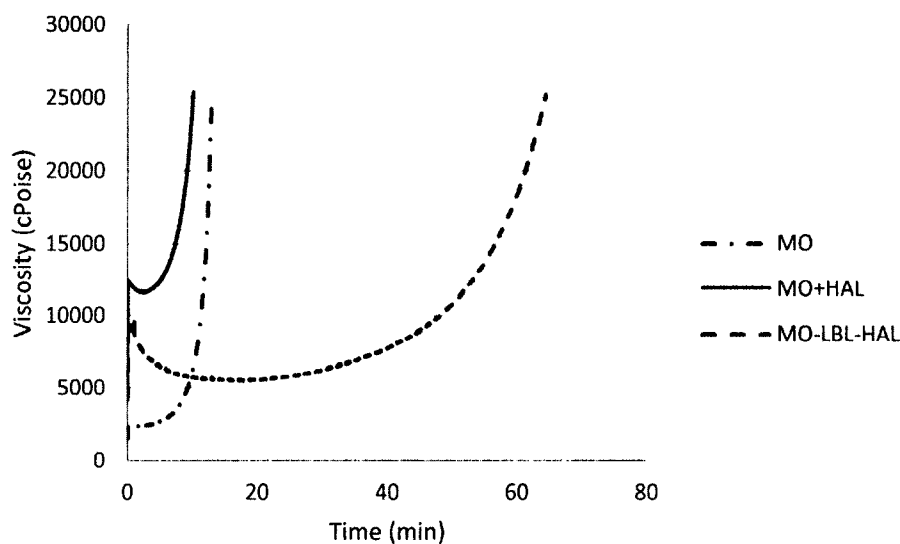


Figure 7-11: Viscosity at room temperature for controlled MO fly ash, fly ash with controlled 6% halloysite, and fly ash with 6% treated halloysite.

Rheology study is conducted on the control DH fly ash, DH fly ash mixed with 6% halloysite, and LbL treated DH fly ash mixed with 6% halloysite at 50° C. Practically at higher temperature, fly ash has the ability to set rapidly. For the controlled DH fly ash and the fly ash with 6% halloysite, they follow a similar trend for the viscosity, and they set in less than 1 hr. In the case of LbL coated fly ash with 6% halloysite the viscosity of the sample is higher with an increased setting time of nearly to 2 hrs (Figure 7-12). As shown in SEM (Figure 7-6) halloysite can coat the positively charged fly ash surface better viscosity was not achieved than the control fly ash sample. When the fly ash surface is modified with the polyelectrolytes, the halloysite coating on the surface is much denser, and it is able to improve the viscosity as well as the setting time. It shows

that LbL coating is able to pack the halloysite on the fly ash surface, therefore delaying the setting time of the geopolymer cement. A similar study will be conducted at room temperature in the future.

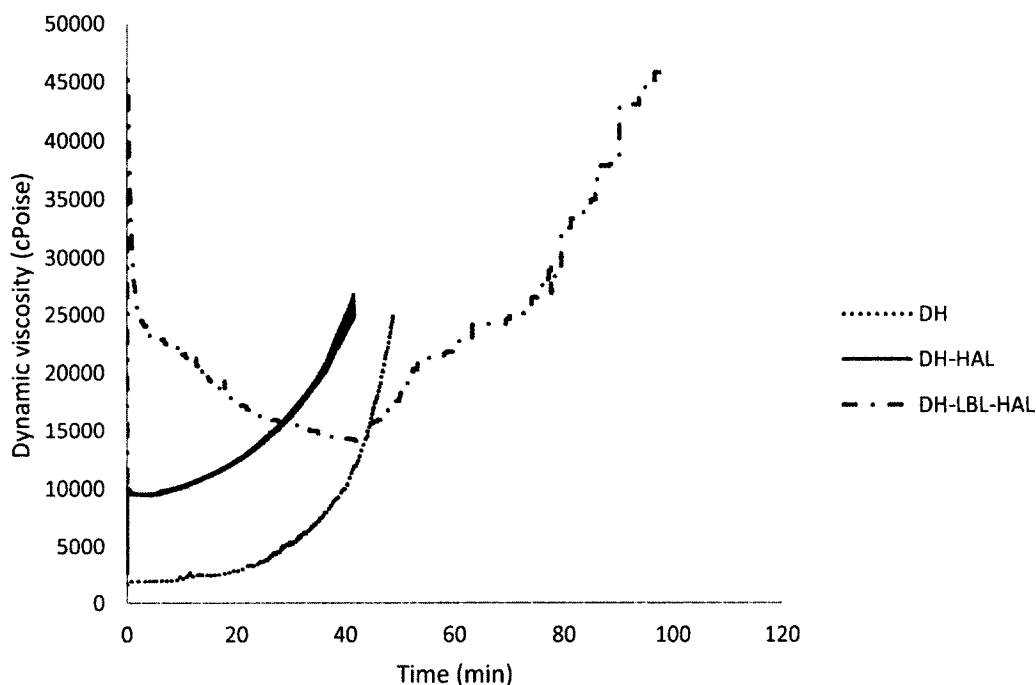


Figure 7-12: Viscosity at 50° C. for control DH fly ash, fly ash with control 6% halloysite, and fly ash with 6% treated halloysite.

7.4 Conclusion

Halloysite nanotubes are coated onto the fly ash microparticles in two different ways: adding halloysite into dry fly ash, and adding halloysite into the geopolymer paste. Geopolymerization is performed using 10 M and 12 M of NaOH solutions. In the case of positively charged fly ash, microparticles coated with negatively charged clay nanotube is performed directly in the one step procedure. However, for negatively charged fly-ash microparticle, it is necessary for the deposition of clay nanotubes in alternation with polycations optimizing with this positive/negative electrostatic interaction of the

components. The halloysite adding method have effect on the viscosity measurement, as the addition of halloysite into the dry fly ash have more setting time than the sample with halloysite added into the geopolymer paste. Halloysite nanotubes were successfully coated on to DH and MO fly ash surfaces by Layer-by-Layer (LbL) assembly. The surface of fly ashes was modified with polyelectrolytes: a polycation, PEI, and polyanion, PAA. Zeta potential analysis show that the fly ash surface was modified after deposition of each polyelectrolyte layer. For the MO fly ash, the setting time improve with the addition of 6% of the halloysite premixed with the fly ash. Viscosity measurement for MO at room temperature show that LbL coated MO fly ash with 6% halloysite had better setting time than the other two samples.

For the high calcium content DH fly ash at a higher temperature of 50° C, the LbL coated fly ash sample with 6% halloysite proves to have better functionality than the other two samples. The behaviour of LbL treated MO fly ashes with halloysite at high temperature, and LbL coated DH fly ash with halloysite at room temperature is still to be explored.

CHAPTER 8

CONCLUSION AND FUTURE WORK

8.1 Conclusion

Halloysite nanotubes applications for chemical agents encapsulation is developed for anticorrosive and flame retardant protective coatings. Being a naturally occurring clay mineral, halloysite is available in thousands of tons, is biocompatible, and allows for economical scale-up in an environmentally friendly manner.

Halloysite clay nanotubes have a loading efficiency of 10-12 wt%. The loading efficiency is improved by selective etching of the internal alumina layer using sulfuric acid. With increasing molarity of the sulfuric acid and the temperature, the etching rate increase, and the halloysite nanotubes become hollow silica nanotubes. 1 M sulfuric acid at 50° C for 24 hrs is considered optimum to achieve a 40-50% lumen enlargement. TEM analysis show that the internal diameter of the halloysite is increased, without affecting the outer diameter. Halloysite loading efficiency is improved by more than 2 times for benzotriazole.

Halloysite tubes are loaded with anticorrosive: benzotriazole, 2-mercaptobenzimidazole, 2-mercaptobenzothiazole and dodecylamine. These loaded halloysites are admixed with the paint at 5 wt%, and the coating corrosion-healing properties are analyzed. Anticorrosive agents release is controlled by the synthesis of

metal-organic end-tube complexation and polymeric stoppers. Cu-BTA complex stoppers have the best functionality for a controlled slow release. 2-mercaptobenzimidazole is found to be the most effective as an anticorrosive agent for ASTM A366 steel. However, halloysite loaded with 2-mercaptobenzimidazole and urea-formaldehyde stoppers have better adhesion properties. Metal-organic and polymeric stoppers are optimized on the halloysite loaded with standard anticorrosion agent dodecylamine. Dodecylamine release is analyzed in water and paint thinner, xylol. For metal-organic complexation, Fe(III) ions based stoppers are more effective. Sodium tripolyphosphate are effective as compared to Fe (II) and Cu (I)-BTA stoppers.

Extending our strategy of protective composites doped at 5-7 wt% with clay nanotubes, we develop flame-retardant coatings. Halloysite nanotubes are mixed with the latex paint, and applied on a wooden flake or metal boards. Upon exposure to the flame-torch, the paint sample with 5 wt% halloysite has better flame retardant properties than a commercial flame retardant. The analysis is based on ASTM E84 standard which includes analysis based on smoke development and flame spread show 2 times the slow burning of the coating as compared with an undoped paint layer. Second, a chemical agent triphenyl phosphate is loaded into the halloysite lumen with an efficiency of 6 wt%. Doping paint with such loaded halloysite allows for synergistic flame-retardant properties combining anti-burning properties clay nanotubes themselves and their lumen-loaded phosphate ester agents.

Halloysite nanotubes are coated onto fly ash microparticle surface using Layer-by-Layer (LbL) assembly with sequential polycations deposition (polyethylenimine – PEI

and polyacrylic acid - PAA). Zeta potential analysis shows regular alternation of the surface's electrical potential, confirming that fly ash is modified with the polyelectrolytes and nanoclay forming multilayer nanocoating. LbL modified fly ash had better halloysite coating than the controlled fly ash pre-mixed with halloysite. For nanoclay modified fly ash, solidification (curing) time is increased from ca. 18 minutes to 4 hrs, which is very important for applications of geopolymers (LaTech disclosure was filed and patent is in preparation). Rheological testing shows that viscosity of the sample improved for the LbL coated fly ash with a 6% halloysite addition.

8.2 Future Work

Halloysite nanotubes are successfully used as an encapsulating agent for anticorrosive agents. Results show that halloysite can be used as an alternative to other encapsulating agents for the purpose of self-healing, and flame retardant coatings.

For the anticorrosive coatings, future study will involve the analysis of the coatings based on ASTM D870 standard on the ferrous substrate coated with paint doped with halloysite samples preloaded with anticorrosive agents which will be exposed to a corrosive environment at a temperature slightly higher than room temperature for 30 days. Efficiency of the coating will be analysed based on the sample's appearance, self-healing effect, SVET analysis, and mechanical properties of the coating.

The effect of the base on the halloysite will also be analysed in future halloysite studies. Halloysite will be exposed to basic environment with different molarities and temperatures. The structure of halloysite will be analysed using SEM, TEM, and XRD. A

comparison study will be made based on the observation with the selective alumina etching of the halloysite using acid.

Halloysite application as a flame retardant will be extended with the loading of different types of flame retardants. The next phase of the study will involve the characterization by cone calorimetry to check the ignition time, mass loss, and the amount of heat released. The study will be made on both wooden flake and metal surfaces. Analysis will be made according to ASTM E84 standard, which involves analysis based on flame spread, and smoke developed.

Halloysite will also be used as an encapsulating agent for antioxidants. Antioxidant loaded halloysite nanotubes will be used as an additive into styrene-butadiene rubber (SBR) to improve aging of the rubber, and also mechanical properties. Halloysite are hydrophilic in nature. Therefore, efforts will also be made to hydrophobize the halloysite with silanating agents so that they can get easily dispersed in rubber.

In recent study fly ash-halloysite composite is made. Future study will be concentrated on loading halloysite with carboxymethyl cellulose (CMC) to prepare flexible geopolymers. Halloysite will be used as a nanocontainer for CMC, and controlled release of CMC will extend the flexibility of the geopolymer.

APPENDIX A

KINETICS OF SELECTIVE ALUMINA ETCHING AND CHARACTERIZATION OF DEALUMINATION

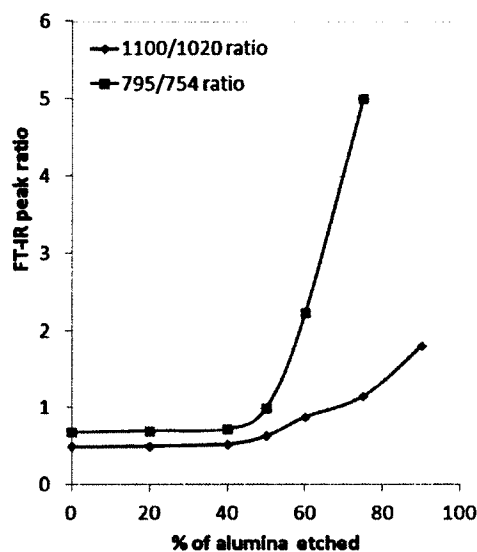


Figure A-1: FT-IR Peak ratios of halloysites at different levels of dealumination.

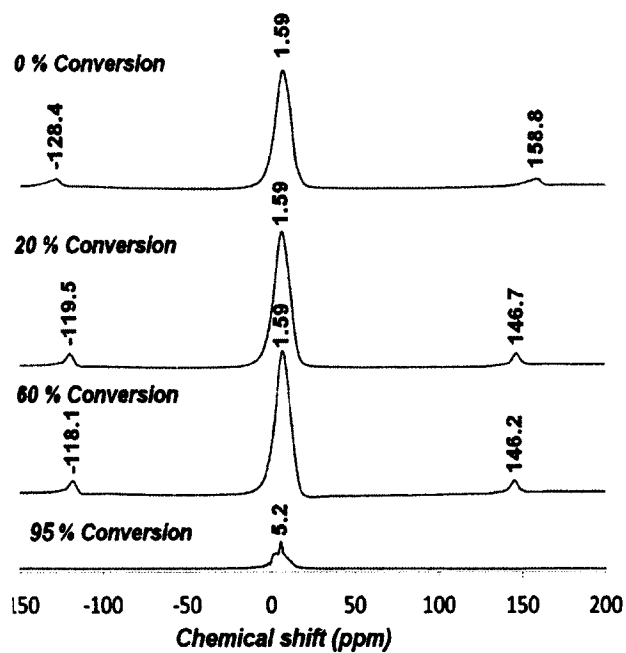


Figure A-2: Solid State ^{27}Al NMR Spectra of halloysite samples at various levels of dealumination by sulfuric acid.

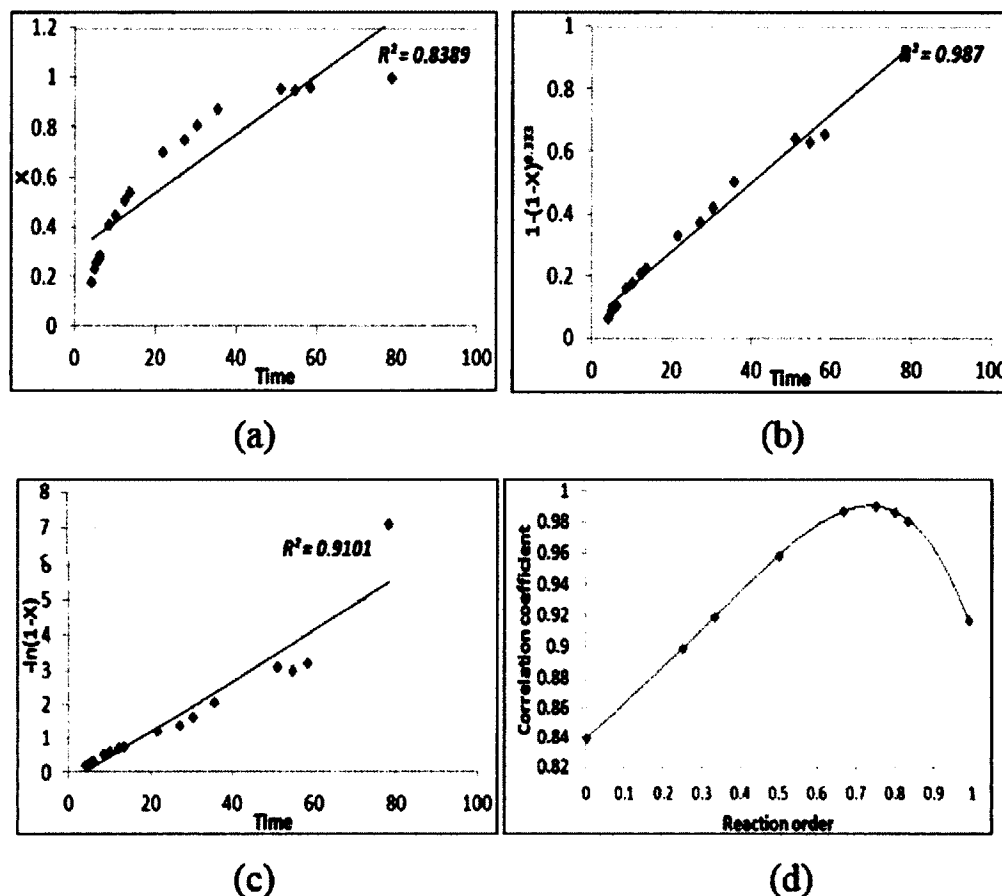


Figure A-3: Kinetic curves of the halloysite dealumination at 80° C fit to the kinetic models of zeroth (A), 2/3rd (B) and first (C) order reaction kinetics. Correlation coefficients of the halloysite dealumination curves at 80°C fit to the kinetic equations of various orders in aluminum (D). Kinetic profiles were fit to the equation $Kt = 1 - (1 - X)^{1-n}$, where K is the reaction rate constant, X is the halloysite dealumination level at time t and n is the reaction order in aluminum. Maximum correlation is observed at value of $n = 2/3$.

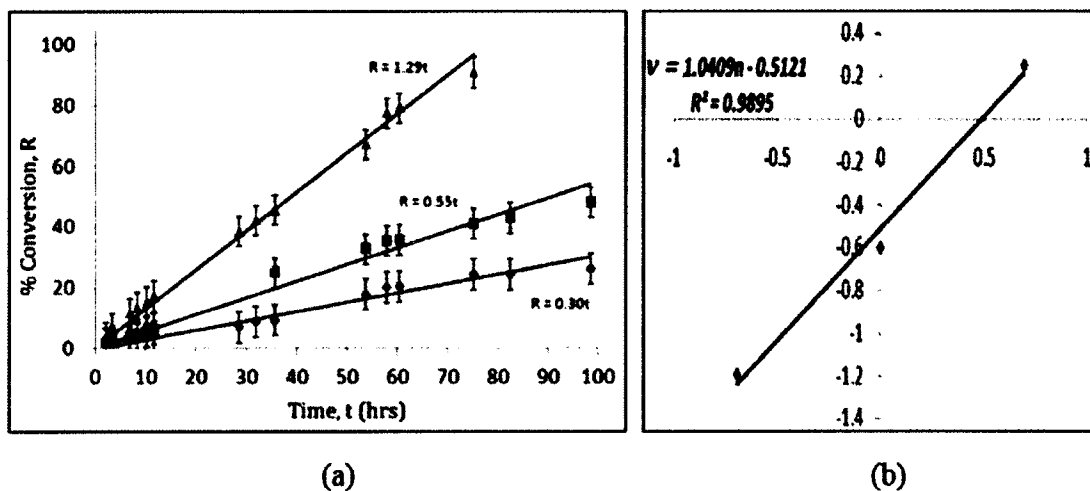


Figure A-4: (a) Alumina etching curves of halloysites at 50° C with sulfuric acid of three different concentrations 0.5 M (diamonds), 1.0 M (squares) and 2.0 M (triangles). (b) $\ln(v)$ vs $\ln(c)$ curves of the alumina etching profiles, v -reaction rate, c -sulfuric acid concentration. As one can see, $\ln(v) = \ln(c) + C$, i.e. $v = k \cdot c$.

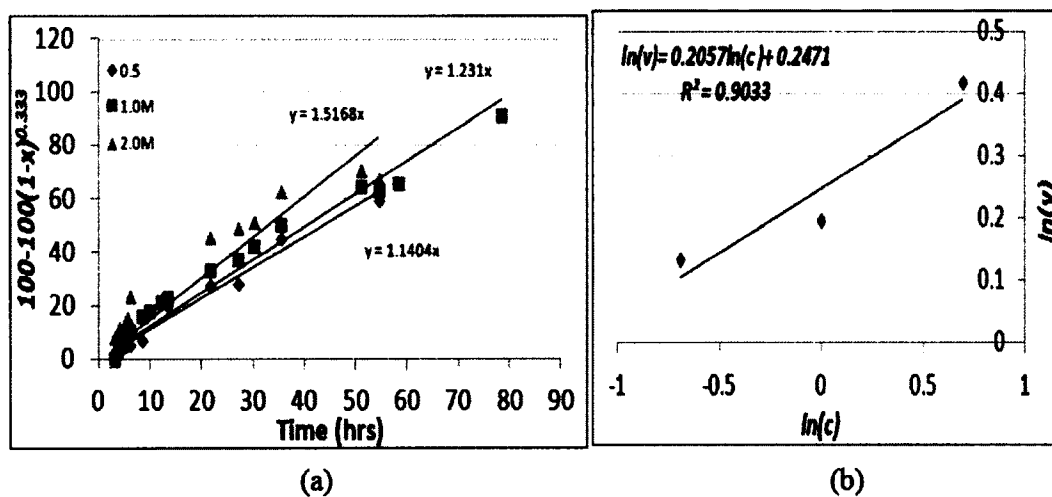


Figure A-5: (a) Alumina etching curves of halloysites at 80° C with sulfuric acid of three different concentrations 0.5 M (diamonds), 1.0 M (squares) and 2.0 M (triangles). (b) $\ln(v)$ vs $\ln(c)$ curves of the alumina etching profiles, v -reaction rate, c -sulfuric acid concentration. As one can see, $\ln(v) = 0.2\ln(c) + C$, i.e. $v = k \cdot c^0$.

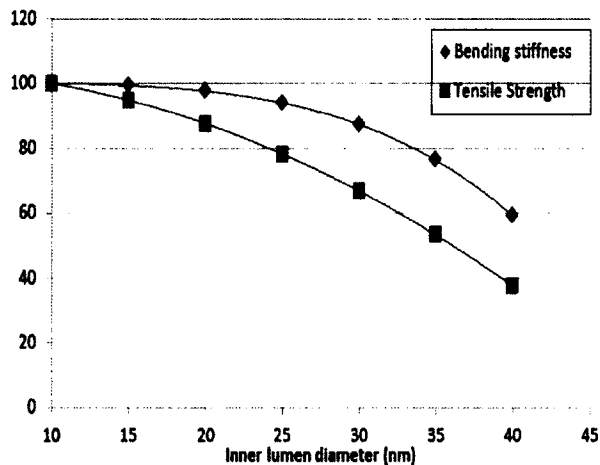


Figure A-6: Relative values of halloysite bending stiffness and tensile strength (normalized to 100) at various lumen diameters.

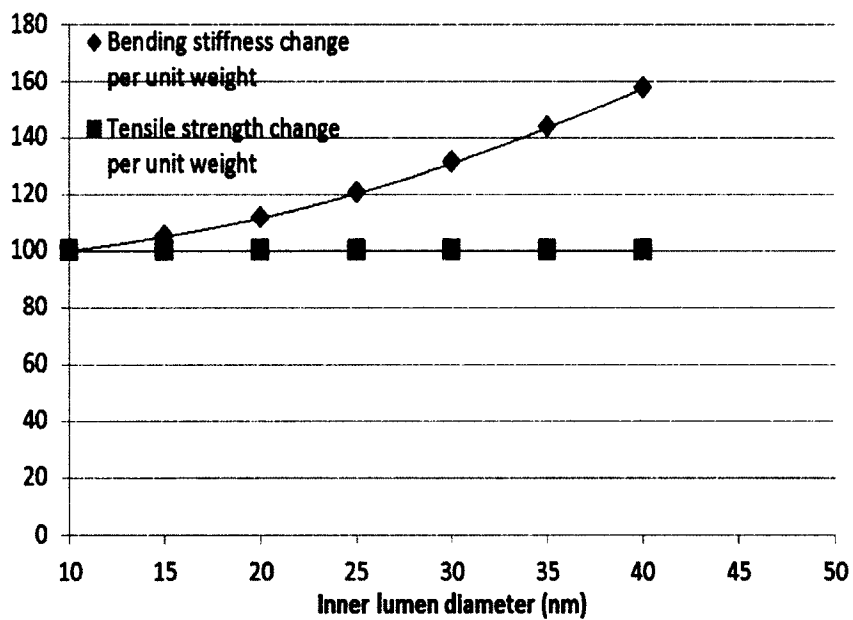


Figure A-7: Relative values of halloysite bending stiffness and tensile strength per unit weight (normalized to 100) at various lumen diameters.

APPENDIX B

ANALYSIS OF ANTICORROSIVE AGENTS LOADING BASED ON THERMOGRAVIMETRIC ANALYSIS

Halloysite loading efficiency for anticorrosive agents is alternately analyzed using thermogravimetric analysis (TGA). Anticorrosive agents, BTA, 2-MBI and 2-MBT, are loaded into the halloysite using a vacuum. Acetone is used as a solvent for the loading. Loading is performed with 3 vacuum cycles for efficient loading. For the last vacuum cycle, the sample is left in the vacuum chamber overnight. The next day, the samples are washed with acetone 2 times to remove excess anticorrosive agents from the surface. Samples are dried in a vacuum chamber. The sample pan is loaded into the TGA, and the weight is set to zero before loading the sample. After zeroing the sample pan about 10 mg of the sample is placed into the sample pan, and the TGA heating mode is set to the heat ramp where the temperature increases steadily at the mentioned value. For the above mentioned samples, the temperature set is 10° C/min as the template and loaded material do not have close melting points.

In the case of pure BTA, the melting point is 94° C. When loaded into the halloysite, the melting point is extended to 204° C. (Figure B-8) shows that BTA is loaded into the halloysite lumen, and after reaching the 200+ temperature, it boil out of the halloysite. BTA has a boiling point of 204° C.

In the case of 2-MBT (Figure B-9), it has a melting point of 172-182° C in its pure form. When loaded into the halloysite, the melting point extend to 213° C, which is again an indication of loading inside the lumen.

Figure B-10 is of the TGA curve for the 2-MBI loaded into the halloysite. Pure 2-MBI has a melting point of 300° C. For halloysite loaded 2-MBI, the melting point observed is 294° C, which is where the point of mass loss starts, and extend up to 325° C.

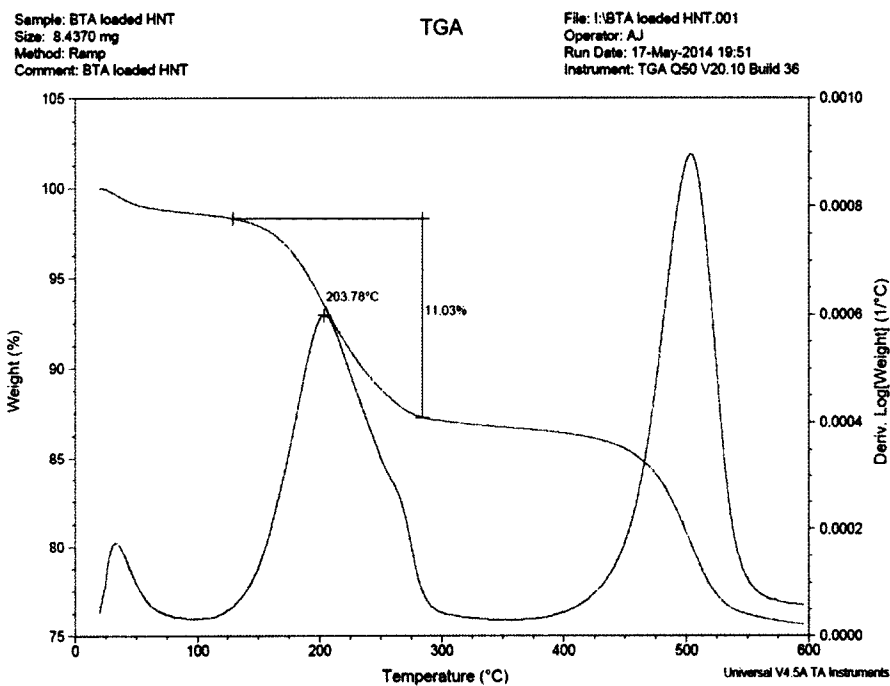


Figure B-8: TGA curve for BTA loaded halloysite nanotubes.

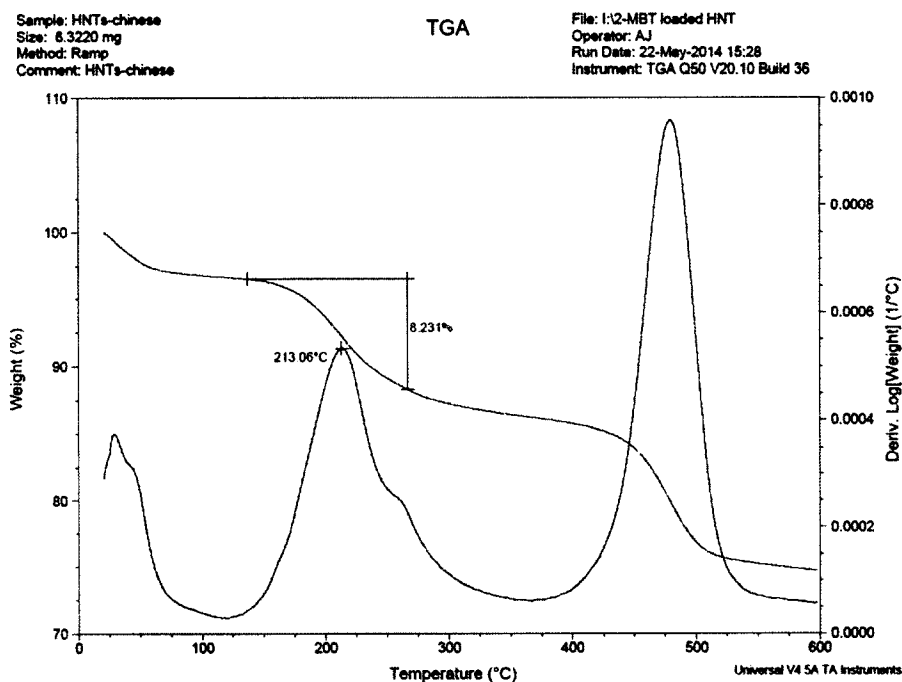


Figure B-9: TGA curve for 2-MBT loaded halloysite nanotubes.

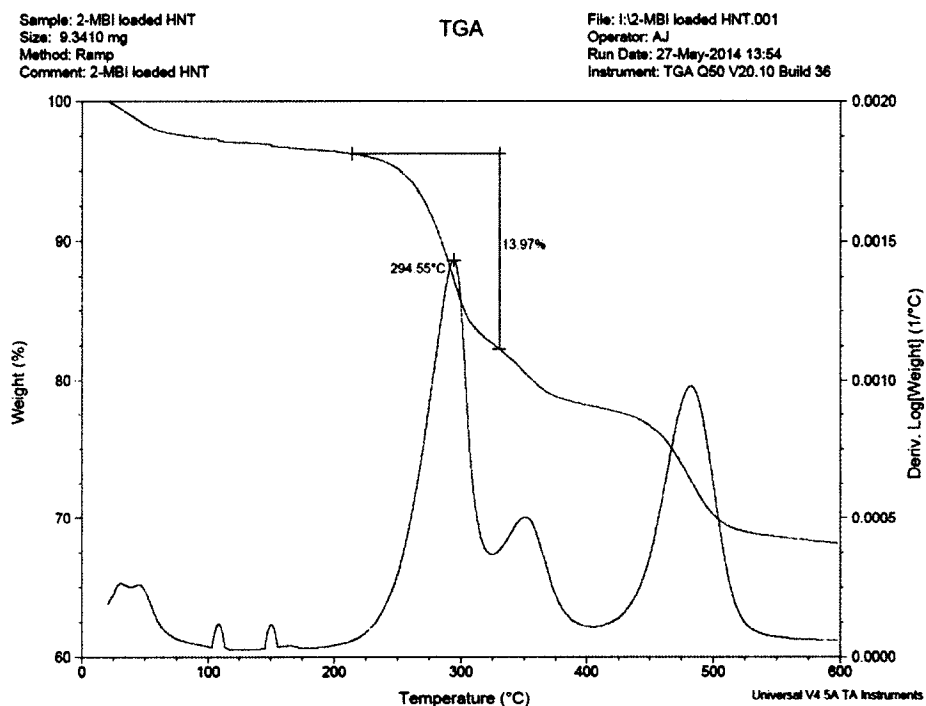


Figure B-10: TGA curve for 2-MBI loaded halloysite nanotubes.

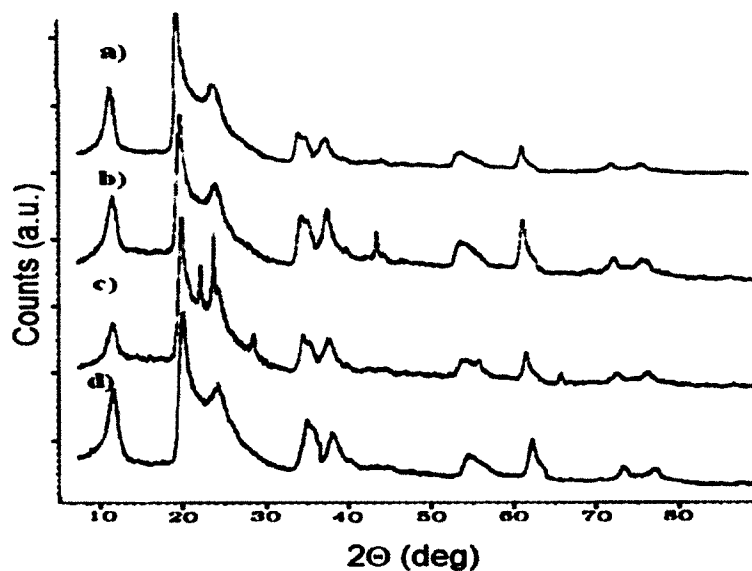


Figure B-11: X-ray powder diffraction patterns (Cu-K α) of the halloysite loaded with BTA (a), MBT (b), and MBI (c) and empty pristine halloysite (d).

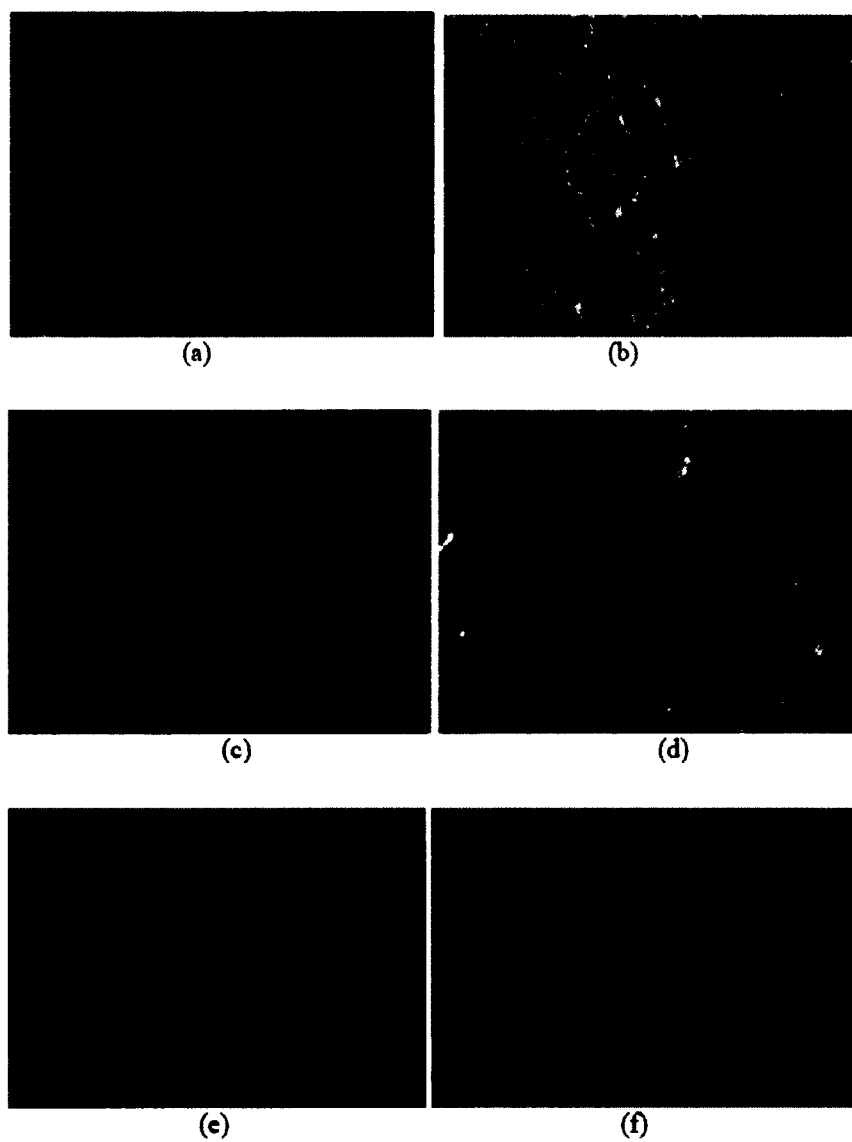


Figure B-12: Optical microscope images from the back sides of the coatings removed from corroded steel strips, (a)-original paint and paint admixed with (b)-BTA, (c)-MBT, (d)-MBI, (e) BTA loaded halloysite with Cu-stoppers, and (f) BTA loaded halloysite with UF-stoppers.

REFERENCES

- [1] A. S. T. Bates, F. Hildebrand, "Morphology and structure of endellite and halloysite," *American Mineralogist*, vol. 35, no. 7-8, pp. 463-483, 1950.
- [2] G. Churchman, L. Albridge, and R. Carr, "The relationship between the hydrated and dehydrated state of a halloysite," *Clays and Clay Minerals*, vol. 20, no. 1948, pp. 241-246, 1972.
- [3] E. Joussein, S. Petit, J. Churchman, B. Theng, D. Righi, and B. Delvaux, "Halloysite clay minerals – a review," *Clays and Clay Minerals*, vol. 40, no. 4, pp. 383-426, December, 2005.
- [4] M. F. L. De Volder, S. H. Tawfick, R. H. Baughman, and a J. Hart, "Carbon nanotubes: present and future commercial applications.," *Science*, vol. 339, no. 6119, pp. 535-539, February, 2013.
- [5] S.-H. Zhang, Z.-X. Xie, Z.-Y. Jiang, X. Xu, J. Xiang, R.-B. Huang, and L.-S. Zheng, "Synthesis of silver nanotubes by electroless deposition in porous anodic aluminium oxide templates.," *Chem. Commun. (Camb)*, no. 9, pp. 1106-7, May 2004.
- [6] S. Baral, S. Brandow, and B. Gaber, "Electroless metalization of halloysite, a hollow cylindrical 1: 1 aluminosilicate of submicron diameter," *Chem. Mater.*, vol. 5, no. c, pp. 1227-1232, 1993.
- [7] D. G. Shchukin, G. B. Sukhorukov, R. R. Price, and Y. M. Lvov, "Halloysite nanotubes as biomimetic nanoreactors.," *Small*, vol. 1, no. 5, pp. 510-3, May 2005.
- [8] I. Wilson, "Kaolin and halloysite deposits of China," *Clays and Clay Minerals*, vol. 39, pp. 1-15, January, 2004.
- [9] D. Marney, L. Russell, and D. Wu, "The suitability of halloysite nanotubes as a fire retardant for nylon 6," *Polym. Degrad. Stab.*, vol. 93, pp. 1971-1978, July, 2008.
- [10] B. Lecouvet, J. G. Gutierrez, M. Sclavons, and C. Bailly, "Structure–property relationships in polyamide 12/halloysite nanotube nanocomposites," *Polym. Degrad. Stab.*, vol. 96, no. 2, pp. 226-235, February, 2011.

- [11] J. Premkumar, O. Lev, R. Rosen, and S. Belkin, "Encapsulation of luminous recombinant *E. coli* in sol-gel silicate films," *Adv. Mater.*, vol. 13, no. 23, pp. 1773-1775, 2001.
- [12] D. G. Shchukin, S. V. Lamaka, K. A. Yasakau, M. L. Zheludkevich, M. G. S. Ferreira, and H. Mohwald, "Active Anticorrosion Coatings with Halloysite Nanocontainers," *J. Phys. Chem. C*, vol. 112, no. 4, pp. 958-964, January, 2008.
- [13] E. Koh, S. Lee, J. Shin, and Y.-W. Kim, "Renewable Polyurethane Microcapsules with Isosorbide Derivatives for Self-Healing Anticorrosion Coatings," *Ind. Eng. Chem. Res.*, vol. 52, no. 44, pp. 15541-15548, November, 2013.
- [14] L. J. De Cock, S. De Koker, B. G. De Geest, J. Grooten, C. Vervaet, J. P. Remon, G. B. Sukhorukov, and M. N. Antipina, "Polymeric multilayer capsules in drug delivery," *Angew. Chem. Int. Ed. Engl.*, vol. 49, no. 39, pp. 6954-73, September, 2010.
- [15] D. G. Shchukin and H. Möhwald, "Self-repairing coatings containing active nanoreservoirs," *Small*, vol. 3, no. 6, pp. 926-43, June, 2007.
- [16] M. T. Cook, G. Tzortzis, D. Charalampopoulos, and V. V. Khutoryanskiy, "Production and evaluation of dry alginate-chitosan microcapsules as an enteric delivery vehicle for probiotic bacteria," *Biomacromolecules*, vol. 12, no. 7, pp. 2834-40, July, 2011.
- [17] T. Kaiden, E. Yuba, A. Harada, Y. Sakanishi, and K. Kono, "Dual signal-responsive liposomes for temperature-controlled cytoplasmic delivery," *Bioconjug. Chem.*, vol. 22, no. 10, pp. 1909-15, October, 2011.
- [18] C. Daraio, V. F. Nesterenko, J. F. Aubuchon, and S. Jin, "Dynamic Nanofragmentation of Carbon Nanotubes," *Nano Lett.*, vol. 4, no. 10, pp. 1915-1918, October, 2004.
- [19] C. Tang, Y. Bando, D. Golberg, X. Ding, and S. Qi, "Boron Nitride Nanotubes Filled with Ni and NiSi₂ Nanowires in Situ," *J. Phys. Chem. B*, vol. 107, pp. 6539-6543, April, 2003.
- [20] N. G. Veerabadran, D. Mongayt, V. Torchilin, R. R. Price, and Y. M. Lvov, "Organized shells on clay nanotubes for controlled release of macromolecules," *Macromol. Rapid Commun.*, vol. 30, no. 2, pp. 99-103, January, 2009.
- [21] E. Abdullayev, R. Price, D. Shchukin, and Y. Lvov, "Halloysite tubes as nanocontainers for anticorrosion coating with benzotriazole," *ACS Appl. Mater. Interfaces*, vol. 1, no. 7, pp. 1437-43, July, 2009.

- [22] E. Abdullayev and Y. Lvov, "Clay nanotubes for corrosion inhibitor encapsulation: release control with end stoppers," *J. Mater. Chem.*, vol. 20, no. 32, pp. 6681-6687, May, 2010.
- [23] V. Vergaro, E. Abdullayev, Y. M. Lvov, A. Zeitoun, R. Cingolani, R. Rinaldi, and S. Leporatti, "Cytocompatibility and uptake of halloysite clay nanotubes," *Biomacromolecules*, vol. 11, no. 3, pp. 820-6, March, 2010.
- [24] J. Forsgren and E. Jämstorp, "A ceramic drug delivery vehicle for oral administration of highly potent opioids," *J. Pharma. Sci.*, vol. 99, no. 1, pp. 219-226, 2010.
- [25] L. Alexander, G. Faust, and S. Hendricks, "Relationship of the clay minerals halloysite and endellite," *American Mineralogist.*, vol. 28, no. 1826, pp. 1-18, 1943.
- [26] D. MacEwan, "The nomenclature of the halloysite minerals," *Minerologist Magazine*, no. 5, pp. 36-44, 1947.
- [27] G. Churchman and R. Carr, "The definition and nomenclature of halloysites," *Clays and Clay Minerals*, vol. 23, no. 1950, pp. 382-388, 1975.
- [28] I. Bobos, J. Duplay, J. Rocha, and C. Gomes, "Kaolinite to halloysite-7 Å transformation in the kaolin deposit of São Vicente de Pereira, Portugal," *Clays Clay Miner.*, vol. 49, no. 6, pp. 596-607, 2001.
- [29] M. H. H. Richard H. Bennett, William R. Bryant, *Microstructure of Fine-Grained Sediments: From Mud to Shale*. Springer, pp. 582, 1991.
- [30] B. Singh, "Why Does Halloysite Roll?--A New Model," *Clays and Clay Minerals*, vol. 44, no. 2, pp. 191-196, 1996.
- [31] S. LEE and S. KIM, "Adsorption of naphthalene by HDTMA modified kaolinite and halloysite," *Appl. Clay Sci.*, vol. 22, no. 1-2, pp. 55-63, November, 2002.
- [32] M. Jackson and F. Abdel-Kader, "Kaolinite intercalation procedure for all sizes and types with X-ray diffraction spacing distinctive from other phyllosilicates," *Clays and Clay Minerals*, vol. 26, no. 2, pp. 81-87, 1978.
- [33] K. Tazaki, "Microbial formation of a halloysite-like mineral," *Clays and Clay Minerals*, vol. 53, no. 3, pp. 224-233, 2005.
- [34] N. G. Veerabadran, R. R. Price, and Y. M. Lvov, "Clay nanotubes for encapsulation and sustained release of drugs," *ACS Nano*, vol. 02, no. 02, pp. 115-120, April, 2007.

- [35] M. T. Viseras, C. Aguzzi, P. Cerezo, C. Viseras, and C. Valenzuela, "Equilibrium and kinetics of 5-aminosalicylic acid adsorption by halloysite," *Microporous Mesoporous Mater*, vol. 108, no. 1-3, pp. 112-116, February, 2008.
- [36] M. Zhao and P. Liu, "Adsorption behavior of methylene blue on halloysite nanotubes," *Microporous Mesoporous Mater*, vol. 112, no. 1-3, pp. 419-424, July, 2008.
- [37] R. Frost and J. Kristof, "Intercalation of halloysite: a Raman spectroscopic study," *Clays and Clay Minerals*, vol. 45, no. 4, pp. 551-563, 1997.
- [38] G.J.Churchman, J.S. Whitton, G.G.C. Claridge, B.K.G.Theng., "Intercalation method using formamide for differentiating halloysite from kaolinite," *Clays and Clay Minerals*, vol. 32, no. 4, pp. 241-248, 1984.
- [39] E. Joussein, S. Petit, and B. Delvaux, "Behavior of halloysite clay under formamide treatment," *Appl. Clay Sci.*, vol. 35, no. 1-2, pp. 17-24, January, 2007.
- [40] S. J. Antill, "Halloysite: A Low-Cost Alternative," *Aust. J. Chem.*, vol. 56, no. 7, p. 723, July, 2003.
- [41] H. M. Kelly, P. B. Deasy, E. Ziaka, and N. Claffey, "Formulation and preliminary in vivo dog studies of a novel drug delivery system for the treatment of periodontitis.," *Int. J. Pharm.*, vol. 274, no. 1-2, pp. 167-83, May, 2004.
- [42] S. R. Levis and P. B. Deasy, "Characterisation of halloysite for use as a microtubular drug delivery system.," *Int. J. Pharm.*, vol. 243, no. 1-2, pp. 125-34, August, 2002.
- [43] R. M. Carr, "Intercalation of Salts in Halloysite," *Clays and Clay Minerals*, vol. 26, no. 2, pp. 144-152, 1978.
- [44] S. Hillier and P. C. Ryan, "Identification of halloysite (7 Å) by ethylene glycol solvation: the 'MacEwan effect,'" *Clay Minerals*, vol. 37, no. 3, pp. 487-496, September, 2002.
- [45] E. Abdullayev, A. Joshi, W. Wei, Y. Zhao, and Y. Lvov, "Enlargement of halloysite clay nanotube lumen by selective etching of aluminum oxide," *ACS Nano*, vol. 6, no. 8, pp. 7216-26, August, 2012.
- [46] A. Joshi, E. Abdullayev, A. Vasiliev, O. Volkova, and Y. Lvov, "Interfacial Modification of Clay Nanotubes for the Sustained Release of Corrosion Inhibitors," *Langmuir*, vol. 29, pp. 7439-7448, 2012.

- [47] E. Abdullayev and Y. Lvov, "Halloysite clay nanotubes for controlled release of protective agents," *J. Nanosci. Nanotechnol.*, vol. 11, no. 11, pp. 10007-26, November, 2011.
- [48] R. R. Price, B. P. Gaber, and Y. Lvov, "In-vitro release characteristics of tetracycline HCl, khellin and nicotinamide adenine dinucleotide from halloysite; a cylindrical mineral," *J. Microencapsul.*, vol. 18, no. 6, pp. 713-22, 2007.
- [49] V. Vergaro, Y. M. Lvov, and S. Leporatti, "Halloysite clay nanotubes for resveratrol delivery to cancer cells," *Macromol. Biosci.*, vol. 12, no. 9, pp. 1265-71, October, 2012.
- [50] A. D. Hughes and M. R. King, "Use of naturally occurring halloysite nanotubes for enhanced capture of flowing cells," *Langmuir*, vol. 26, no. 14, pp. 12155-64, July, 2010.
- [51] R. Qi, R. Guo, M. Shen, X. Cao, L. Zhang, J. Xu, J. Yu, and X. Shi, "Electrospun poly(lactic-co-glycolic acid)/halloysite nanotube composite nanofibers for drug encapsulation and sustained release," *J. Mater. Chem.*, vol. 20, no. 47, pp. 10622, November, 2010.
- [52] Y.-F. Shi, Z. Tian, Y. Zhang, H.-B. Shen, and N.-Q. Jia, "Functionalized halloysite nanotube-based carrier for intracellular delivery of antisense oligonucleotides," *Nanoscale Res. Lett.*, vol. 6, no. 1, pp. 608, January, 2011.
- [53] W. Wei, E. Abdullayev, A. Hollister, D. Mills, and Y. M. Lvov, "Clay nanotube/poly(methyl methacrylate) bone cement composites with sustained antibiotic release," *Macromol. Mater. Eng.*, vol. 297, no. 7, pp. 645-653, July, 2012.
- [54] E. Abdullayev and Y. Lvov, "Halloysite Clay Nanotubes for Controlled Release of Protective Agents," *J. Nanosci. Nanotechnol.*, vol. 11, no. 11, pp. 10007-10026, November, 2011.
- [55] Y. M. Lvov, D. G. Shchukin, H. Möhwald, and R. R. Price, "Halloysite clay nanotubes for controlled release of protective agents," *ACS Nano*, vol. 2, no. 5, pp. 814-20, May, 2008.
- [56] M. Du, B. Guo, and D. Jia, "Thermal stability and flame retardant effects of halloysite nanotubes on poly(propylene)," *Eur. Polym. J.*, vol. 42, no. 6, pp. 1362-1369, June, 2006.
- [57] M. Du, B. Guo, and D. Jia, "Newly emerging applications of halloysite nanotubes: a review," *Polym. Int.*, vol. 59, pp. 574-582, 2010.

- [58] H. Jing, Y. Higaki, W. Ma, H. Wu, W. O. Yah, H. Otsuka, Y. M. Lvov, and A. Takahara, "Internally Modified Halloysite Nanotubes as Inorganic Nanocontainers for a Flame Retardant," *Chem. Lett.*, vol. 42, no. 2, pp. 121-123, 2013.
- [59] K. Geckeler and M. Shamsi, "Gold nanoparticle-halloysite nanotube and method of forming the same," *US Pat. App. 12/244,762*, vol. 1, no. 19, pp. 1-12, 2008.
- [60] E. Abdullayev, K. Sakakibara, K. Okamoto, W. Wei, K. Ariga, and Y. Lvov, "Natural tubule clay template synthesis of silver nanorods for antibacterial composite coating," *ACS Appl. Mater. Interfaces*, vol. 3, no. 10, pp. 40406, October, 2011.
- [61] A. Rapsomanikis and D. Papoulis, "Halloysite clay mineral composite films prepared by sol-gel method: synergistic effect and the case of silver modification," *Glob. NEST J.*, vol. 16, no. 3, pp. 485-498, 2014.
- [62] K. Prashantha, "Processing and characterization of halloysite nanotubes filled polypropylene nanocomposites based on a masterbatch route: effect of halloysites treatment on structural and mechanical properties," *Express Polym. Lett.*, vol. 5, no. 4, pp. 295-307, February, 2011.
- [63] D. R. Paul and L. M. Robeson, "Polymer nanotechnology: Nanocomposites," *Polymer*, vol. 49, no. 15, pp. 3187-3204, July, 2008.
- [64] B. Guo, F. Chen, Y. Lei, and D. Jia, "Tubular Clay Composites with High Strength and Transparency," *J. Macromol. Sci. Part B*, vol. 49, no. 1, pp. 111-121, January, 2010.
- [65] A. A. Azeez, K. Y. Rhee, S. J. Park, and D. Hui, "Epoxy clay nanocomposites – processing, properties and applications: A review," *Compos. Part B Eng.*, vol. 45, no. 1, pp. 308-320, February, 2013.
- [66] S. Pande, S. H. M. D. Bedre, R. Bhat, R. Deshpande, and a. Venkataraman, "Synthesis, Characterization and Studies of PANI-MMT Nanocomposites," *Journal of Nanoscience and Nanotechnology*, vol. 2, no. 4, pp. 90-98, August, 2012.
- [67] Q. H. Zeng, A. B. Yu, G. Q. Lu, and D. R. Paul, "Clay-based polymer nanocomposites: research and commercial development," *J. Nanosci. Nanotechnol.*, vol. 5, no. 10, pp. 1574-92, October, 2005.
- [68] A. L. Wagner, S. Cooper, and M. Riedlinger, "Natural nanotubes enhance biodegradable and biocompatible nanocomposites," *Ind. Biotechnol.*, vol. 1, no. 3, pp. 190-193, September, 2005.

- [69] M. Du, B. Guo, M. Liu, and D. Jia, "Preparation and Characterization of Polypropylene Grafted Halloysite and Their Compatibility Effect to Polypropylene/Halloysite Composite," *Polym. J.*, vol. 38, no. 11, pp. 1198-1204, September, 2006.
- [70] W. C. Oifutt and A. C. Whitaker, "Catalytic conversion process employing as catalyst, a halloysite clay activated with magnesium oxide," *US 2744056 A*, pp. 2-4, 1956.
- [71] E. Emam, "Clays as Catalysts in Petroleum Refining Industry," *ARPJ. Sci. Technol.*, vol. 3, no. 4, pp. 356-375, 2011.
- [72] T. Milliken, "Use of clays as petroleum cracking catalysts," *Clays and Clay Minerals*, pp. 314-326, 1952.
- [73] D. Santilli, "Residual oil processing catalysts," *US Pat. 4,358,400*, pp. 2-5, 1982.
- [74] H. Robson, "Synthetic halloysites as hydrocarbon conversion catalysts," *US Pat. 4,098,676*, pp. 2-6, 1978.
- [75] Y. Lvov, R. Price, B. Gaber, and I. Ichinose, "Thin film nanofabrication via layer-by-layer adsorption of tubule halloysite, spherical silica, proteins and polycations," *Colloids Surfaces A Physicochem. Eng. Asp.*, vol. 198-200, pp. 375-382, February, 2002.
- [76] G. Cavallaro, D. I. Donato, G. Lazzara, and S. Milioto, "Films of Halloysite Nanotubes Sandwiched between Two Layers of Biopolymer: From the Morphology to the Dielectric, Thermal, Transparency, and Wettability Properties," *J. Phys. Chem. C*, vol. 115, no. 42, pp. 20491-20498, October, 2011.
- [77] Y. Lvov and E. Abdullayev, "Functional polymer-clay nanotube composites with sustained release of chemical agents," *Prog. Polym. Sci.*, vol. 38, no. 10-11, pp. 1690-1719, October, 2013.
- [78] B. Guo, Y. Lei, F. Chen, X. Liu, M. Du, and D. Jia, "Styrene-butadiene rubber/halloysite nanotubes nanocomposites modified by methacrylic acid," *Appl. Surf. Sci.*, vol. 255, no. 5, pp. 2715-2722, December, 2008.
- [79] Y. Ye, H. Chen, J. Wu, and L. Ye, "High impact strength epoxy nanocomposites with natural nanotubes," *Polymer*, vol. 48, no. 21, pp. 6426-6433, October, 2007.
- [80] M. Du, B. Guo, M. Liu, and D. Jia, "Thermal decomposition and oxidation ageing behaviour of polypropylene/halloysite nanotube nanocomposites," *Polym. Polym. Compos.*, vol. 15, no. 4, pp. 321-328, 2007.

- [81] R. D. White, D. V Bavykin, and F. C. Walsh, "The stability of halloysite nanotubes in acidic and alkaline aqueous suspensions," *Nanotechnology*, vol. 23, no. 6, pp. 065705-065715, February, 2012.
- [82] A.-B. Zhang, L. Pan, H.-Y. Zhang, S.-T. Liu, Y. Ye, M.-S. Xia, and X.-G. Chen, "Effects of acid treatment on the physico-chemical and pore characteristics of halloysite," *Colloids Surfaces A Physicochem. Eng. Asp.*, vol. 396, pp. 182-188, February, 2012.
- [83] M. Bhanot and B. . Jennings, "Transient light scattering from halloysite suspensions," *J. Colloid Interface Sci.*, vol. 56, no. 1, pp. 92-99, July, 1976.
- [84] E. Abdullayev, D. Shchukin, and Y. Lvov, "Halloysite Clay Nanotubes as a Reservoir for Corrosion Inhibitors and Template for Layer-by-Layer Encapsulation," *Polym. Mater. Sci. Eng.*, vol. 99, pp. 331-332, 2008.
- [85] P. Yuan, P. D. Southon, Z. Liu, M. E. R. Green, J. M. Hook, S. J. Antill, and C. J. Kepert, "Functionalization of Halloysite Clay Nanotubes by Grafting with γ - Aminopropyltriethoxysilane," *J. Phys. Chem. C*, vol. 112, pp. 15742-15751, 2008.
- [86] U. Vijayalakshmi, "Synthesis and characterization of porous silica gels for biomedical applications," *Trends Biomater Artif. Organs*, vol. 18, pp. 101-105, January, 2005.
- [87] J. Fitzgerald, A. Hamza, C. E. Bronnimann and S. Dec, "Studies of the Solid/Solution 'Interfacial' Dealumination of Kaolinite in HCl (aq) Using Solid-State 1H CRAMPS and SP/MAS 29Si NMR Spectroscopy," *J. Am. Chem. Soc.*, vol. 119, no. 26, pp. 7105-7113, 1997.
- [88] D. R. Vollet, J. D. Macedo, and Y. P. Mascarenhas, "Pore structure characterization of kaolin, metakaolin, and their acid-treated products using small-angle X-ray scattering," *Appl. Clay Sci.*, vol. 8, no. 6, pp. 397-404, February, 1994.
- [89] M. Rıza Altıokka, H. Akalın, N. Melek, and S. Akyalcı, "Investigation of the Dissolution Kinetics of Meta-Kaolin in H₂SO₄ Solution," *Ind. Eng. Chem. Res.*, vol. 49, no. 24, pp. 12379-12382, December, 2010.
- [90] E. Aglietti, J. Porto Lopez, and E. Pereira, "Structural alterations in kaolinite by acid treatment," *Appl. Clay Sci.*, vol. 3, no. 2, pp. 155-163, May 1988.
- [91] F. Habashi, *Principles of Extractive Metallurgy, Volume 1*. CRC Press, pp. 153-163, 1969.
- [92] K. Smith and R. Kirkpatrick, "High-resolution silicon-29 nuclear magnetic resonance spectroscopic study of rock-forming silicates," *American Mineralogist*, vol. 68, pp. 1206-1215, 1983.

- [93] D. G. Shchukin, M. Zheludkevich, K. Yasakau, S. Lamaka, M. G. S. Ferreira, and H. Möhwald, "Layer-by-Layer Assembled Nanocontainers for Self-Healing Corrosion Protection," *Adv. Mater.*, vol. 18, no. 13, pp. 1672-1678, July, 2006.
- [94] J.-M. Yeh, S.-J. Liou, C.-Y. Lin, C.-Y. Cheng, Y.-W. Chang, and K.-R. Lee, "Anticorrosively Enhanced PMMA-Clay Nanocomposite Materials with Quaternary Alkylphosphonium Salt as an Intercalating Agent," *Chem. Mater.*, vol. 14, no. 1, pp. 154-161, January, 2002.
- [95] G. S. Frankel, "Pitting Corrosion of Metals," *J. Electrochem. Soc.*, vol. 145, no. 6, p. 2186, 1998.
- [96] K. D. Demadis, C. Mantzaridis, and P. Lykoudis, "Effects of Structural Differences on Metallic Corrosion Inhibition by Metal-Polyphosphonate Thin Films," *Ind. Eng. Chem. Res.*, vol. 45, no. 23, pp. 7795-7800, November, 2006.
- [97] M. L. Zheludkevich, D. G. Shchukin, K. A. Yasakau, H. Möhwald, and M. G. S. Ferreira, "Anticorrosion Coatings with Self-Healing Effect Based on Nanocontainers Impregnated with Corrosion Inhibitor," *Chem. Mater.*, vol. 19, no. 3, pp. 402-411, February, 2007.
- [98] K. Ariga, A. Vinu, and Y. Yamauchi, "Nanoarchitectonics for mesoporous materials," *Bull. Chem. Soc. Jpn.*, vol. 85, no. 1, pp. 1-32, 2012.
- [99] Z. Li, J. C. Barnes, A. Bosoy, J. F. Stoddart, and J. I. Zink, "Mesoporous silica nanoparticles in biomedical applications," *Chem. Soc. Rev.*, vol. 41, no. 7, pp. 2590-605, April, 2012.
- [100] X. He, Y. Zhao, D. He, K. Wang, F. Xu, and J. Tang, "ATP-responsive controlled release system using aptamer-functionalized mesoporous silica nanoparticles," *Langmuir*, vol. 28, no. 35, pp. 12909-15, September, 2012.
- [101] A. P. Esser-Kahn, S. A. Odom, N. R. Sottos, S. R. White, and J. S. Moore, "Triggered Release from Polymer Capsules," *Macromolecules*, vol. 44, no. 14, pp. 5539-5553, July, 2011.
- [102] K. Ariga, Q. Ji, J. P. Hill, Y. Bando, and M. Aono, "Forming nanomaterials as layered functional structures toward materials nanoarchitectonics," *NPG Asia Mater.*, vol. 4, no. 5, p. e17, May, 2012.
- [103] J. Barthes, D. Mertz, C. Bach, M.-H. Metz-Boutigue, B. Senger, J.-C. Voegel, P. Schaaf, and P. Lavalle, "Stretch-induced biodegradation of polyelectrolyte multilayer films for drug release," *Langmuir*, vol. 28, no. 38, pp. 13550-4, September, 2012.

- [104] S. De Koker, R. Hoogenboom, and B. G. De Geest, "Polymeric multilayer capsules for drug delivery," *Chem. Soc. Rev.*, vol. 41, no. 7, pp. 2867-84, April, 2012.
- [105] X. Luo, C. Matranga, S. Tan, N. Alba, and X. T. Cui, "Carbon nanotube nanoreservoir for controlled release of anti-inflammatory dexamethasone," *Biomaterials*, vol. 32, no. 26, pp. 6316-23, September, 2011.
- [106] Y. J. Suh, D. S. Kil, K. S. Chung, E. Abdullayev, Y. M. Lvov, and D. Mongayt, "Natural nanocontainer for the controlled delivery of glycerol as a moisturizing agent," *J. Nanosci. Nanotechnol.*, vol. 11, no. 1, pp. 661-5, January, 2011.
- [107] C. J. Ward, S. Song, and E. W. Davis, "Controlled Release of Tetracycline-HCl from Halloysite-Polymer Composite Films," *J. Nanosci. Nanotechnol.*, vol. 10, no. 10, pp. 6641-6649, October, 2010.
- [108] D. N. P. Murthy, M. Xie, and R. Jiang, *Weibull Models*. John Wiley & Sons, 2004, pp. 408.
- [109] R. A. and P. M. R. Oltra, V. Maurice, *Local Probe Techniques for Corrosion Research*. Cambridge, UK: Woodhead Publishing; 1st edition, 2007, pp. 12-180.
- [110] E. Hodnett and W. Willie, "Schiff bases of salicylaldehyde and their cobalt (II) derivatives as antitumor agents," *Proc. Okla. Acad. Sci.*, no. 11, pp. 107-111, 1966.
- [111] L. S. Birnbaum and D. F. Staskal, "Brominated Flame Retardants: Cause for Concern?," *Environ. Health Perspect.*, vol. 112, no. 1, pp. 9-17, October, 2003.
- [112] W. de Vos and M. Kesner, "Teaching about Flame Retardants. A Joint Israeli-Dutch Project," *J. Chem. Educ.*, vol. 78, no. 1, p. 41, January, 2001.
- [113] B. ScharTEL, "Phosphorus-based Flame Retardancy Mechanisms—Old Hat or a Starting Point for Future Development?," *Materials (Basel)*, vol. 3, no. 10, pp. 4710-4745, September, 2010.
- [114] S. Johnson, S. Guggenheim, and A. Van Groos, "Thermal stability of halloysite by high-pressure differential thermal analysis," *Clays and Clay Minerals*, vol. 38, no. 5, pp. 477-484, 1990.
- [115] M. Al Bakri, H. Mohammed, H. Kamarudin, I. Niza and Y. Zarina "Review on fly ash-based geopolymer concrete without Portland Cement," *J. Engi. Tech. Res.*, vol. 3, pp. 1-4, January, 2011.
- [116] D. P. Bentz and C. F. Ferraris, "Rheology and setting of high volume fly ash mixtures," *Cem. Concr. Compos.*, vol. 32, no. 4, pp. 265-270, April, 2010.

- [117] P. Duxson, a. Fernández-Jiménez, J. L. Provis, G. C. Lukey, a. Palomo, and J. S. J. Deventer, "Geopolymer technology: the current state of the art," *J. Mater. Sci.*, vol. 42, no. 9, pp. 2917-2933, December, 2006.
- [118] Y. Lvov, K. Ariga, M. Onda, I. Ichinose, and T. Kunitake, "Alternate assembly of ordered multilayers of SiO₂ and other nanoparticles and polyions," *Langmuir*, vol. 7463, no. 14, pp. 6195-6203, 1997.
- [119] E. I. Diaz-Loya, E. Allouche, S. Eklund, A. Joshi and K. Kupwade-Patil, "Toxicity mitigation and solidification of municipal solid waste incinerator fly ash using alkaline activated coal ash," *Waste Manag.*, vol. 32, pp. 1521-1527, 2012.